FIBRE OPTIC DISTRIBUTED CORROSION SENSOR

A thesis submitted for the degree of Doctor of Philosophy

by

Elena Sinchenko

Centre for Atom Optics and Ultrafast Spectroscopy

Faculty of Engineering and Industrial science

Swinburne University of Technology

Melbourne, Australia

2013

Abstract

Corrosion monitoring is an important aspect of increasing the safety and reliability of large structures such as aircraft, ships, submarines and bridges. In general, current non-destructive corrosion detection techniques are only able to detect local changes after significant damage has occurred. Moreover, corrosion often localises in areas that are inaccessible for inspection, especially in large structures. This implies a need for sensitive detection systems with multiple sensors in order to monitor the initial stages of corrosion over large areas.

Thus, the development of a wide-area detection system for continuously monitoring structural changes, together with a capability for non-destructive evaluation and early warning, is an important task. The aim of the present research is to evaluate the feasibility of a distributed optical fibre sensor for detecting corrosion at arbitrary points of interest in a large structure.

A detection method based on the estimation of water ingress into conventional optical fibre during the corrosion process was tested. This method was based on changes in the water peak absorption in a sensor made from conventional optical fibre. This did not give conclusive results. This method may be attractive for sensor designs based on hygroscopic glasses or fibres with small cladding thickness.

In the method chosen for further development, the fluorescence from the complex Tris-(8-hydroxyquinoline)aluminum (Alq_3) produced by the reaction of Al^{3+} ions with the indicator 8-HQ was detected. A theoretical model was developed to evaluate the evanescent field interaction mechanism and critical parameters of the detection system. This suggested that fluorescent emissions generated by the evanescent field and coupled back into guided modes could be detected by means of photon counting technology. Moreover, the location of the fluorescence could be resolved by measuring the time-of-flight of the fluorescent emission returned from a short excitation pulse.

Two constructions of the optical fibre sensor, based on etched D-shaped fibre and declad plastic-clad fibre, were examined as sensing elements for distributed measurements. Evaluation of the results in terms of practical considerations such as

cost, additional development requirements and the risks to achieving the required results, led to the choice of a plastic clad fibre that could be easily declad as a sensing element for the detection system.

A system based on pulsed excitation and time-gated photon counting was used to detect a localized source of fluorescence at an arbitrary position along the fibre length. Environments examined were the complex Alq_3 excited at 405 nm and the infrared dye IR-125, excited at 780 nm. A model to characterize the response of the sensor to a Gaussian input pulse was developed and tested. Analysis of the Alq_3 fluorescence response confirmed the validity of the model and enabled the fluorescence lifetime to be determined. The decay rate was found to be proportional to concentration, which is indicative of collisional deactivation. The intrinsic lifetime obtained (18.2±0.9 ns) is in good agreement with published data. The minimum Alq_3 concentration that could be detected is 5×10^{-5} M (~20 ppm) over an exposed length of 0.2 m, whereas the detection limit for IR-125 is 2×10^{-6} M (~1.2 ppm). The model allows the spatial resolution of the distributed sensing system to be improved in those cases where the fluorophore lifetime is longer than the resolution of the sensing system.

The absorbance and fluorescence response of the multimode optical fibre evanescent wave sensor was analysed to investigate the influence of different conditions, such as environmental refractive index, excitation wavelength, and launching conditions. Theoretical models were developed to investigate and improve the efficiency of the optical fibre detection system. The potential for using the developed detection system in practical sensing applications was successfully demonstrated in a stimulated corrosion test.

Acknowledgement

This thesis would never have been possible without the great help of many people I had the pleasure to work with for the long five years. As they say, “It Takes a Village to Raise a Child…”

Firstly, I would like to thank my supervisors A/Prof. Alex Mazzolini and Dr Paul Stoddart for giving me the great opportunity to work in the exciting research field of optical fibre sensing; even if my knowledge about optical fibre technology at that time was limited by an article from Wikipedia.

I am deeply thankful to Paul for his timely and practical support and great encouragement through all the ‘ups’ and ‘downs’ of my research journey. I am also very thankful for spending many hours discussing, reading, and improving the materials for this thesis.

I am giving special thanks to Keith Gibbs for introducing me to the world of Modelling and Statistics. With Keith’s help my humble experimental results became meaningful and truly scientific. Calling myself Keith’s colleague always was a big honour for me.

I would like to acknowledge the opportunity to be involved in a big industrial project and the financial support from the DSTO. Big thanks to Claire Davies and all other members of the team working on the Fibre Optic Corrosion Sensing Project. Special thanks to Grant McAdam and Silvia Tejedor for organizing and participating in the practical application testing.

I appreciate help from Prof. Peter Cadusch with the mathematical intricacies.

Thanks to Sheila and Andrea, it was pleasure to work in the neat and organized labs.

Thanks to Mark Kivinen for making all the working mechanical things despite the fact that the given drawings were not so clear.

Many thanks to our administrator Tatiana Tchernova for making all paperwork (it is larger than a thesis altogether) an easy task.

And big special thanks to my wonderful husband and my both most loved sons. Yes, we are there … yet!

Declaration

I, Elena Sinchenko, declare that this thesis entitled:

"Fibre optic distributed corrosion sensor"

is my own work and has not been submitted previously, in whole or in the part, in respect of any other academic award.

Elena Sinchenko

Centre for Atom Optics and Ultrafast Spectroscopy
Faculty of Engineering and Industrial science
Swinburne University of Technology
Melbourne, Australia

Dated this day, 29th July, 2013

Publications

Effect of Cladding Refractive Index on an Optical Fiber Evanescent-Wave Sensor
Elena Sinchenko, W.E. Keith Gibbs, Alexander P. Mazzolini, Paul R. Stoddart
Journal of Lightwave Technology, 2013 (in press)

Influence of cladding refractive index on a ditributed optical fibre chemical sensor
Paul Stoddart, Alex P. Mazzolini, Elena Sinchenko, W. E. Keith Gibbs
Proceedings of the 19th Australian Institute of Physics Congress (2010)

Characterization of time-resolved fluorescence response measurements for distributed optical-fiber sensing
E. Sinchenko, W.E.K. Gibbs, C.E. Davis and P.R. Stoddart
Applied Optics 49 6385-6390 (2010)

Distributed fluorescence sensing using exposed-core microstructured optical fiber
S.C. Warren-Smith, E. Sinchenko, P.R. Stoddart and T.M. Monro
IEEE Photonics Technology Letters 22 1385-1387 (2010)

Fluorescence lifetime effects in distributed optical fiber chemical sensing
W. E. K. Gibbs, E. Sinchenko, Paul Stoddart
Technical Digest of IMCS-13, 13th International Meeting on Chemical Sensors, Perth, July 2010

Fluorescence-based distributed chemical sensing for structural health monitoring
Elena I. Sinchenko; W. E. Keith Gibbs; Paul R. Stoddart
Smart Structures, Devices, and Systems IV, edited by Said Fares Al-Sarawi, Vijay K. Varadan, Neil Weste, Kourosh Kalantar-Zadeh, Proc. of SPIE Vol. 7268, 72681K (2008)

Optical fibre techniques for distributed corrosion sensing
E. Sinchenko, G. McAdam, C. Davis, S. McDonald, I. McKenzie, P.J. Newman and P.R. Stoddart
ACOFT/AOS Conference 2006 - 10-13 July 2006.
RMIT University, Melbourne, Australia

Table of contents

List of illustrations and tables

Figures

Tables

Chapter 1

Project motivation

Corrosion has been found to be one of the major damage mechanisms affecting engineering structures, including constructions such as bridges and pipelines, as well as mobile transport structures such as marine ships or aircraft which normally operate in a highly corrosive environment. The probability of corrosion damage increases with the age of the structure, particularly when the original design lifetime is exceeded. Therefore, detection of corrosion at the early stages is very important to reduce the costs of maintenance and to ensure safety.

A major concern which increases the risk of damage and repair costs is corrosion in hidden or inaccessible areas. Generally, by the time that corrosion detection is possible without disassembly, the damage is so extensive that massive repairs and even replacement of entire parts are required.

Thus, the development of a detection system for continuously monitoring large-scale structural changes, together with the ability for non-destructive evaluation, remains an important task.

1.1 Corrosion basics and sensing mechanisms for corrosion

Corrosion can be defined as the destructive attack of a metal by chemical or electrochemical reaction with the environment that causes metals to be transformed into their salts and oxides. Modern corrosion science is based on the electrochemical theory of corrosion. The electrochemical theory presents corrosion processes as a combination of anodic oxidation such as metal dissolution with metal ion production and a cathodic reduction such as oxygen ionisation or production of hydrogen ions. The electrochemical theory of corrosion applies to any type of metal; in this chapter we will

discuss the fundamental reactions during corrosion mostly for aluminium as the metal most relevant to the project.

Aluminium has a highly negative standard electrode potential of -1660 mV (Vargel 2004), so it is expected to be very unstable in the presence of moisture. However, experience shows that this is not the case, and aluminium shows a resistance to corrosion in most environments, despite the thermodynamic prediction. This stability is associated with the presence of a continuous oxide film on the surface. At room temperature in air, a protective film is formed on the surface of aluminium in such small time as 10^{-4} seconds, which prevents further deterioration of the metal (Totten and MacKenzie 2003). So aluminium is a passive metal. But like all passive metals, aluminium is prone to localised corrosion caused by a local rupture of the passive film. Under certain conditions, such as a presence of active anions, variation of pH value and so on, localised corrosion will develop and propagate.

In order to understand corrosion mechanisms, it is necessary to consider some basic facts of electrochemistry. As a simple example shown in Figure 1.1, we consider the corrosion process in the 2024 aluminium alloy from which most aircraft structures are made. Aluminium alloy 2024 is an aluminium alloy, with copper and magnesium as the alloying elements (copper is the chief alloying agent). It is used in applications requiring high strength to weight ratio, as well as good fatigue resistance.

The microscopic grains of aluminium and copper materials in the 2024 aluminium alloy together with an electrolyte serve as a classical electrochemical cell. Sources of the electrolyte can be atmospheric moisture containing dissolved sea salt or dissolved acids, salts or alkalis from industrially contaminated air. In the example, a diluted hydrochloric acid is considered as the electrolyte. The electrode potential difference at the place of aluminium-copper contact causes production of positive ions within the aluminium (anodic oxidation):

$$Al \rightarrow Al^{3+} + 3e^{-} \qquad (3.1)$$

Because aluminium is more electronegative than copper it will form the anode of the galvanic action, whereas copper acts as a cathode. The presence of the electrolyte allows a complete circuit to be formed. The aluminium ions attract chlorine ions from the electrolyte and form aluminium chloride:

$$Al^{3+}+3Cl^{-}\rightarrow AlCl_3 \quad (3.2)$$

Aluminium chloride is a salt of corrosion which is deposited at the surface of the aluminium. Hydrogen ions are attracted to the copper by the remaining electrons from the aluminium and are neutralised with production of H_2 molecules, which release as a free gas (cathodic reduction).

$$2H^{+}+2e^{-}\rightarrow H_2 \quad (3.3)$$

Corrosion is formed on the aluminium where the corrosion salt replaces the metal and causes severe changes in the properties of the material.

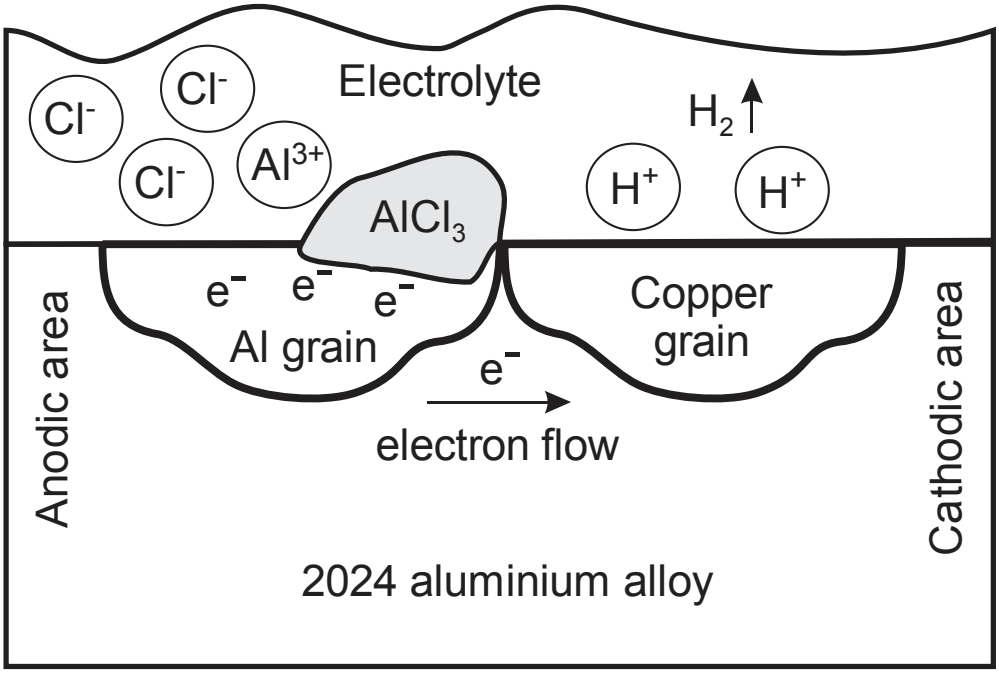

Figure 1.1. Electro-chemical cell in galvanic corrosion process. Adapted from (Jeppesen and Sanderson 1985).

Different types of corrosion can occur on aluminium (Jeppesen and Sanderson 1985), such as uniform (generalised) corrosion, pitting corrosion, transgranular and intergranular (intercrystalline) corrosion, exfoliation corrosion, stress corrosion, etc.

Factors causing corrosion include the presence of acids and alkalis in the working environment, as well as salts, some contaminating metals such as mercury, simple water and air which serve as media for the electrochemical reactions. A relatively new problem is corrosion caused by organic growth in the fuel tanks. The predominant type

of corrosion will depend on a certain number of factors that are intrinsic to the metal, the medium and the conditions of use. There is no form of corrosion that is specific to aluminium and its alloys (Vargel 2004).

Corrosion is most dangerous when it develops in inaccessible areas. In the internal micro structure of aluminium alloys, areas of dissimilar metals provide efficient cathodes and anodes for corrosion formation. This type of corrosion is called intergranular corrosion. If corrosive action reaches the boundary between the grains through an interrupted protective oxide film, the corrosion can continue within the metal. Intergranular corrosion is difficult to detect directly because it happens within the metal itself, rather than on the surface. The only practical and certain fix for this type of corrosion is replacement of the part (Jeppesen and Sanderson 1985).

Another type of corrosion develops in the situation when water enriched with dissolved oxygen from the air covers the surface of a metal such as aluminium airplane skins and seeps into the cracks between the lap joints of the sheets. Water and oxygen attract electrons from the metal to form negative hydroxide ions. The oxygen concentration is higher in water on the open area than in the cracks. This results in a difference in potential between the area of high oxygen concentration and that of low oxygen concentration, and provides electron flow between hidden and open areas. Electrons flow to the open area which becomes a cathode. The area between the skins, having lost electrons, now has positive aluminium ions and becomes the anode. Positive aluminium ions attract the negative hydroxide ions from the water and form a common corrosion product – aluminium hydroxide. This type of corrosion is called oxygen concentration cell corrosion. Oxygen cell corrosion forms under the marking tape of ferrules on aluminium tubing, beneath sealer that has loosened, or under bolt or screw heads.

There are various techniques for monitoring corrosion in metal structures and they can be divided into two basic categories. There are those that provide a direct measure of corrosion (e.g. weight loss measurements), and indirect techniques that utilize a related parameter to provide an indirect indication of the presence and degree of corrosion. Depending on the particular corrosive environment that is anticipated, and the confidence of the relationship between a specific environmental parameter and the degree of corrosion of a certain material, monitoring of an indirect parameter to

establish the corrosion condition can be quite reliable. Common indirect measurements of corrosion include parameters such as electrochemical potential, pH, temperature, oxygen presence, moisture content (especially condensed water), specific ions that have been identified as aggressive (e.g. chlorides) and the products of corrosion (usually metal ions). Detection of hydrogen diffusion through equipment walls has also been utilized to indirectly monitor corrosion reactions in specific structures (Roberge 2007).

1.1.1 Non-optical methods

There are a number of monitoring techniques that provide a direct measure of corrosion rates. They include techniques that can be used for continuous monitoring and those that are suitable for periodic assessment of the corrosion condition. The most commonly used method of corrosion monitoring is the evaluation of weight change of a "tell-tale" coupon over some exposure period. The time of exposure of the coupon is determined by the surface area of the coupon, type of metal, anticipated corrosion rate, and the sensitivity of the balance used for weighing the coupon. Obviously, weight loss measurements of coupons are designed to provide periodic assessment of corrosion and require disassembly of the inspected part.

Other appropriate non-optical techniques include electrical resistance and various electrochemical methods: linear polarization resistance, electrochemical impedance spectroscopy, electrochemical noise, harmonic impedance spectroscopy and galvanic current (Koch and Thompson 1994). In addition, more complex non-optical methods based on neutron radiography (Bossi et al. 1995) include atmospheric neutron radiography and fast neutron activation analysis.

1.1.2 Optical methods

Optical methods are some of the oldest and best-established techniques for sensing chemical analytes and have formed the basis of many chemical sensors. A corrosion process usually includes chemical or electrochemical transformations that can be detected by optical sensors. The development of inexpensive, high quality optical fibres for the communications industry has provided an essential component for implementation of optical sensors. There has been considerable research effort expended in developing sensors based on optical fibres for both physical and chemical analytes, with many interesting schemes proposed (Norris 2000).

Optical fibre chemical sensing involves the probing of matter by photons. Various parameters are associated with a photon flux and a change in any one of these may give analytical information about the materials being probed. There are several measurement techniques that are commonly used to monitor these parameters.

- Absorption and reflectance spectroscopy detects changes in intensity of the optical signal.
- Luminescence spectroscopy, Raman spectroscopy, Brillouin scattering spectroscopy and reflectance spectroscopy detect changes in wavelength.
- Luminescence lifetime techniques detect time characteristics of the optical signal, e.g. decay.
- Polarized absorbance, circular dichroism and interferometric techniques are used to measure changes in phase or polarization.

An essential component of any form of analysis using optical fibres is the optical fibre itself. This is usually made from a silica-based glass and less frequently from an organic polymer (e.g. polymethylmethacrylate). The development of fibres made from heavy metal halides or chalcogenides is extending the wavelength range at which optical fibre sensors can operate. Several potential advantages arise from using an optical fibre as the basis of a chemical (corrosion) analysis technique:

- **Suitability for remote in-situ measurements**. The small size, often less than 1 mm in diameter, flexibility, chemical stability and high transmission efficiency of optical fibres enables remote in-situ chemical analyses to be undertaken using fibre optic sensors.
- **Electrical isolation and freedom from electromagnetic interference**. As optical fibres are made from insulating materials, optical fibre sensors are, by their nature, electrically isolated from the interrogating electronics. This is especially important for in-vivo medical sensors and application areas where flammable or explosive reagents are present. The associated immunity to electromagnetic interference (EMI) makes them suitable for use in electrically noisy environments.
- **Potential for distributed sensing**. In principle, optical fibre chemical sensors can be made where the whole length of the fibre is sensitised to a particular analyte. The presence of the analyte at any point along the fibre can modify its optical properties, enabling a large area to be monitored simultaneously. Alternatively, the sensitized fibre can be interrogated by an optical equivalent of radar (optical time domain reflectometry,

OTDR) to give a measure of the analyte concentration as a function of position over the extended area. Very few such devices have been developed (Norris 2000).

1.2 Optical fibre sensors

This section presents a review of the field of corrosion detection using optical methods, especially those methods based on optical fibre measurements where there is potential for distributed sensing. A special effort has been made to discuss recent achievements in the design of corrosion sensors and new directions in developing detection systems as well.

1.2.1 Bragg-grating and long period grating sensors

The application of strain, temperature or pressure to a fibre grating causes a shift in the peak wavelength owing to a change in the refractive index and length of the host fibre. Fibre gratings can therefore be used as sensing elements for measuring strain, temperature or pressure, and offer stability, compactness, linearity of response, low insertion loss and are potentially inexpensive.

Unlike long-period grating sensors (LPGs), short period gratings do not easily lend themselves to monitoring changes in the index of refraction of the cladding. However, the short-period gratings may still be used to monitor corrosion using a technique that has been successfully demonstrated using metal-coated, prestrained optical fibre strain gauges. In the proposed technique, the Bragg grating is prestrained and coated with a layer of metal, which "freezes" the sensor in the prestrained state. As the corrosion process occurs and metal is removed from the sensor, the residual strain of the sensor element decreases and can be used to indirectly monitor the corrosion level. A number of sensors based on this principle have been designed and tested (Trego et al. 1998), (Greene et al. 1996).

Lo and Xiao (Lo and Xiao 1998) present a method to measure metal corrosion using a single-pitch Bragg grating sensor. A prestrained Bragg grating which is only partially coated with a metal can be designed as a corrosion transducer, and the section without a metal coating can be used as a temperature sensor. After releasing the preloading, the two Bragg wavelengths reflected from the Bragg grating are sufficiently separated that there is no cross-talk between the corrosion and temperature signals.

Since the temperature variation is obtained from the free section, any thermal drift in the Bragg grating corrosion sensor can be measured and compensated.

In addition, sensors for the detection of corrosion precursors and by-products (moisture, Cu^{2+}metal ions) were developed by Luna Innovation, Inc. (Cooper et al. 2001). The moisture sensor was fabricated by coating a LPG sensor element with poly(ethylene oxide) PEO, formed from the polymerization of ethylene oxide monomers. In the presence of water, the PEO hydrogel coating absorbs water and swells, leading to a decrease in the refractive index at the surface of the fibre and a resulting shift in the out-coupled LPG wavelength. For the metal-ion sensor, a chelating polymer coating with an affinity for 2+ metal-ions is attached to the surface of the LPG sensing element. When metal ions are present they form inter-chain and intra-chain cross-links with the carboxyl groups in the chelating polymer, significantly reducing the phase volume of the polymer chains. This cross-linking increases the density of the polymer coating and results in an increase in refractive index at the surface of the fibre, again causing a shift in the wavelength out-coupled by the LPG.

For the purposes of distributed sensing, fibre Bragg gratings can be deployed in a quasi-distributed arrangement along an optical fibre back-bone. The different sensing positions are essentially wavelength encoded, which implies a need for relatively expensive and bulky spectral interrogation systems and broadband light sources. A recent review states that “although grating sensors have been intensively developed for more than 10 years there are countless trials and there are a few commercial successes. The highest profile of these is in monitoring the strain excursion history in carbon fibre composite yacht masts for the luxury and racing market” (Culshaw 2004). Thus their application to distributed corrosion sensing is probably limited.

1.2.2 Optical fibre sensing using indicator dyes

Indicators are synthetic dyes that undergo a colour change on interaction with a chemical species. The purpose of using so-called indicator chemistry (i.e. a dye in or on a polymeric support) in optical sensing is to convert the concentration of a chemical analyte into a measurable optical signal. In other words, the indicator acts as a transducer for the chemical species that frequently cannot be determined directly by optical means.

On interaction with the target analyte, chromophore indicators change the absorption spectrum with one band appearing as others disappear. Fluorescent indicators, in contrast, are frequently of the yes/no type in that only one of the species (i.e. the complexed or uncomplexed form) is fluorescent. Quenchable fluorophores undergo a change in intensity of a single band (usually decreasing with a specific decay constant). There are also fluorophores that undergo a shift in their spectral maximum due to the changing environment. This is called the solvatochromic effect (Wolfbeis 1997).

The chemistry of indicators is fairly well established and there are many examples of using indicator dyes without optical fibre to detect the species of interest, including the determination of metal ions (including aluminium) for corrosion detection (Johnson and Agarwala 1994, Johnson et al. 1997), chloride ions (Badr et al. 2000) and changes in pH level (Misra et al. 2002).

1.2.2.1 Fluorescence-based sensors

Presence or absence of fluorescent signal

An optical sensor for Al^{3+} based on the use of purpurin immobilised on XAD 4 (styrene-divinylbenzene cross-linked copolymer) (Ahmad and Narayanaswamy 2002) was used to measure fluorescence from a solid surface by mean of an optical fibre attachment to a spectro-fluorometer. A plot of log[Al^{3+} concentration] against the sensor response was linear for Al^{3+} concentrations in the range from 5.0×10^{-5} to 3.2×10^{-3} M, with a limit of detection of 3.0×10^{-5} M. A fluoride solution was shown not to quench the complex during measurements and was used as a regenerating agent to refresh the probe. Good repeatability (1%) and reproducibility (4%) of measurement were obtained with this probe.

The localized corrosion behaviour of a galvanic aluminium-copper couple was investigated by in situ fluorescence imaging with a fibre-optic imaging sensor (Szunerits and Walt 2002). Three different, but complementary, methods were used for visualizing remote corrosion sites, mapping the topography of the metal surface and measuring local chemical concentrations of H^+, OH^-, and Al^{3+}. The first method is based on a pH-sensitive imaging fibre, where the fluorescent dye SNAFL (seminaphthofluorescein) was covalently attached to the fibre's distal end. Fluorescence

images were acquired as a function of time at different areas of the galvanic couple. In a second method, the fluorescent dye morin was immobilized on the fibre-optic imaging sensor, which allowed the in situ localization of corrosion processes on pure aluminium to be visualized over time by monitoring the release of Al^{3+}. The development of fluorescence on the aluminium surface defined the areas associated with the anodic dissolution of aluminium. It was also shown that cerium chloride and 8-hydroxyquinoline effectively inhibit corrosion of pure aluminium by decreasing the current, reducing the number of active sites on the aluminium surface and passivating the surface faster. From the number and extent of corrosion sites and the release of aluminium ions monitored with the fibre, it was shown that 8-hydroxyquinoline is a more effective inhibitor than cerium chloride.

Fuhr with co-authors (Fuhr et al. 1998) investigated two fluorescent Cl^- ion indicators: MEQ (6-methoxy-N-ethylquinolinium iodide) and ABQ (6-methoxy-N-(n-aminoalkyl)quinolinium bromide hydrochloride (AAQ) with alkyl chain length of 4). Both are quinoline derivatives that have been exploited in the past as intracellular chloride indicators based on collisional quenching of their fluorescence by halide ions. The investigation demonstrated the potential for eventual implementation in an optical sensor, but immobilization into a sol-gel matrix was not successful.

Time-resolved spectroscopy (by quenching of fluorescence)

A novel laser-based corrosion sensor has been developed (Chin et al. 1996) using embedded optical fibre, near-infrared (NIR) dyes and phase-resolved fluorescence spectroscopy to detect corrosion by-products (aluminium and iron) at the incipient stage. During the initial research effort, the practicality of using phase-resolved fluorescence spectroscopy and the NIR dye fluorescence lifetime for characterization of metal ions was demonstrated.

Improvement of an optical fibre oxygen sensor based on fluorescence quenching by oxygen gas was reported (Morisawa et al. 1996). Using the newly synthesized poly-l-menthylmethacrylate (PMtMA) and its blend of poly(4-methyl-1-pentene) (PMP) as the cladding layer in which a sensing dye was doped, a plastic optical fibre (POF) oxygen sensor with high sensitivity (with the quenching rate of 5.85×10^3 $s^{-1}\%^{-1}$) and a fast response time of less than 5 s was realized. In addition, this sensor was not affected by humidity.

Solvatochromic effect (shift of max of fluorescence)

An integrated optical fibre sensor system, which allows in-situ non-destructive long-term monitoring of concrete structures has been developed (Grahn et al. 2002). A pyridinium-N-phenolat betainital dye was used as a moisture indicator. This dye shows strong solvatochromic behaviour in the ultraviolet-visible spectral range. The dye is embedded in a polymer matrix, whose moderate polarity is enhanced by free water diffusing into the sensor. This leads to a continuous hypsochromic shift of the absorption spectrum according to the water concentration. Another appropriate dye is 4-amino-N-methylphthalimid, which shows a similar behaviour in its fluorescence spectrum. Derivatives of this dye and suitable polymer matrices are reported to be under development.

1.2.2.2 Measurement of absorption via the evanescent field

Fibre optic evanescent field spectroscopy for in situ monitoring of pH levels has been investigated (Ghandehari and Vimer 2004). The cladding of plastic clad silica fibre is replaced with polymethylmethacrylate doped with pH-sensitive chromoionophores. The chromoionophores include methyl red, thymol blue, and thymolphtalein for pH in acidic, neutral and basic environments, respectively. The evanescent wave is used to selectively excite the indicator molecules within the fibre cladding for sampling aqueous media surrounding the fibre. This evanescent wave optical fibre sensor was explored for non-destructive detection of chemical species that contribute to degradation of civil infrastructure materials and could possibly be used for quasi-distributed detection of pH ranging from the acidic to basic.

For the determination of the pH-value of concrete, which is of major importance for the assessment of acidic attacks, an optical fibre sensor system has been developed (Grahn et al. 2002). The system consists of pH-indicator dyes immobilized in a highly hydrophilic polymer matrix. The doped polymer was used to coat a declad optical fibre to construct the evanescent optical fibre sensor. Any change in pH-value of the wet concrete material is indicated by a colour change of the dye/polymer system. The sensor system displays long term stability even in aggressive media of pH 12-13.

1.2.3 Direct measurement of changes in absorption and reflection

A method (Fuhr and Huston 1998) of corrosion monitoring relying on direct spectroscopy of corroded/uncorroded materials used the "twin-fibre" technique with separate transmit and receive fibres. A point corrosion sensor was demonstrated in the experiment using the "twin-fibre" bundle. The presence of corrosion is determined via colour modulation of a broadband input signal. The attributes and benefits associated with using optical fibres are realized in a separate experiment with the use of a fibre that has been selectively "windowed" using a wet timed glass etching method. In such a scheme time-resolved analysis can be employed to determine the amount of corrosion that occurs within each window segment of the fibre.

A similar simple technique (Singh et al. 2000) was based on the colour matching principle to detect corrosion induced colour changes. It employs a thin Y-shaped fibre optic bundle, which increases the quantity of light energy coupled from a white light source. The light reflected from the sample is incident on a PIN photo-detector through a complementary filter cutting the appropriate wavelength range. A series of such probes can be safely embedded and/or bonded to structures at pre-determined locations. This sensor was implemented and its feasibility for in-situ corrosion detection in structures was demonstrated. Measurement data was acquired for steel samples corroded both in concrete and under open ambient conditions.

1.2.4 Microbending based sensor

The simplest loss mechanism, which can be used for sensing purposes, is microbending, because a deliberately introduced microbend can provide a potentially useful sensor system. The work of (MacLean et al. 2003) describes a chemically reactive system in which the thin active coating on multimode graded-index fibre responds to a particular liquid species by expanding and thus introducing a microbend through the helical wrap, which cause losses in the light propagating through the optical fibre. By varying the active layer, sensors capable of detecting moisture and liquid hydrocarbons have been demonstrated. The benefits of these systems lie in their ability to address long interaction lengths and locate events quickly (within seconds) with relatively high precision (within a few meters) using a simple short range OTDR and a relatively inexpensive cabling format.

1.2.5 Total internal reflection change due to corrosion of metal coating

As light propagates along a fibre due to total internal reflection at the core/cladding interface, any changes to this interface should result in a change in transmission. Thus, if the normal cladding is removed from the sensing region and replaced by a metal layer, the boundary of total internal reflection disappears at that point because of absorption by the metal film. In this way, the amount of output light will obviously decrease. As corrosion develops, the output power will increase again owing to a reduction in absorbed light until it reaches a stable situation; that is, the metal film disappears and total internal reflection is recovered. The corrosion rate of the metal film is affected by the concentration of the corrosive solution and by the corrosion time.

If the basic composition of the metal cladding is the same as the material of the investigated structure, the metal cladding will have similar corrosion behaviour. As the corrosion of the metal cladding continues, its optical properties are altered, in turn affecting the propagation of light in the fibre. By monitoring the change of light output from the fibre, one may estimate the rate and degree of corrosion (Dong 2005), (Dong et al. 2005), (Dong et al. 2007).

A corrosion sensor based on metal-coated optical fibre has also been used to monitor steel corrosion in reinforced concrete (Li et al. 2000). This type of sensor is not new; it was suggested in 1996 (Rutherford et al. 1996) and was tested by embedding in a structure that simulated the real environment. The results of the testing were unsatisfactory. It was found that the light attenuating mechanism in the sensor exposed to a salt spray environment is fundamentally different depending on whether the sensor is tested bare or when it is mounted on corroding aluminium. When the sensor was tested bare, the aluminium alloy plating on the core of the sensor gradually corroded away, leaving the core exposed to the relatively low index of refraction of the salt spray electrolyte. Thus, the sensor optical throughput increased as the corrosion progressed, as predicted. When the sensor was installed on a piece of corroding aluminium alloy, the corrosion by-products built up along the core as the aluminium alloy cladding corroded. The particulate or granular nature of the corrosion by-products served as scattering sites, causing a net decrease in optical throughput. Therefore the performance of this type of sensor would be unpredictable when applied to a real structure exposed to salt spray.

Also, the sensors were found to be very fragile and even with careful handling in a laboratory environment, the breakage rate was high (8 out of 24 broke).

A low-cost optical fibre humidity sensor (Bariain et al. 2000) has been designed that is based on the deposition of a gel (agarose) on a biconically tapered optical fibre and used as a refractometer. The refractive index of the agarose gel surrounding the tapered zone of the fibre responds to humidity changes. In this way, the transmitted optical power through the taper varies as a function of the relative humidity.

Alternatively, a mixture of swelling cellulose and hydrophobic polymer can be used as a sensitive cladding layer for plastic optical fibre (POF). Attachment of water molecules causes a change in refractive index. This POF type sensor can be easily fabricated by coating the cladding layer on the plastic fibre core. When exposed to humid air, the cladding produces a change from leaky to guided propagation depending on the relative humidity. The sensor showed good results over a wide humidity range (Muto et al. 2003). However, this sensor has a fast response time, which is not appropriate for corrosion monitoring where cumulative approach to water is a critical parameter.

1.3 Organic dyes for corrosion sensing

Table 1.1 summarises the information about organic dyes potentially useful for corrosion monitoring, as well as suitable to be implemented into an optical fibre detection system.

The list of dyes is divided into two main sections: firstly, dyes which can be used in fluorescence analysis, and secondly, dyes which can be used in colorimetric or absorption analysis. Both approaches have advantages and disadvantages. In an OTDR measurement, the finite fluorescence lifetime can limit spatial resolution; a limitation that does not occur with absorption.

Dyes 1, 2, 9, and 10 are suitable for use as corrosive environment sensors (pH). Dye 2 demonstrates an extremely wide sensing range. Also, dyes 1 and 2 have been incorporated in an optical fibre sensor construction.

All other dyes were chosen because of their ability to detect the presence of aluminium as an ion, which characterises the beginning of the corrosion process.

Because aluminium degradation is also a problem in many areas of health protection, environmental pollution detection and so forth, several reagents have been reported for the spectrophotometric determination of aluminium. Some of the reagents for aluminium ions detection are commercially available; for example, Stilbazo is available from Tokyo Chemical Industry Co. as a spectrophotometric reagent for aluminium ions and other metals. The International Organization for Standardisation (ISO) suggests the use of 8-hydroxyquinoline for the determination of aluminium. The 8-Hydroxyquinoline absorption and fluorescence wavelengths at ~400 and ~500 nm respectively can be made compatible with the existing distributed sensor system (Stoddart et al. 2005).

Every chemical mentioned in Table 1.1 requires particular conditions to work as an aluminium detection agent: pH level, presence of contaminants, solvent used, even some reagents which work as catalysts. Only one chemical (lumogallion) has been used directly in a corrosion detection system. The possibility to use other listed dyes in corrosion detection with an optical fibre sensing system also needs to be investigated.

Table 1.1. Organic dyes for corrosion sensing

№	Common name (chemical name, chemical group)	Excitation wavelength	Fluores-cence wavelength	pH range	Other issues	Chemical structure of Dye	Ref
Fluorescence sensing							
1	5-(and-6-) carboxysuccinimidyl ester (SNAFL-SE)	490 nm	540/650 nm	6.2 - 8.6	pH sensing application pH sensitive dye SNAFL was covalently bound to the distal end of the fibre surface	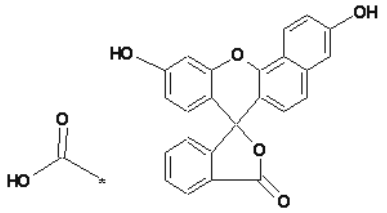	(Szunerits and Walt 2002)
2	Carboxy seminaphthofluorescein (SNAFL-2)	550 nm	640 nm	3 - 11	pH sensing application, membrane for the fiber-optic sensor.	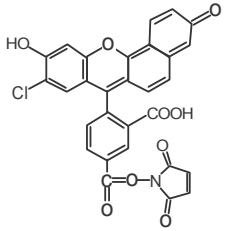	(Xu et al. 1998)
3	Morin	430 nm	500 nm	7	Al^{3+} ion detection; imaging fibre with covalently bonded morin	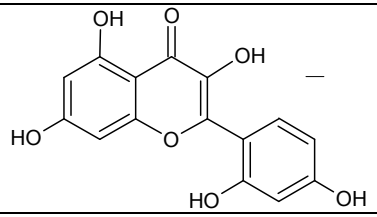	(Szunerits and Walt 2002)

№	Common name (chemical name, chemical group)	Excitation wavelength	Fluores-cence wavelength	pH range	Other issues	Chemical structure of Dye	Ref
4	Near Infra Red (NIR) dyes	670 nm	750 nm	Not specified	Ion detection Al^{3+}, Fe^{3+}, fluorescence quenching	TG1 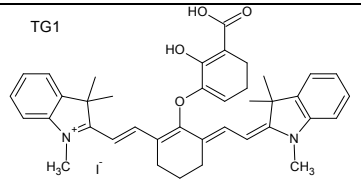 TG2 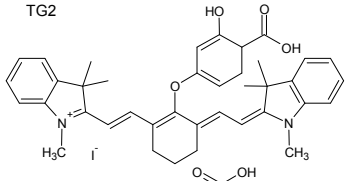 TG3 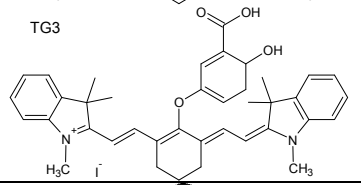	(Chin et al. 1996)
5	Ferron Iodoxyquinolinesulfonic acid	370 nm	Not men-tioned	5	Complexes with Al^{3+}, Fe^{3+} ions	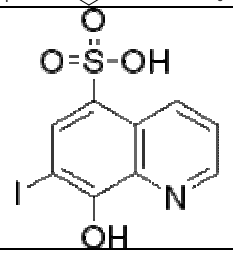	(Zhou et al. 2006), (Campa et al. 1988)
6	Pontachrome Blue Black R (Alizarine Blue Black R, Mordant Black 17)	500 nm	Orange-red fluorescence 634-698 nm	Not men-tioned	Interference with Fe^{3+} ions	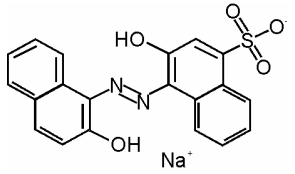	(Block and Morgan 1962)

№	Common name (chemical name, chemical group)	Excitation wavelength	Fluores-cence wavelength	pH range	Other issues	Chemical structure of Dye	Ref
7	Quercetin	450 nm	490 nm	Not men-tioned	Al^{3+} ion detection	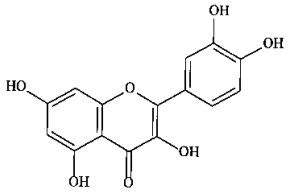	(Chang et al. 2003)
8	N-o-vanillidine-2-amino-p-cresol	423 nm	553 nm	4.0	Al^{3+} ion detection	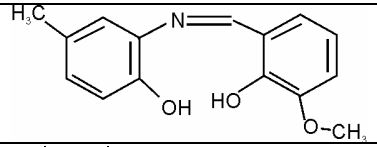	(Kara et al. 2007)
9	8-Hydroxyquinoline	350-400 nm	520 nm	Not stated	Al^{3+} ion detection	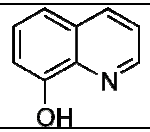	(McAdam et al. 2005)

№	Common name (chemical name, chemical group)	Absorption wavelength peak	pH range	Other issues	Chemical structure of Dye	Ref
Absorption sensing						
10	Derivative of dimethylindolenine bromide	780-800 nm	10 - 16	pH sensing application; dye entrapped within a Naflon matrix and fabricated into thin film.	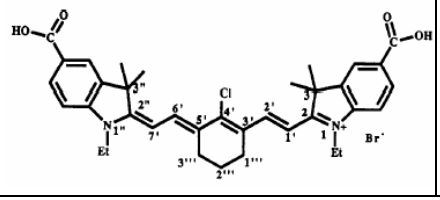	(Zen and Patonay 1991), (Zen et al. 1992)

№	Common name (chemical name, chemical group)	Absorption wavelength peak	pH range	Other issues	Chemical structure of Dye	Ref
11	Trimethynecyanine	900 nm	0.4 – 4.4	pH-sensing application	Not shown, supposedly is similar to previous	(Murphy et al. 1996)
12	Pyrocatechol Violet	500 nm	Exactly 6.10	Indicator for metal titration; with pH > 6 acts as a pH sensor, with pH < 6 – incomplete complexation	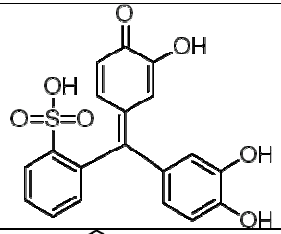	(Wauer et al. 2004)
13	Eriochrome cyanine R	535 nm	Not stated	Eriochrome cyanine R combines with aluminium to produce change in colour.	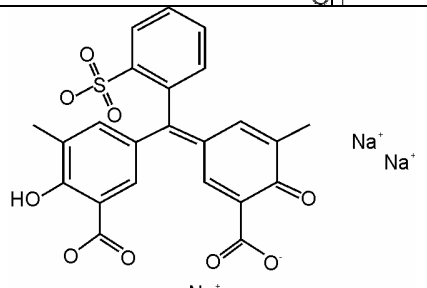	(Hill 1959), (Amelin and Gan'kova 2007)
14	Chrome Azurol S (Mordant Blue 29)	600 nm	6	Al^{3+} ions detection pH dependent optimum pH 6	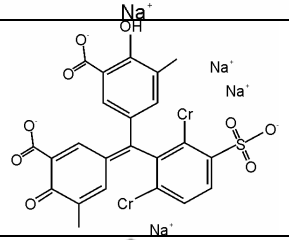	(Maleki et al. 2004), (Nadzhafova et al. 2001)
15	Xylenol Orange	400-600 nm	5-6	Al^{3+} ion detection pH dependent	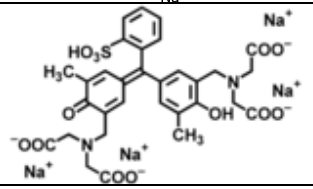	(Madrakian et al. 2005)

№	Common name (chemical name, chemical group)	Absorption wavelength peak	pH range	Other issues	Chemical structure of Dye	Ref
16	5,8-dihydroxy-1,4-naphthoquinone	600 nm		Determination of beryllium and aluminium ions	Not shown	(Agnihotri et al. 1993)
17	Alizarin	510-570 nm	5.5-7.5	Al^{3+} ion detection	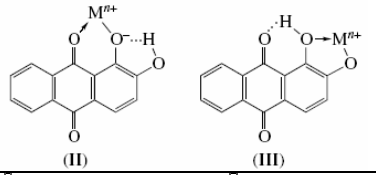	(Fain et al. 2004)
18	Aluminon	530 nm	6–7	Change in colour, may be used in fluorescent measurement, with short wave excitation	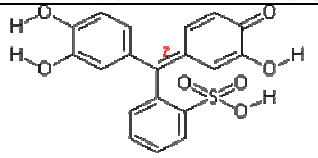	(Clark and Krueger 1985)
19	Bis-(2,3,4-Trihydroxyphenylazo) benzidine	455 nm	4.8-5.3	In the presence of nitrogen-containing organic reagents, the best medium for the complexation is shifted to the acidic region (pH 2).	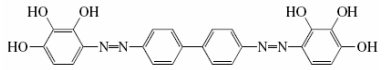	(Alieva et al. 2006)
20	2,2′,3,4-Tetrahydroxy-3′-sulpho-5′-nitroazobenzene	479 nm	4.0	Al^{3+} ion detection	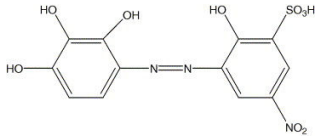	(Guray et al. 2005)

№	Common name (chemical name, chemical group)	Absorption wavelength peak	pH range	Other issues	Chemical structure of Dye	Ref
21	Stilbazo	413 nm	5.0	Spectrophotometric reagent for Al^{3+} ions and other metals from Tokyo Chemical Industry Co.	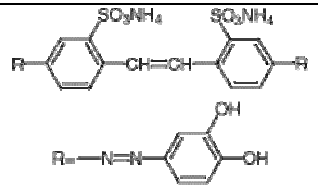	(C.U. Wetlesen and Omang 1961)

1.3.1 Aluminium corrosion monitoring by fluorescence of Alq_3

Because aluminium-based alloys are widely used in the production of aircraft components, one of the by-products of the corrosion process is aluminium cations. Previous work using fluorescence techniques has focussed on the detection of aluminium cations as an indication of the early stages of corrosion. The indicator 8-Hydroxyquinoline (8-HQ) has shown promising properties for the detection of aluminium cations and a point optical fibre sensor was built using 8-HQ as a transducer (McAdam et al. 2005).

From the sensing point of view, 8-HQ forms a stable complex with aluminium ions (Alq_3 - Figure 1.2) with changes to its absorption and fluorescence properties as shown in Figure 1.3. Excitation at 405 nm is ideal in this case, because it corresponds to the strong absorption line of the 8-HQ/Al^{3+} complex (Alq_3) and effectively excites fluorescence of Alq_3, but at the same time it is not absorbed by 8-HQ.

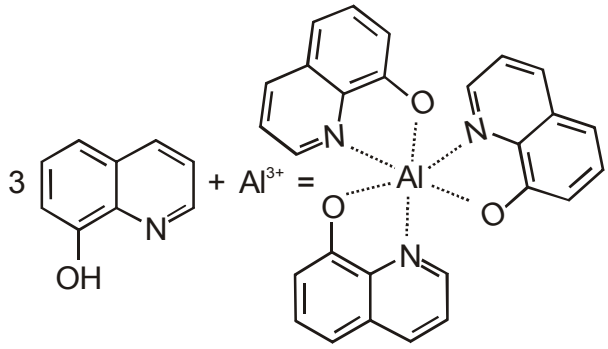

Figure 1.2. Corrosion detection reaction: 8-HQ forms the complex Alq_3 when exposed to Al^{3+}. Adapted from (McAdam et al. 2005).

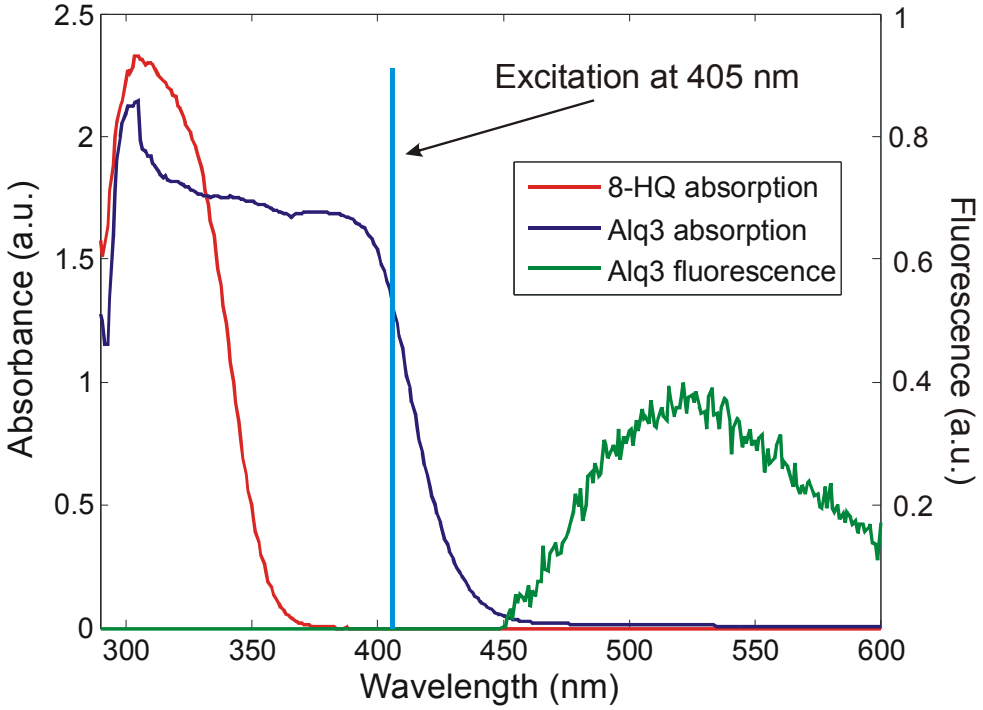

Figure 1.3. Spectral absorption and fluorescence characteristics of 8-HQ and its complex with aluminium (Alq_3) in cuvette.

1.3.2 Immobilization of dyes

Suitable polymers are required to provide a solid support for indicator dyes together with permeation of the species of interest. The most widely used polymers (Wolfbeis 1997) are:

- silicones,
- hydrophobic polymers, e.g. poly(vinyl chloride),
- polyethylene,
- silica materials,
- hydrophilic materials, e.g. so-called hydrogels.

Immobilization methods of indicator dyes include:

- physical entrapment,
- covalent binding,
- electrostatic binding and adsorption.

The application of sol-gel materials to optical fibre sensors, especially in the form of thin films, has attracted considerable interest because of the ease of fabrication and design flexibility of the process. The nature of the sol-gel process lends itself very well

to the deposition of thin films using a variety of techniques such as dip-coating, spin-coating, and spraying. In many sensor applications, the sol-gel film is used to provide a microporous support matrix in which analyte-sensitive chromophores are entrapped. Smaller analyte species may then diffuse into the matrix and interact with the chromophore. Sol-gel films have many advantages as support matrices over polymer supports, including strong adhesion, good mechanical strength, and excellent optical transparency (MacCraith and McDonagh 2002).

As mentioned above, many optical sensors, both absorption and fluorescence based, use waveguiding principles. Many optical-fibre based evanescent-wave sensors employ a thin, porous sol-gel film that is doped with an analyte-sensitive reagent and coated on a length of de-clad optical fibre. The amount of evanescent power that can interact with the fluorophore is critically dependent on the refractive indices of the fibre core and sol-gel cladding. Hence, the ability to tailor the sol-gel refractive index is crucial to optimizing sensor performance. Typically, a porous silica sol-gel film has a refractive index of about 1.43 but this value can be adjusted by choice of process parameters such as sol pH, ageing time, and, in particular, the sol-gel precursor (MacCraith and McDonagh 2002). A number of investigations of polymer or sol-gel entrapped materials for optical sensing have been reported (Kao et al. 1998, Wallington 1997, Arregui 2002).

1.4 OTDR for distributed sensing

Optical time domain reflectometry (OTDR) is a well established technique for the characterization of fibre optic communication systems. Physical parameters at every point along the fibre can be obtained by measuring from one end of the fibre. This method can also be used with a chemically sensitive optical fibre. Typically, a short excitation pulse is launched into the fibre and the time delay of reflected light that is guided back down the fibre due to scattering by physical or chemical ‘defects’ in the cladding is analysed. Thus, in principle, it should be possible to detect the presence and spatial distribution of an analyte along the active length of the fibre (Rogers 1999).

The possibility of using OTDR principles in sensing systems is well presented in the literature. Distributed strain measurements using strain-induced attenuation in optical fibre have been reported in (Kurashima et al. 1997) and (Schaefer et al. 1996).

Use of a fibre optic distributed sensing system employing multiplexed bragg gratings to monitor structural fatigue in an aircraft has been reported in (Duncan et al. 2003).

Distributed optical-fibre chemical sensing systems are of interest for monitoring broad-area chemical distributions. Different techniques have been investigated to show the potential of optical fibre distributed chemical sensing based on measuring changes in refractive index, absorption and fluorescence (Buerck et al. 1996), (Mendoza et al. 1995), (Lieberman et al. 1989), (Mukamal et al. 2005), (Cordero et al. 2005).

It has been shown that distributed chemical sensors can be achieved by immobilizing suitable reagents in the cladding of plastic-clad silica (PCS) optical fiber (Cordero et al. 2006b), (Cordero et al. 2006a), (Potyrailo et al. 2005), (Potyrailo and Hieftje 1999). Despite the number of potentially important applications, relatively few practical distributed chemical sensing systems based on evanescent field interactions have been reported. This is primarily due to the difficulty of protecting the optical fibre waveguide while allowing sufficiently sensitive interaction between the target chemical species and the guided light in the fibre core. Some new methods for signal generation and processing in distributed chemical sensing based on absorption measurements have been introduced (Potyrailo and Hieftje 1998a) to improve dynamic range and sensitivity of the detection system.

Distributed optical fibre fluorosensors for pH measurement were presented in the literature (Wallace et al. 1997), (Browne et al. 1996). This approach did not receive much further development due to issues with sensitivity, stability, and fluorescence lifetime effects, despite the fact that some work has been done to improve detection parameters such as spatial resolution (Potyrailo and Hieftje 1998b). An approach based on OTDR was employed to build a compact detection system for simultaneous multi-component fluorescent chemical analysis (Henning et al. 2005).

Nevertheless, fluorescence-based techniques potentially provide a powerful transduction mechanism for chemical events, with a large number of fluorescent indicators available to detect a wide range of chemical species.

1.4.1 Apparatus for distributed measurements

The "Sentor" optical fibre distributed temperature sensor (DTS) developed by Tyree Optech and Swinburne University can be modified for use in corrosion detection (Stoddart et al. 2005). The Sentor DTS uses high-speed electronics for the laser drive and photon detection circuits. A sensitive photomultiplier tube (PMT) detector provides the advantages of the photon counting method to simplify all aspects of operation. The time-gated electronics for signal acquisition accumulate the photon counts in bins of 2 ns width, which corresponds to a length resolution of 0.2 m in silica fibres. An increase in the accumulation time can be used to improve the signal to noise ratio. A detailed description of the Sentor optical fibre distributed temperature sensor can be found in Appendix 1.

A number of distributed optical fibre sensors are available in the commercial market, including several Raman scattering based sensors for temperature sensing only. Examples are listed below and details are available on the Internet:

- SensorTran;
- Weatherford's optical distributed-temperature-sensing.

Distributed optical fibre sensors based on Brillouin scattering for measurements of temperature and strain and using conventional telecommunication fibres are also available. Examples are listed below and details are available on the Internet:

- OZ Optics [Foresight DSTS (Distributed Strain and Temperature Sensors)]
- Omnisens (STA)
- Yokogawa (AQ8603)
- Sensornet (DTSS)
- Neubrex (Neubrescope)
- AP Sensing (former Agilent Technologies and Hewlett Packard) [Distributed Temperature Sensing]

A distributed optical fibre acoustic sensor for reservoir monitoring (Helios) was developed by Fotech Solutions. The Helios sensing system from Fotech consists of two elements: an optical fibre cable, and the Helios Interrogator which combines the high

sensitivity of optical fibre interferometers with the high spatial resolution of short pulse optical time domain reflectometry in single-mode optical fibre. Helios is designed to detect acoustic signals or vibration along the entire length of the installed optical fibre. The Helios distributed acoustic monitoring system was installed in a coal-bed methane well in Scotland for Composite Energy Ltd of Stirling, UK.

Distributed Intrinsic Chemical Agent Sensing and Transmission (DICAST) technology was developed by Intelligent Optical Systems, Inc. DICAST sensors have been developed for multiple chemical agents, including chemical warfare agents, and prototype systems are deployed at beta sites in Pennsylvania and California. The operating principle is understood to be based on optical absorption by the chemically sensitive cladding.

1.5 Summary and thesis outline

The work presented in this thesis aims to develop and investigate a detection system that has the potential to continuously monitor large-scale structures, together with the ability to non-destructively evaluate corrosion situations. It is preferable to be able to detect corrosion at the early stages in hidden or inaccessible areas. A way of achieving this goal is by combining optical fibre technology with developed chemical sensing of related parameters to provide an indirect indication of the presence of corrosion.

Development of a fully distributed sensing system can be set as an ultimate goal of this technology. The fully distributed sensing system would provide constant monitoring and measurements of the degree of corrosion at every location along the sensing fibre. Practical considerations and consultations with the end-user could set minimal requirements that should be satisfied for the sensing system to have a potential for further development. Because corrosion is a complicated process it is practical for the system to be able to detect corrosion rather than to measure it. Detection is understood in terms of the signal detection theory as a “yes/no” type of detection according to a preset threshold. The sensing system is required to be able to localize the corrosion point along the sensing fibre. The optical fibre sensor is required to have the potential to be installed in predetermined locations that are considered vulnerable to

corrosion. So, the proposed sensing system should be able to perform distributed detection at an arbitrary location along the sensing fibre. Such a sensor could be considered a fully distributed sensing system. On the other hand, installing the optical fibre sensor at particular places (like lap joints, etc.) gives an opportunity to consider the sensing system as a quasi-distributed system. Thus, development of a fibre optic distributed corrosion sensor which can detect corrosion at the preset threshold at any predefined location was set as an initial target. At the same time, the system should have the potential to be extended to a fully distributed capability in future work.

Prior to the experimental and modelling results, Chapter 2 provides a brief overview of the methods of designing an optical fibre sensor potentially suitable for distributed corrosion monitoring. In Chapter 3, the theoretical considerations and modelling that indicate critical design parameters for an ideal distributed chemical sensing system based on evanescent wave interactions are presented. In order to provide motivation for the use of the chosen optical fibre sensor design, an evaluation of the available techniques is given in Chapter 4. The aims of Chapter 5 are to theoretically and experimentally investigate the absorbance and fluorescence response of the multimode optical fibre evanescent wave sensor, together with the effect of excitation wavelength and the influence of launching conditions on the sensor performance. The experimental equipment, used for the distributed measurements, based on pulsed excitation and time-gated photon counting, are described in Chapter 6. The distributed detection system has been designed and used to locate a fluorescent region along the fibre. Also in this chapter a theoretical model is developed to characterize and predict the behaviour of the fluorescent response at the detector. A practical application in corrosion determination and characterisation of the designed detection system is the subject of Chapter 7. The final chapter combines a conclusion of the project and recommendations for further work.

Chapter 2

Methods

Employing optical fibre technology for corrosion monitoring requires optical fibre design making the fibre sensitive to the corrosive environment. This design should provide modulation of the light propagating in the fibre according to changes in the environment attributed to corrosion.

In this chapter, methods of designing an optical fibre sensor potentially suitable for distributed corrosion monitoring are described. Different approaches to modulation of light in the optical fibre due to a corrosive environment are presented. An approach based on water diffusion in the optical fibre provides direct detection of the water ingression by a change in spectral intensity of the propagating light. Another approach utilises chemical indicators for corrosion sensing as it has been described in Chapter 1. To realise such an approach, special optical fibre modification providing indicator-light interaction through the evanescent field is required.

2.1 Water diffusion into optical fibre

Optical fibres inherently have extremely low attenuation or transmission loss which has brought their wide acceptance as a medium of transmission. Nevertheless, there are some factors which cause light loss and limit how far a signal can travel through the fibre. Total attenuation consists of material absorption, Rayleigh scattering in the fibre and waveguide imperfections.

Material absorption can be divided into two categories: intrinsic absorption losses and extrinsic absorption. Regular telecommunication optical fibres are made from ultra-pure fused silica glass with special dopants to obtain the desired indices of refraction needed to guide light. Germanium, titanium, or phosphorous are added to increase the core refractive index; whereas boron or fluorine are added to decrease the refractive

index of the cladding. So, intrinsic absorption can be associated with absorption by fused silica, for which electronic resonances occur in the ultraviolet region (wavelength < 0.4μm), whereas vibrational resonances occur in the infrared region (wavelength > 7μm). Extrinsic absorption on the other hand corresponds to losses caused by impurities within silica.

Different types of atomic defects in the silica fibres lead to additional losses appearing over time. There are called aging losses. These silica defects can react with trace amounts of hydrogen even at room temperature and cause significant losses at 1383 nm which corresponds to the hydroxyl (OH^-) absorption peak and at 1530 nm associated with the absorption peak caused by the Si-H bond vibration (Chang 2005).

The main source of extrinsic absorption in fibres is the presence of water vapour. A vibrational resonance of the OH^- ion occurs near 2730 nm. Its harmonic and combination tones with silica produce absorption at 1383 nm, 1244 nm and 950 nm wavelengths. The presence of residual water vapour in silica causes aging losses in the fibre as well as increasing extrinsic absorption losses.

Typical optical fibre spectral attenuation is shown in Figure 2.1 (Schubert 2006). The absorption peak around 1400 nm is associated with vibrational states of O-H bonds in the glass as well as in the water molecules present in the fibre as a contaminant and is called the “water peak”.

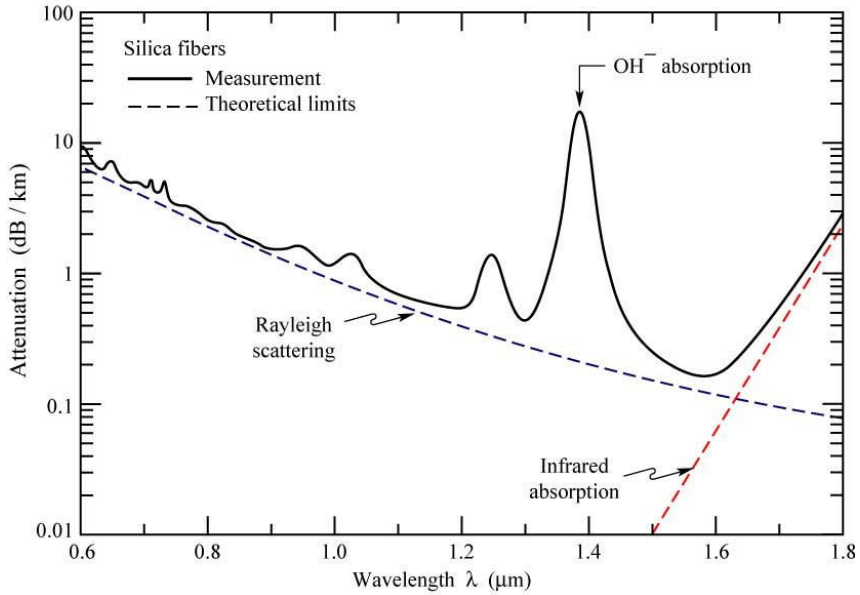

Figure 2.1. Measured attenuation in silica fibres (solid line) and theoretical limits (dashed lines) given by Rayleigh scattering in the short-wavelength region, and by molecular vibrations (infrared absorption) in the infrared spectral region (Schubert 2006).

Great efforts have been put into reducing water contamination in optical fibres during the manufacturing process. Recent advances in manufacturing have resulted in so called zero-water-peak fibres. Examples of these fibres include: SMF-28e^{+} from Corning, the Furukawa-Lucent OFS AllWave, Pureband Zero Water Peak Fibre from Sumitimo Electric Lightwave.

Consequently, changes in the intensity of the "water peak" could potentially be used as an indicator of water ingression. Monitoring of the "water peak" intensity over time may allow the presence of water around the fibre to be detected as an indication of a corrosive environment development.

In principle, this could be monitored by a modified optical time domain reflectometer (OTDR) operating at 1400 nm.

2.2 Coupling via evanescent field

An evanescent field is created whenever light undergoes total internal reflection at the boundary between two dielectric media. In planar media, the evanescent field decays exponentially away from the boundary into the lower index medium, with a decay constant dependent on the indices and the angle of incidence.

To characterise the evanescent wave a penetration parameter was introduced. The penetration depth d_p is defined as a distance, into optically rare medium, at which the amplitude of the evanescent wave decreases to 1/e of its initial value and can be given by

$$d_p = \frac{\lambda}{2\pi n_1 \sqrt{\sin^2 \theta_c - \sin^2 \theta_z}}, \tag{2.1}$$

where λ is the light wavelength, n_1 and n_2 are the refractive indices of the dielectric media with $n_2 < n_1$, θ_z is the angle complimentary to the incident, θ_c is the angle complimentary to the critical angle for total internal reflection, and it is defined as

$$\theta_c = \arccos \frac{n_2}{n_1}. \tag{2.2}$$

For the fused silica (n=1.458)/water (n=1.333) system and for VIS range (380-780 nm), the average value of d_p is about 250 nm, but for the angles close to the critical angle d_p exceeds 1 μm. This value is enough to provide interaction with the molecules at the boundary and enables recording those absorption or emission spectra. It establishes a basis for the well known technique referred to as attenuated total reflectance spectroscopy.

Optical fibres and waveguides may be considered, in simple terms, as guiding light through total internal reflection and therefore have an evanescent field extending from the core/cladding boundary along their entire length. This provides a useful means of interacting with the guided light without interrupting the fibre path. Coupling between two or more waveguides may be performed via the evanescent field in suitable configurations. Waveguides may be designed in such a way as to allow the evanescent field to interact with an absorber or fluorescent dye, forming the basis for many optical chemical sensors (Stewart and Johstone 1996).

Further, we describe optical fibre sensor constructions developed to date with special attention to those potentially useful in the distributed measurements.

2.2.1 Exposed core fibre

Plastic-clad-silica (PCS) multimode fibres are the most commonly used in the development of optical fibre chemical sensors. The simplest and cheapest method of sensor construction is when the plastic cladding is removed over a suitable fibre length, exposing the core and allowing access to the evanescent field. Another arrangement is a fibre surrounded by a cladding that has been impregnated with chemically active species. Both approaches are widely presented in the literature; advantages and problems are discussed and solutions suggested (Ruddy et al. 1990), (MacCraith et al. 1991), (Potyrailo et al. 1996), (Ghandehari and Vimer 2004), (Lee et al. 2003), (Lee et al. 2001), (Kumar et al. 2002), (Orghici et al. 2008), (Börner et al. 2009).

Moreover, this type of optical fibre construction provides a platform to develop truly distributed sensing systems. The problem is that the low percentage of total power carried by the evanescent field results in poor sensitivity.

One way to overcome this problem is, for example, the tapered fibre which was developed to maximize interaction with the sensing region. The tapered fibre is produced by heating a section of single mode fibre in a methane/oxygen mixture flame and pulling the fibre as it melts (Moar et al. 1999). This tapered profile supports a modal structure that spreads out as it travels through the tapered region and extends into the medium surrounding the taper. It provides strong interaction with the surrounding area allowing efficient excitation of the species in the sensing region by the propagating light and possible coupling back via evanescent field. It allows the fibre taper to be used in a variety of applications including fibre dye lasers (Pendock et al. 1992), non-linear optical devices (Mackenzie and Payne 1990b), (Mackenzie and Payne 1990a) and optical fibre sensors (Anderson et al. 1994), (Hale and Payne 1997), (Foulgoc et al. 1996), (Falciai et al. 1997).

Tapered fibres have shown suitable sensitivity, but have limited application as distributed sensors; it is only possible to build a quasi-distributed system on the tapered fibre basis. In addition, the tapered regions are delicate and required special packaging.

A relatively new approach to solve this problem is based on improving the efficiency of the coupling to the surrounding region by using specially designed fibres. For example, maximization of the fraction of the total supported modal field power in

the evanescent field is possible by creating an optimal fibre refractive index profile (Gibson and Dower 2007).

Recent developments in the fabrication of micro- structured optical fibres suggest that the coupling efficiency can be significantly improved in fibre designs that maximises the evanescent field in the sensing area. Such designs were suggested and analysed theoretically (Zhu et al. 2006) and low loss and high sensing efficiency were predicted. An approach to evanescent field sensing, in which both core and cladding are micro-structured, is presented in (Cordeiro et al. 2006). The fibre was fabricated and tested, and simulations and experimental results were shown in the visible region to demonstrate the utility of this approach for sensing.

Micro-structured optical fibres can also be gainful for fibre-based fluorescence sensing thanks to the possibility of improving the sensing performance through fibre geometry optimisation and materials like high-index glasses. It has been shown that such fibres exhibit localised regions of high intensity which lead to approximately two orders of magnitude enhancement of fluorescence recapturing (Afshar et al. 2007). Experimental implementations of micro-structured optical fibre sensors are presented in the literature (Jensen et al. 2004), (Smolka et al. 2007). However, the evanescent field can generally only be accessed via the distal ends of the fibre. Consequently, distributed sensing is not possible unless the core is exposed.

Fluorescence-based distributed sensing using exposed-core micro-structured optical fibres was demonstrated in (Warren-Smith et al. 2010). A time-domain approach that uses photon counting detection was employed. The resolution was shown to be 0.5 m, with a range of up to 2.5 m. The improved efficiency provided by the specially designed fibre is accompanied by increased absorption losses, rendering this approach unsuitable for large detection ranges. It may be possible to improve the useful range by fabricating fibres with cleaner fabrication techniques or higher purity materials.

2.2.2 D-fibre and asymmetric waveguides

Removal of the cladding or tapering of the fibre results in a very fragile filament. As an alternative, a D-shaped fibre structure with the cladding removed all along the fibre length is another suitable candidate for distributed sensing. Such fibres are commercially available, but their evanescent sensing ability needs more detailed

investigation. Theoretical and experimental investigations have been performed to estimate and compare the detection efficiency of the different constructions (Marcuse et al. 1992), (Henry 1994), (Huntington et al. 1997).

A number of evanescent wave sensors have been developed on the base of D-shaped fibre. For example, in (Lee et al. 1996) a D-shaped optical fibre sensor was demonstrated as a surface contamination monitor for salt deposition on insulators. Optical fibre sensors using the evanescent field in D-fibre were used for temperature measurements (Chandani and Jaeger 2005), chemical sensing (Chen et al. 2005) and measurements of liquid level based on changes in refractive index (Chandani and Jaeger 2007).

In most cases, a reduction of the cladding thickness is required to provide effective evanescent field interaction, especially if short wavelengths are planned to be used for sensor excitation. Usually this is performed by wet etching with HF acid, which adds complications in the sensor production. Another possible solution is to mount the fibre in a curved slot cut in a quartz block, which is polished to produce a D-shaped structure on the fibre with half the cladding region removed (Kim et al. 2007). Other difficulties of employing D-fibre as a sensing element such as low sensitivity, second-harmonic background signals from interference effects, as well as the practical difficulty in splicing compared with standard (circular) fibre, were addressed in (Stewart et al. 1997). Surface contamination is another problem that should be taken into account when working with the D-fibre based sensors (Jin et al. 1995). At the same time, D-fibres still provide potential for truly distributed measurements.

Integrated optical waveguides may also be used as evanescent wave sensors. Integrated optical guides are usually asymmetric in structure (in terms of index distribution) and may be planar, two dimensional, single layer, or multilayer in form. For example, it has been shown (Draxler et al. 1996) that the combination of inhomogeneous waveguiding with lifetime-based sensing and imaging can be used for applications such as oxygen sensing. A complete integrated optical sensor system (Mendoza et al. 1996) has simultaneously identified and quantified traces of metal ions in a water stream. Despite the attraction of integrated optical waveguides for simultaneous chemical identification there is not much potential for them to be used in distributed sensing systems.

2.3 Summary

This Chapter presents information on the methods of optical fibre sensor design. Based on the information presented here, three methods will be further evaluated as potentially useful for distributed corrosion monitoring in Chapter 4. These methods are: the method based on spectral measurements of water ingress; the method standing on modification of the D shape fibre, and the method of the optical fibre sensor construction by exposure of the core of the plastic clad fibre.

In designing an effective distributed sensor, it is important to consider many factors such as: the nature and requirements of the particular application, the physical and chemical properties of the target species, and the parameters of the detection system, as these factors jointly define the detection system performance. In order to evaluate the potential benefits of the approach based on evanescent wave interaction in the optical fibre sensor, a model for an ideal distributed fluorescence sensing system based on photon counting detection is presented in the follow chapter.

Chapter 3

Modelling of an ideal distributed sensing system

In this Chapter, a concept of distributed measurement in optical fibre based on the technique of optical time domain reflectometry (OTDR) is investigated. OTDR is primarily used to evaluate loss and detect faults along a fibre. This system utilises an optical radar (or LIDAR, for light detection and ranging) concept to examine the continuity and attenuation of optical fibres, by measuring the characteristics of the backscattering against time when a short pulse of light is launched into a fibre waveguide.

Combining this idea with the concept of an intrinsically sensitive optical fibre, the design of a distributed chemical sensing system is suggested. One of the possibilities to design an intrinsically sensitive optical fibre is to develop a fibre with a specially modified chemically sensitive cladding. The chemically sensitive cladding may be created by doping a primary material with indicators (probes) – synthetic dyes that undergo changes of spectral-luminescent properties on interaction with chemical species.

A schematic of a fluorescence based OTDR is depicted in Figure 3.1. A pulsed laser is coupled into a section of fibre via a directional coupler, which also serves to couple the back-scattered light fraction, captured and returned via the intrinsically sensitive fibre on test, to the sensitive detection system with time resolving capability. The modified cladding region containing the fluorescent dye commences after the directional coupler at a range R_0. Optical energy generated by the fluorescent dye molecules in the cladding is coupled into the core by means of the evanescent field of the guided modes.

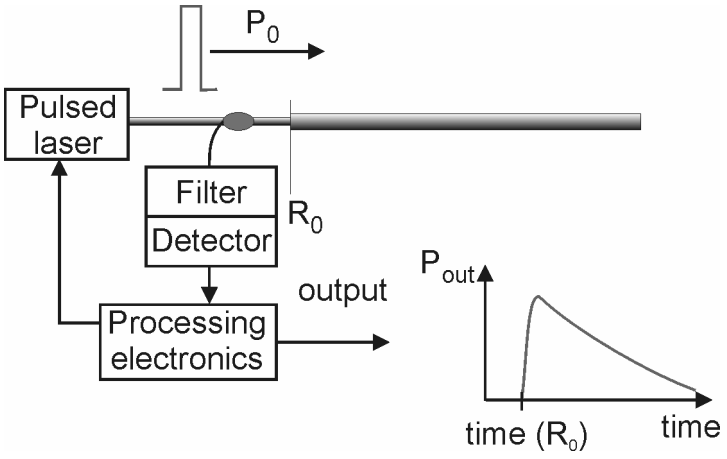

Figure 3.1. Detection system schematic.

3.1 LIDAR equation

The use of an optical fibre for range-resolved, remote detection is analogous to the laser radar technique, where single-ended measurements of materials in the atmosphere are made. For a laser radar system, the received power P_r in a spectral component of frequency ν_0 backscattered from an element at range R is described by the generalized laser radar equation. So, for instantaneous received power at time t from the distance R (Hinkley 1976):

$$P_r(R) = P_0(\nu_0) K \frac{c \cdot \tau}{2} \beta_\pi(R) \frac{A_r}{R^2} \exp(-2\int_0^R \alpha(r) dr) \tag{3.1}$$

where: $P_0(\nu_0)$ is the power of the laser pulse at frequency ν_0;

c is the speed of light;

τ is the pulse duration;

β_π is the volume backscattering coefficient of the tested media;

A_r is the effective receiver aperture;

α is the volume extinction coefficient of the tested media;

K is the efficiency of the total optical system.

3.2 Adaptation of LIDAR equation for fluorescence detection in optical fibre

In the case of fluorescence measurements, the detected signal has shifted wavelength relative to the laser emission. Therefore, the received signal should be registered at the fluorescence wavelength, which is determined by the spectral and

luminescent properties of the dye used as a fluorescent probe. The other significant component which the system receives is the Rayleigh backscattered signal, which can be several orders higher than the fluorescence signal. Using high quality optical filters, similar to those used in Raman temperature sensing applications, allows efficient rejection of the Rayleigh component in the detection channel.

The generalized laser radar equation allows for the received signal power to decrease as the inverse square of the range, as required for divergent scattering from a point source. This factor is not applicable in an optical fibre, due to the guided nature of the received light. Therefore the power detected at a range R in a fluorescence-based distributed sensing system is:

$$P_r(\nu_f, R) = P_0(\nu_0) K \beta \exp(-\alpha_0 R) \exp(-\alpha_f R) \frac{c\tau}{2n} \tag{3.2}$$

where: ν_0 and ν_f are the frequencies of excitation and fluorescence respectively;

P_0 is the power of the laser pulse at frequency ν_0;

K is the efficiency of the total optical system;

β is the parameter which characterizes the efficiency of the interaction between light propagating in the optical fibre and the fluorescent material;

$\exp(-\alpha_0 R)$ and $\exp(-\alpha_f R)$ are the transmittances at the excitation and fluorescence wavelengths;

$\frac{c\tau}{2n}$ is the effective length of resolution;

n is the effective optical fibre refractive index;

$\tau = \tau_p + \tau_s + \tau_c$ determines the spatial resolution of the detection system,

τ_p is the laser pulse length;

τ_s is the response time of the optical interaction with the fluorescent species;

τ_c is the time resolution of the detection system.

The range R is related to the observed time delay t by

$$R = \frac{ct}{2n}. \tag{3.3}$$

3.2.1 K – the efficiency of the total optical system

The efficiency characterises the extraneous losses in the optical system, e.g. splicing losses, light coupling losses. As a first approximation, K can be assumed equal to one (i.e. no losses).

3.2.2 Evanescent field interaction

Gloge (Gloge 1971) has shown that, based on the weakly guided approximation, the ratio of powers propagating in the core and cladding regions depends strongly on the particular mode propagating in a fibre. The weakly guiding approximation assumes that the refractive index difference Δ between the core and cladding is small ($\Delta = \frac{n_{co} - n_{cl}}{n_{cl}} << 1$, n_{co} and n_{cl} are the core and cladding refractive indices). The relationship between the power propagating in the core (P_{core}), the power propagating in the cladding (P_{clad}) and total power $P = P_{core} + P_{clad}$ is plotted in Figure 3.2 according to Gloge. The dimensionless parameter V, appearing in Figure 3.2, is known as the waveguide parameter or waveguide frequency. It is defined as $V = \frac{2\pi\rho}{\lambda}\sqrt{n_{co}^2 - n_{cl}^2}$, where λ is the wavelength of the propagating light, ρ is the diameter of the fibre core.

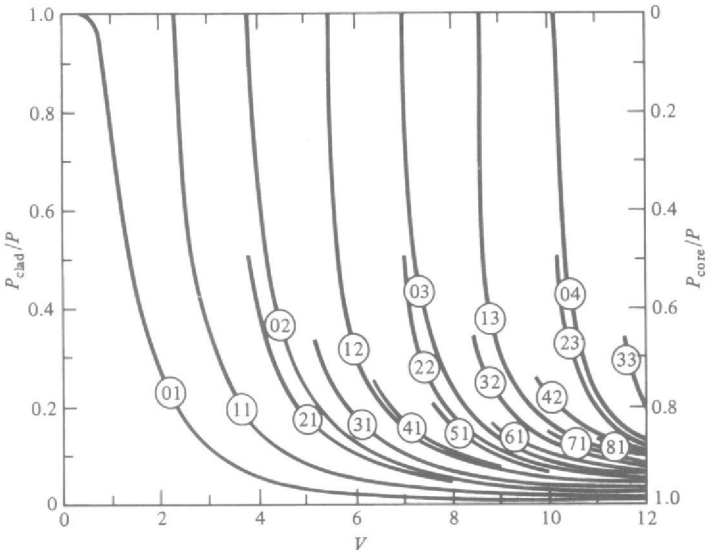

Figure 3.2. Fractional power flow in the cladding and in the core of a step-index optical fibre as a function of the V number (reproduced from (Gloge 1971)).

In the same reference, it has been shown that the average value of the ratio P_{clad} / P is given by $\frac{4\sqrt{2}}{3V}$ for weakly guiding multimode fibres where all modes are propagating. Although in reality a sensor might not comply with the weakly guiding condition and might not be mode-filled, the expression above gives an estimate of the fraction of guided power available for evanescent wave sensing. For example, a conventional multimode fibre, with core diameter of 50 μm, numerical aperture (NA) of 0.2 and excitation wavelength λ_0 = 780 nm, has $V \approx 80$ and $P_{clad} / P \approx 2$ %.

3.2.3 Transmittance of optical fibre

As light travels along a fibre, its power decreases exponentially with distance. If $P(0)$ is the optical power in a fibre at the origin (at $z = 0$), then power $P(z)$ at a distance z further down the fibre is

$$P(z) = P(0)\exp(-\alpha z), \tag{3.4}$$

where

exp(-αz) is the fibre transmission, and

$\alpha = \frac{1}{z}\ln\left[\frac{P(0)}{P(z)}\right]$ is the fibre attenuation given in appropriate units, such as km^{-1}.

The basic attenuation mechanisms in a fibre are absorption, scattering, and radiative losses of the optical energy. Absorption is related to the fibre material, whereas scattering is associated with both the fibre material and imperfections in the optical waveguide. Attenuation owing to radiative effects originates from perturbations (both microscopic and macroscopic) of the fibre geometry. All of these processes have a strong wavelength dependence.

Ultraviolet absorption decays exponentially with increasing wavelength and in the visible and near-infrared region below 1.2 μm the absorption losses is small compared with scattering loss. In the near-infrared region above 1.2 μm, the absorption loss is predominantly determined by the presence of OH^- ions and the inherent infrared absorption of the constituent materials (see Figure 1.2 in Chapter 1).

Scattering in glass occurs mainly due to variation in the refractive index, which is Rayleigh-type scattering, and follows a characteristic λ^{-4} dependence. For wavelengths

below about 1 μm, it is the dominant loss mechanism in a fibre and results in decreasing attenuation with increasing wavelength.

3.2.4 Attenuation by core and cladding

Since light propagates in the core and cladding regions simultaneously, the attenuation of both should be taken into account. Because core and cladding have different composition, and therefore different indices of refraction, the core and cladding generally have different attenuation coefficients, denoted α_{core} and α_{clad}, respectively. If the influence of modal coupling is ignored, the loss for a particular mode in a step-index waveguide is:

$$\alpha = \alpha_{core} \frac{P_{core}}{P} + \alpha_{clad} \frac{P_{clad}}{P}, \tag{3.5}$$

where the ratios P_{core} / P and P_{clad} / P can be estimated as in Section 3.2.2.

This is especially important in our modelling due to the fact that we are considering a cladding doped with a fluorescent material that has a significant absorption coefficient compared to conventional optical fibre materials. We assume that the main attenuation mechanism that applies in the cladding is absorption by the fluorescent material, while the attenuation in the core region is defined mainly by the Rayleigh scattering mechanism. Also, the attenuation of undoped optical fibre materials is small compared to the loss due to absorption by the fluorescent dye in the optical fibre cladding material (α_{abs}). In this case:

$$\alpha_{clad} = \alpha_{abs} \text{ and } \alpha_{core} << \alpha_{clad}. \tag{3.6}$$

Taking into account the fact that $P_{core}+P_{clad}=P$ and the conditions (3.6), we can rewrite (3.5) as:

$$\alpha = \alpha_{core} + (\alpha_{clad} - \alpha_{core}) \frac{P_{clad}}{P} \approx \alpha_{core} + \alpha_{abs} \frac{P_{clad}}{P}. \tag{3.7}$$

We consider the situation where the fluorescent dye effectively absorbs at the excitation wavelength, while its absorption at the fluorescence wavelength can be neglected. So, optical fibre attenuation in our model is:

$$\alpha = \alpha_{core}^{0} + \alpha_{core}^{f} + \alpha_{abs}\frac{P_{clad}}{P}, \text{ and } \alpha_{core} = \alpha_{core}^{0} + \alpha_{core}^{f}, \tag{3.8}$$

where α_{core}^{0} and α_{core}^{f} are the attenuation coefficients of the fibre core at the excitation and fluorescence wavelengths, respectively. In this case, the optical fibre transmission in our model can be written as:

$$T = \exp\left(-\alpha_{core}^{0}R\right)\exp\left(-\alpha_{core}^{f}R\right)\exp\left(-\alpha_{abs}\frac{P_{clad}}{P}R\right) \tag{3.9}$$

The attenuation coefficient α_{abs} depends on the concentration (molar concentration, N_{conc}) and absorption characteristics (the molar absorption coefficient, ε) of the fluorescent dye, so $\alpha_{abs} = N_{conc} \cdot \varepsilon$.

In general, the sensitive range will be limited by absorption in the modified cladding. Therefore, the transmission losses that occur in the unmodified sections of the detection system (see Figure 3.1) can effectively be ignored for short distances in good quality optical fibres.

3.2.5 Interaction between the evanescent field and fluorescent material

The parameter β in Equation (3.2) characterizes the efficiency of the interaction between light propagating in the optical fibre and the fluorescent material. It is the fractional amount of the incident energy launched back from the cladding via the evanescent field after absorption and fluorescent emission processes have occurred. In an optical fibre evanescent wave sensor this process consists of four steps: 1) coupling part of the propagating energy into the cladding region, 2) absorption of the energy at the excitation wavelength by the fluorescent dye, 3) re-emission by the fluorescent dye at the fluorescence wavelength, and 4) coupling the re-emitted light back into the core region.

The first process – coupling part of the propagating energy into the cladding region – can be characterized by the P_{clad}/P ratio as shown in Section 3.2.2. Absorption of the fluorescent dye is determined by the molar absorption coefficient (ε) and molar

concentration (N_{conc}) of the dye, while re-emission is given by the dye's fluorescent quantum yield (φ_f).

For the fourth process, we use the term "collection efficiency" (γ) from Marcuse (Marcuse 1988) where it is defined as the ratio of light collected in the fibre core relative to the total amount of light radiated by the sources, in the absence of the fibre core. Marcuse presented a theoretical study using computer simulation. The interaction between light sources in the fibre cladding and the evanescent field tails of the guided core modes were characterized by means of a wave optics approach and hence the possibility to transfer some energy between them. Note that it is not sufficient for light emitted by a source on the cladding to fall within the collection angle of the fibre core, as this process cannot couple into a stable guided core mode. Figures 3.3 and 3.4 show the results of the simulation for two different situations: in Figure 3.3, the light sources are assumed to be uniformly distributed throughout the cladding; in Figure 3.4, all light sources are assumed to be concentrated in a very narrow region near the core-cladding interface. Using these plots, we can estimate the efficiency of the fourth step - collection of re-emitted light back into the core region.

Thus, the efficiency of the interaction between light propagating in the optical fibre and the fluorescent material can be written:

$$\beta = \frac{P_{clad}}{P} \varepsilon N_{conc} \varphi_f \gamma \tag{3.10}$$

and the detected power becomes:

$$P_r(\nu_f, R) = P_0(\nu_0) K \beta \exp\left(-\alpha_{core}^0 R\right) \exp\left(-\alpha_{core}^f R\right) \exp\left(-\varepsilon N_{conc} \frac{P_{clad}}{P} R\right) \frac{c\tau}{2n} \tag{3.11}$$

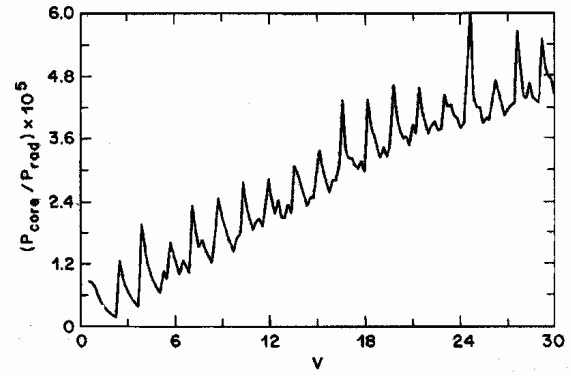

Figure 3.3. Light collection efficiency (γ) of a positively guiding fibre as a function of V number. The light sources are distributed uniformly in the cladding region (reproduced from (Marcuse 1988)).

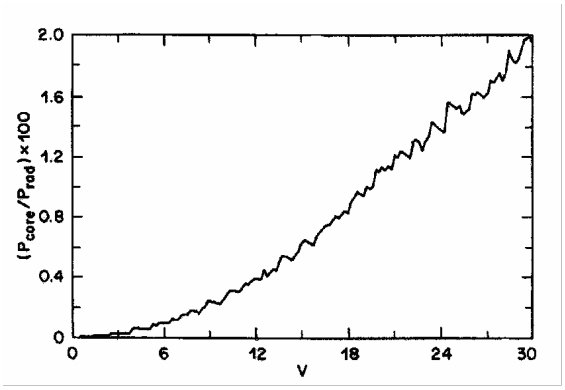

Figure 3.4. Light collection efficiency (γ) of a positively guiding fibre as a function of V number. The light sources are concentrated in a thin layer at the core-cladding interface (reproduced from (Marcuse 1988)).

3.3 Evaluation the performance of the distributed chemical sensing system

The received signal is expected to be very weak, so a sensitive detector such as a photomultiplier tube (PMT) in single-photon counting mode is used for detection. It is important that the detector have sufficient response speed to attain good range resolution. Photomultipliers also permit increasing the signal-to-noise ratio by signal averaging. The returned signal received by the photomultiplier and processed by a pulse amplifier is sampled or gate-ranged at time $2Rn/c$ in a time interval τ_g which corresponds to the effective range resolution.

The number of photoelectrons converted from the returned signal generated by a single laser pulse, and detected in the time interval τ_g, is given by (Hinkley 1976)

$$n(\nu_f) = \frac{P_r(\nu_f, R)\tau_g \eta_f}{h\nu_f}, \tag{3.12}$$

where η_f is the quantum efficiency of the photodetector at frequency ν_f and $h \cdot \nu_f$ is the photon energy at ν_f.

The total measurement time over a particular range-gated interval is $\tau_{meas} = f_p t_{meas} \tau_g$, where f_p is the laser pulse repetition frequency and t_{meas} is the total observation time. In order to obtain the signal-to-noise ratio for this photon counting

scheme, we observe that the total number of photon counts recorded in a given range element will be

$$N_T = f_p t_{meas}\left(n(\nu_f)\xi_S + n_b\xi_S + n_d\xi_N\right) \tag{3.13}$$

where n_b and n_d are the number of noise photoelectrons due to background and dark current, while ξ_S and ξ_N denote the counting efficiency for photoelectron and dark current pulses, respectively. The counting efficiencies usually have a value around 0.8-0.9, determined by the pulse height distribution of the particular photomultiplier and the discriminator level of the receiving system. We make the approximation $\xi_S \approx \xi_N \approx 1$.

In the case of synchronous pulse-gated photon counting, the signal component is derived by subtraction of the total noise contribution ($N_N = f_p t_{meas}\left(n_b + n_d\right)$) from the total count rate, both of which are detected alternately in the same time duration. Therefore we see that the signal-to-noise ratio is

$$\left(S/N\right) = \frac{N_T - N_N}{\sqrt{N_T + N_N}} = \frac{n(\nu_f)\left(f_p t_{meas}\right)^{1/2}}{\left[n(\nu_f) + 2\left(n_b + n_d\right)\right]^{1/2}}. \tag{3.14}$$

The number of measurement cycles (N $= f_p \cdot t_{meas}$) is used as a convenient quantity to characterize the efficiency of detection. This parameter expresses the ability of the detection system to provide sufficient response in a reasonable period of time (accumulation time), where sufficient response is understood in terms of achieving a signal to noise ratio (SNR) = 3, which is sufficient to allow reliable detection of the presence of the chemical species.

$$\mathrm{N} = f_p t_{meas} = \frac{\left(S/N\right)^2\left[n(\nu_f) + 2\left(n_b + n_d\right)\right]}{n(\nu_f)^2} \tag{3.15}$$

A smaller number of measurement cycles (N) requires higher efficiency of the detection system. More measurement cycles are required to detect low concentrations. Increasing the parameter N is possible by increasing either t_{meas} (the total observation time) or f_p (the laser pulse repetition frequency), but there are some practical and fundamental limitations to doing so. Firstly, for practical purposes, the measuring time should generally be less than 30 minutes (although this might vary considerably

depending on the application). Secondly, increasing the laser pulse repetition frequency is limited by the need to avoid pulse overlapping over the desired **detection range**.

Simple calculations show that the upper limit of range for measurements along a fibre is 5.2 km for a pulse repetition rate of 20 kHz, 2.1 km for 50 kHz, 1.0 km for 100 kHz. Therefore, the maximum number of N should not exceed ~10^5 for a laser pulse repetition frequency of 20 kHz and a total observation time of 10 s; or ~10^8 for f_p = 100 kHz and t_{meas} = 30 min, for example.

The total effective length of range resolution (generally referred to as **spatial resolution**) – ΔR – in principle is determined by a combination of the laser pulse length (τ_p), the response time of the optical interaction with the fluorescent species (τ_s), the time resolution of the detection system (τ_c), and the gate time interval (τ_g):

$$\Delta R = \frac{c(\tau_p + \tau_s + \tau_c + \tau_g)}{2n}. \tag{3.16}$$

In an ideal case, when the interaction with the fluorescent species takes place instantaneously, highly precise range finding that corresponds to a high spatial resolution can be achieved by shortening the pulse length and decreasing the resolution time of the detection system together with the gate time interval. This requires more sophisticated and expensive electronics to be employed in the development of the distributed detection system. With a time resolution in the range of nanoseconds, as used in the experimental part of this thesis (Chapters 6 and 7), a minimum spatial resolution of ~ 60 cm is easily achievable.

In fluorescence based detection, the minimum spatial resolution is generally dictated by the fluorescence decay times of the indicators chosen for the sensing application. A moderate example of fluorescence decay times from 20 to 40 ns results in a spatial resolution range of ~ 2 to 4 meters, which may be excessive for practical applications such as corrosion monitoring.

3.4 Modelling results

Results for different fluorophore concentrations are shown in Figure 3.5 for a multi-mode fibre with V = 80. This shows that inspection over large distances is limited

mainly by the absorption of light by the fluorescent material in the activated cladding, despite the higher re-emitted signal power obtained at high fluorophore concentrations. Thus, detection efficiency rapidly becomes worse with distance for high concentrations. Figure 3.6 shows the measurement range that can be achieved within a 30-minute accumulation time as a function of concentration.

For low concentrations, Figure 3.7 shows that detection is possible up to a range limit set by overlapping laser pulses at high repetition rates. This suggests that this kind of system may be suitable for early warning applications.

Calculations for different fibre characteristics (single mode and multimode) show that the detection efficiency strongly depends on the characteristics of the optical fibre (see Figure 3.8). Therefore, it is important to control the level of interaction via the evanescent field to provide reasonable performance over long detection ranges.

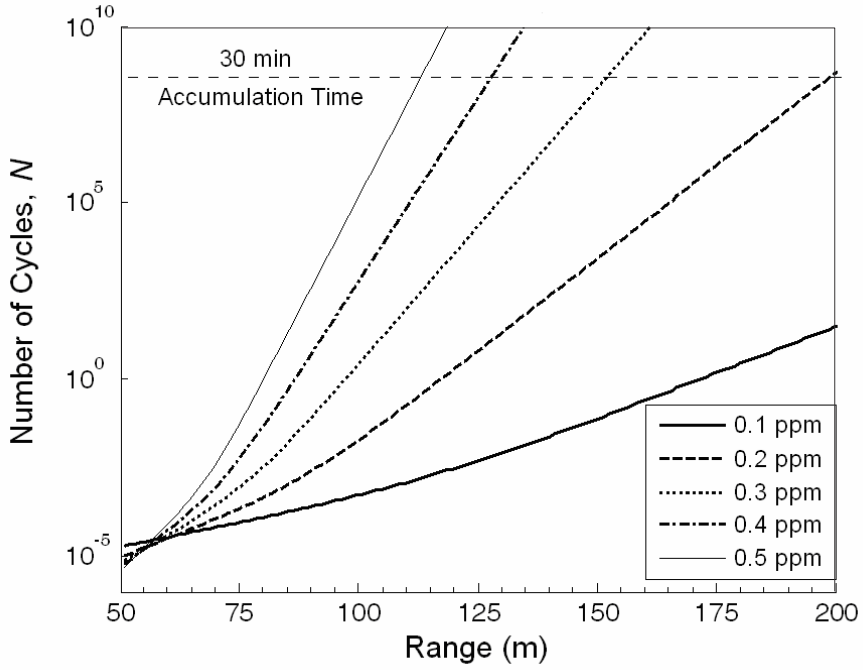

Figure 3.5. Detection efficiency for different fluorophore concentrations (SNR = 3, R_0 = 50 m).

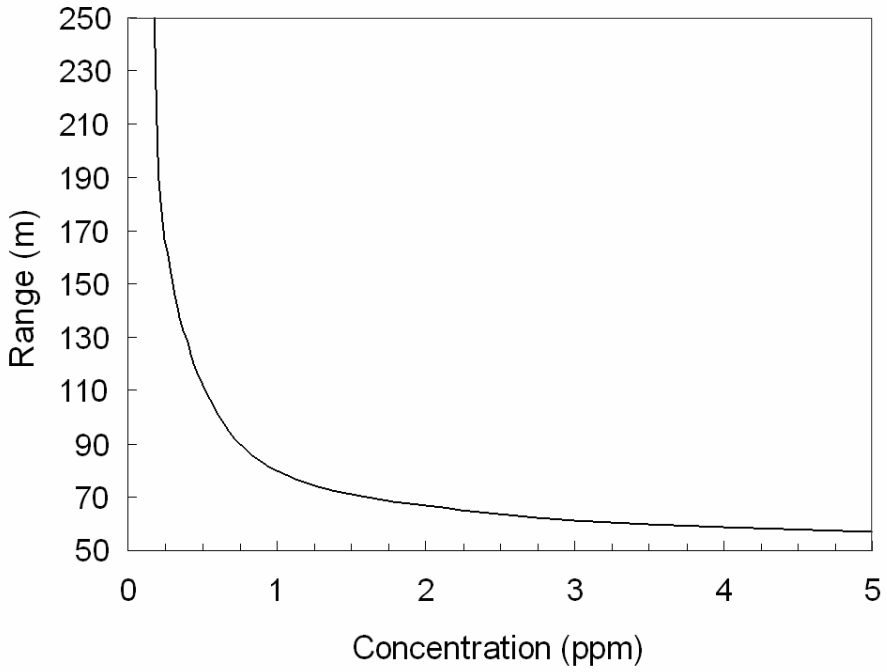

Figure 3.6. Maximum range as a function of concentration for a 30 min. accumulation time.

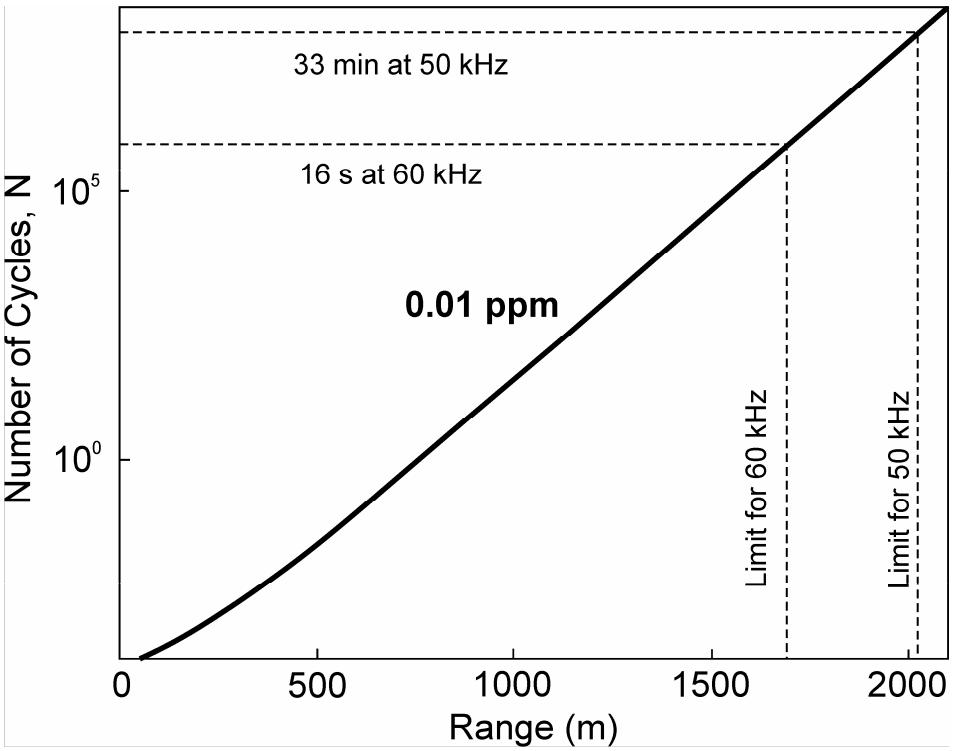

Figure 3.7. Detection efficiency for a fluorophore concentration of 0.01 ppm uniformly distributed in the cladding of a fibre with $V = 80$: a SNR greater than 3 is achieved for measurement conditions above the curve. The horizontal lines reinterpret the number of measurement cycles in terms of signal accumulation time at a given pulse repetition rate. The vertical lines show how the time-of-flight limits the range for a given pulse repetition rate. Depending on the time available for signal accumulation, the model

therefore suggests a practical upper limit to the range of approximately 1800 m in this case.

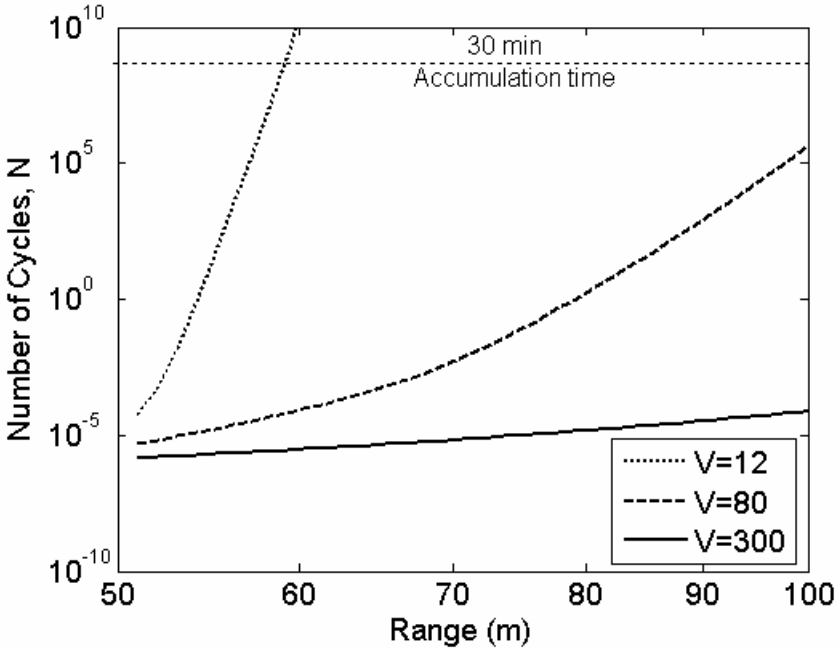

Figure 3.8. Detection efficiency for a range of normalized frequencies V, where smaller V-numbers correspond to higher P_{clad}/P.

These modelling results for the distributed corrosion sensor, based on a conventional multi-mode fibre with a modified cladding and sensitive fluorescence detection by photon counting, suggest that under ideal conditions, sub part per million sensitivity can be achieved over distances of more than a kilometre, which is sufficient for practical application in corrosion monitoring.

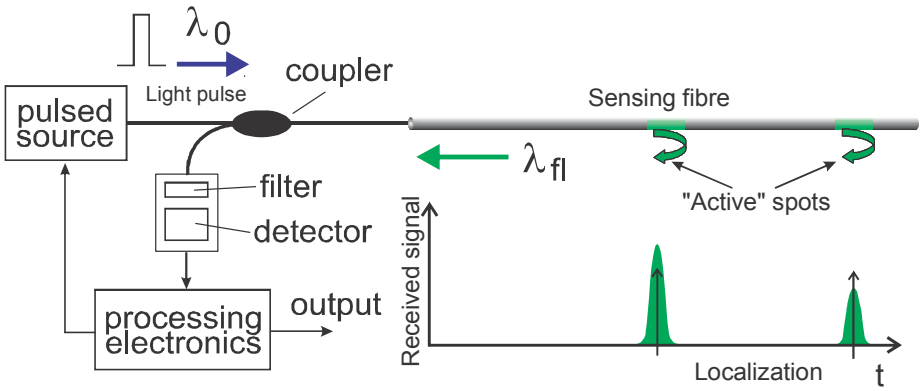

Figure 3.9. Schematic illustration of a system to detect a non-uniform distribution of a fluorophore in the cladding of a fibre.

The modelling considers an extreme case when the modified cladding region contains a uniformly distributed fluorescent dye which interacts with the propagating

light along the entire length of the fibre. This case is characterized by maximum absorption of the energy of the launched light pulse and, consequently, minimum detection range can be achieved. In a more practical case when there is one or just a few "active" spots that must be located along the sensitive fibre (as shown in Figure 3.9) , the detection range and detection efficiency are expected to be further improved.

3.5 Summary

In this Chapter a theoretical model of the response of the ideal distributed sensing system was described. Calculations based on the theoretical model were used to evaluate the performance of an ideal distributed sensing system. Critical parameters such as detection efficiency, detection range, and spatial resolution were also discussed.

It was found that under ideal conditions, sub part per million sensitivity can be achieved. At the same time it was shown that the detection efficiency strongly depends on the characteristics of the optical fibre. In this connection, additional theoretical and experimental investigations were suggested to study the effect of the optical fibre sensor characteristics on the detection efficiency. Different constructions of optical fibre sensor will be discussed in Chapters 4 and 5.

The detection range for the ideal distributed sensing system is limited by overlapping laser pulses at high repetition rates. The estimated range is found to be suitable for the purposes of corrosion sensing applications.

As discussed in Section 3.3, the minimum spatial resolution of detection in a realistic situation where the fluorescence decay time can not be neglected, is limited by the lifetime of the fluorophore (indicator). Thus, extra theoretical and experimental investigations of the effect the fluorescence decay time on the spatial resolution were necessary. These investigations are presented in Chapter 6. The method to improve the spatial resolution for a long lived fluorescent indicator was developed and experimentally tested. This is also presented in Chapter 6.

Chapter 4

Evaluation of Techniques

4.1 Water ingress detection from spectral measurements

As described in Chapter 1, water plays a significant role in creating a corrosive environment. The spectral attenuation due to the presence of water in optical fibre (as described in Chapter 2) provided the basis for the following water ingress experiment.

The materials and equipment used in the experiments were as follows:

- Single mode, pure silica optical fibre: F-SMF-28 from Corning with core diameter 8.2 μm, cladding diameter 125 μm;
- Optical spectrum analyser: ANDO 6315E. Wavelength range 350 - 1750 nm, wavelength resolution 0.05 to 10 nm, measurement level range -90 to +20 dBm;
- White light source: Apex quartz tungsten halogen source, 100W, 33 mm output beam, 0.81° divergence.

F-SMF-28 fibre is optimised for use in the 1310 nm wavelength region and is widely exploited in telephony, cable television, submarine and utility network applications. It has high mechanical strength and low attenuation at the water peak (attenuation at 1383±3 nm does not exceed 2.1 dB/km according the specification). This low level of attenuation provides a low background for water ingress detection.

F-SMF-28 fibre is protected by dual acrylate CPC coating. CPC coatings are designed to be mechanically stripped and have an outside diameter of 245 μm. The optical fibre was mechanically stripped of the protective coating for a length of approximately 10 m. Transmission spectra have been recorded before and after stripping of the protective fibre coating. The change in the power transmitted through the fibre

before and after stripping is shown in Figure 4.1 As it can be seen, the stripping led to a small increase in the propagation losses.

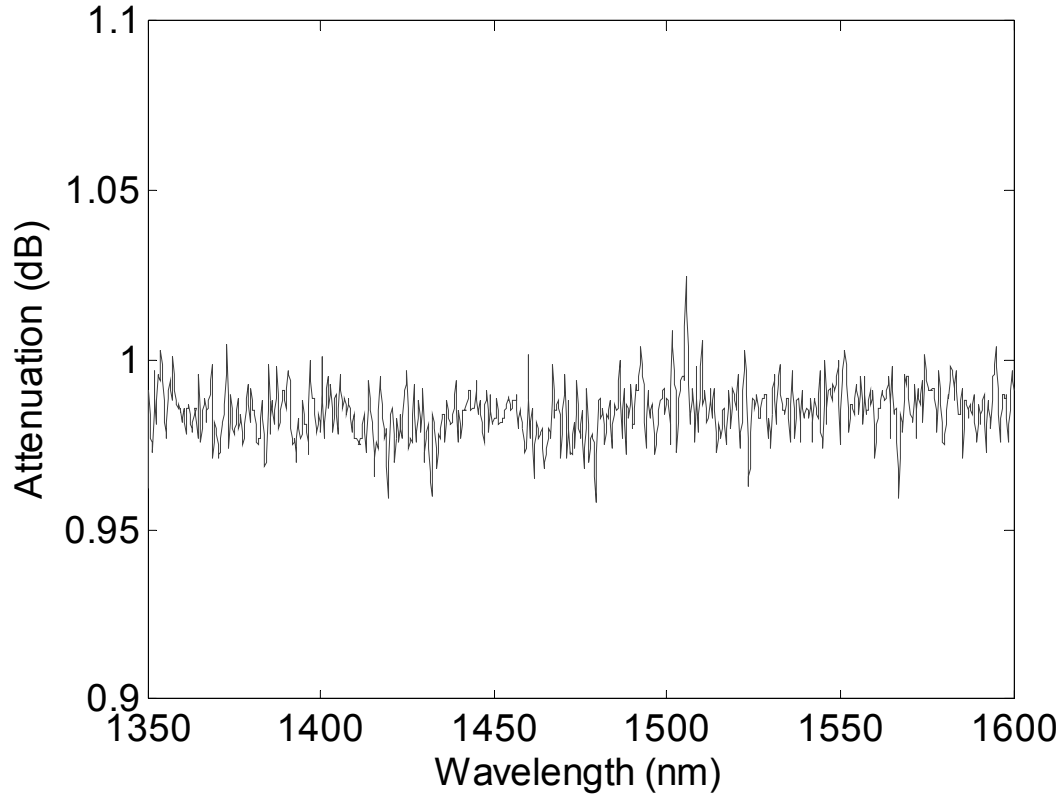

Figure 4.1. Attenuation in the power transmitted through the fibre after stripping of the protective coating. The stripped fibre section was 10 meters long.

The emission from the white light source was coupled into the fibre and the transmitted spectra were recorded with the spectrum analyser for different water immersion times. After two days of the water immersion, the experiment was terminated because the unprotected fibre became brittle and broke down.

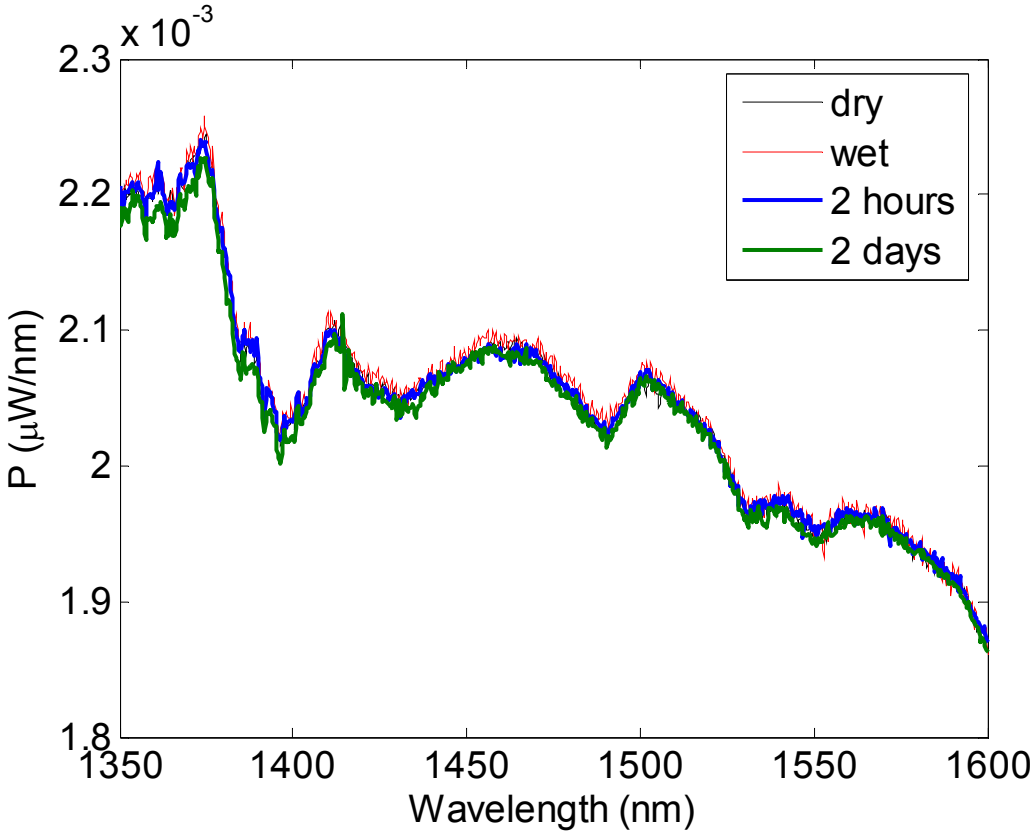

Figure 4.2. Optical fibre transmission spectra during the water immersion experiment. Notation: "dry" – for stripped fibre section in air, "wet"- stripped fibre section just immersed in water, "2 hours" and "2 days" – time of water immersion.

The results of the water immersion experiment are shown in Figure 4.2. After immersion in water for two days no significant change in transmitted power was observed. The recorded transmission spectrums were closely examined to find evidence of water ingression. Received spectra were smoothed using Savitzky-Golay algorithm to eliminate noise and differences between initial spectrum (wet fibre just immersed in water) and spectra after certain times of water immersion were calculated. The differences represent change in the fibre attenuation with water immersion time (shown in Figure 4.3). Only a slight increase (less than 2 % from the initial values) in attenuation in the 1350-1400 nm spectral range using the sensing fibre length of 10 m long was realized.

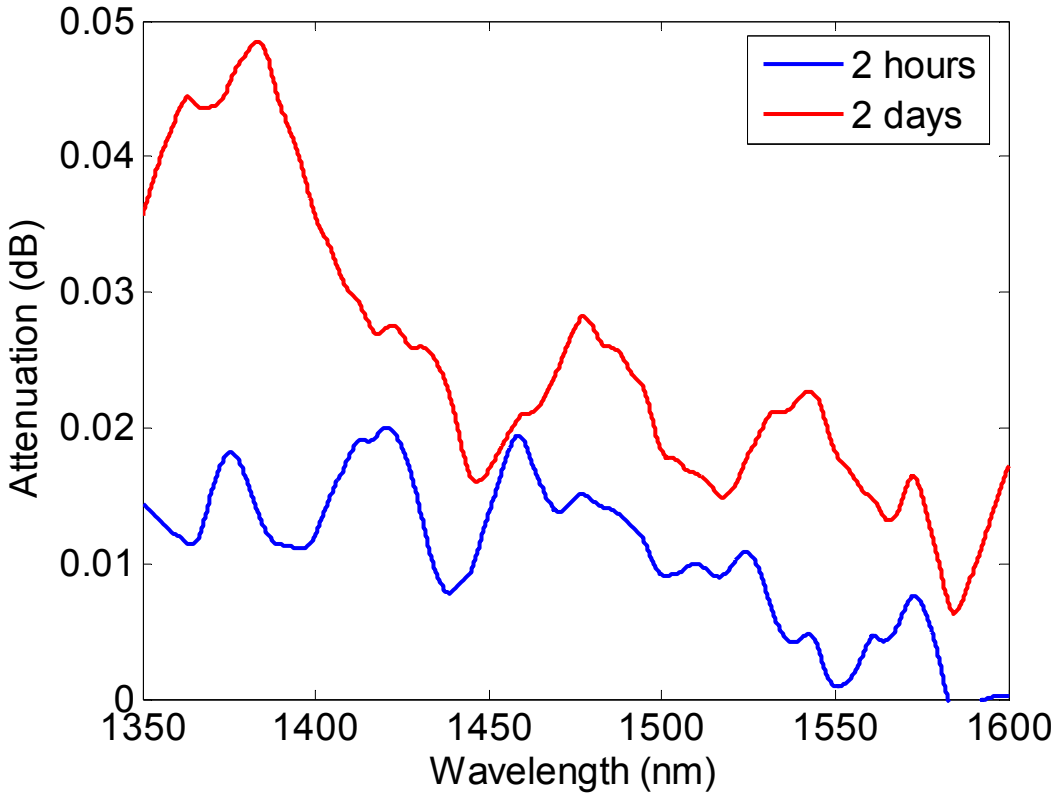

Figure 4.3. Attenuation in optical fibre after immersion in water for different times. The loss is referenced against the transmitted power measured immediately after immersion in water.

The possible explanation might be found in considering the physical dimensions of the fibre. The single mode silica fibre has a core approximately 8 μm in diameter where the light power is confined (see Figure 4.4).

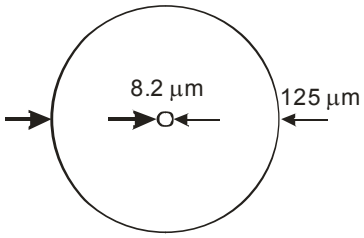

Figure 4.4. Geometry of a single mode optical fibre: core and cladding.

Only when water penetrates all the way through the cladding does it interact with the evanescent field and spectral attenuation occurs. According to published results (Huang et al. 2004), it can take more than 2500 h to observe changes in the absorption spectra in a harsh environment at a temperature of 200°C using the same type of fibre. It

would be expected that at room temperature such penetration through the cladding would take a much longer time. Similar results are presented in (Berger and Tomozawa 2003) where changes in absorbance at the water peak wavelength were monitored to characterise water diffusion into silica glass optical fibre. Similar to the presented results, the water peak was not observed after fibre stripping. Changes in absorbance of values less than 0.1 were recorded after 24 hours of exposing the fibre to water vapour at temperatures of 600 ºC to 800 ºC.

Longer immersion times are possible, but would require fibre protection from breakage. This may be achieved by leaving the polymer cladding in place, provided that the cladding does not significantly modify the rate of water diffusion. However, the results presented here assume employing a long fibre sensor, which contradicts the distributed sensing concept. The sensor response would be unpredictable, with variations probably dependant on micro fissures in the cladding. For these reasons, the use of a conventional stripped fibre for water ingress detection is not an immediately attractive method.

4.2 Sensor construction using D-fibre

The possibility of constructing an optical fibre sensor based on commercially available D-fibre was investigated. As described in Section 2.2, light propagating in the optical fibre penetrates into the cladding area. The depth of penetration depends on the propagating wavelength and the optical fibre characteristics, but generally it is comparable to the wavelength. The D-fibre was purchased from the KVH Company and had the followed specification: E-core polarization maintaining fibre, D-series, nominal operating wavelength 820 nm, largest fibre width 80 μm (indicated in the specification as a diameter) and centre of core to flat 10 μm (see Figure 4.5). The diameter of the coating was 230 μm. Taking into account that sensing is expected to be performed in the visible and near infrared spectral region, modification of the D-fibre was necessary to reduce the centre-of-core to flat distance to less than 1 μm. Etching with hydrofluoric acid was employed to gradually reduce the cladding thickness.

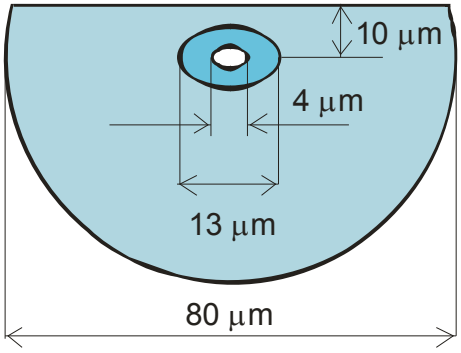

Figure 4.5. D-fibre geometry.

D-shape fibre was cut into 5 cm pieces; every piece was chemically stripped with methylene chloride and cleaved using a manual fibre cutter. Also singlemode and multimode telecommunication fibres were cut into the same length, stripped mechanically and cleaved with the automatic cleaver. Fibres were mounted on the plastic holders and etched in 40% hydrofluoric acid for different periods of time. Etched fibres were examined with an optical microscope.

Etching with concentrated (40%) HF acid resulted in the fibre geometries shown in Figure 4.6. Etching rates for the cladding region of D-shaped and other types of fibre together with the standard errors estimated from the fitting are shown in Figure 4.7 and Table 4.1. The error analysis and fitting procedure are explained in detail in Appendix 2. Differences in the etch rates are normally caused by differences in the glass dopants and the doping concentration. For D-fibre, the germania-doped core region etches faster than the fluorine-doped cladding, and after less than 6 minutes of etching the acid reaches and quickly destroys the fibre core.

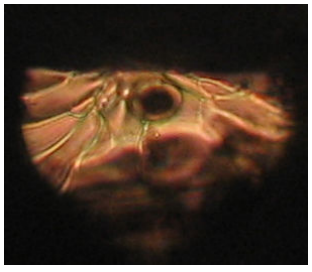		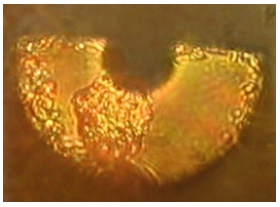
Etching time 3 min, Ø 74 µm	Etching time 6 min, Ø 69 µm	Etching time 9 min, Ø 67 µm

Figure 4.6. Etching results for D-fibre samples with HF concentration 40 %. The etched cladding diameters are shown.

Table 4.1. Etch rates for HF concentration 40 %. The standard errors are also shown.

Fibre type	Etching rate, μm/min
D-fibre (KVH)	0.6±0.1
Telecommunication SM (Corning)	1.3±0.1
Telecommunication MM (Corning)	1.2±0.1

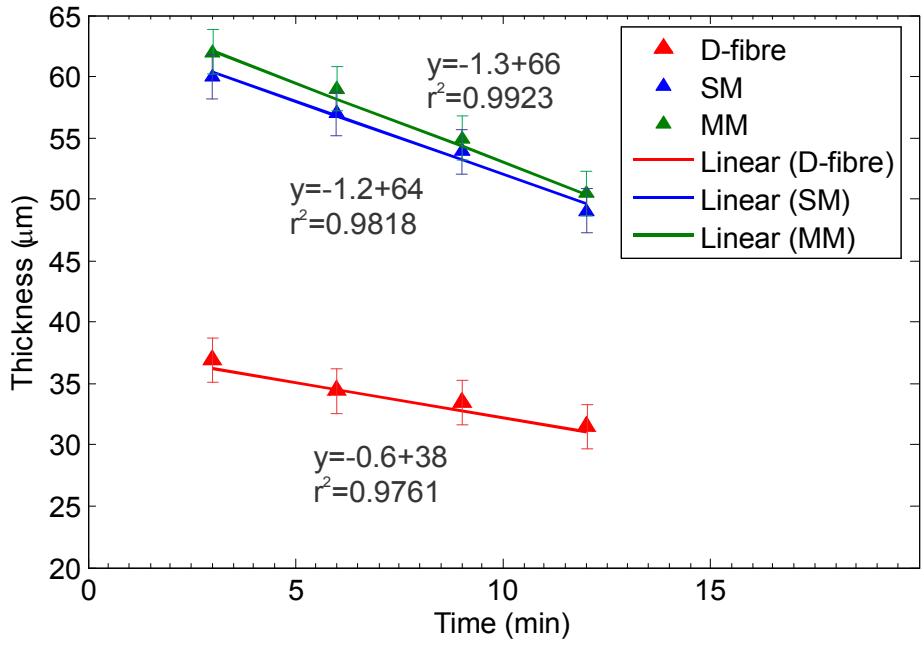

Figure 4.7. Calculated etch rates from the fibre measurements. "Thickness" refers to the etched cladding radius.

In order to control the etching process more precisely, a reduced HF concentration of 20% was employed to etch the D-fibre cladding to a predetermined depth. To produce a sensing fibre suitable for distributed measurements, the middle section of the length of D-shaped fibre was stripped for a length of about 3 cm. After that the D-fibre was spliced to a standard telecommunication singlemode fibre patchcord. The output from a 780 nm laser diode was launched into the singlemode fibre patchcord and the output power was monitored during the etching process with a Newport Optical Power Meter (Model 1830-C) and a Universal Fiber Optic Detector (Model 818-IS-1). The transmitted power was recorded using Labview data acquisition software. Changes in the transmitted power during the D-fibre etching process are presented in Figure 4.8. Figure 4.8 (b) shows a detailed view near the power drop point. The fibre core was destroyed entirely over the period of time marked as 19 s. It caused a significant drop in

the transmitted power. To provide an acceptable level of loss in the sensor within, for example 10 %, and maintain this level for series of sensors, timing precision should be better than 2 seconds. This represents less than 0.1% of the total etch time. Therefore it is considered highly unlikely that the overall etch time could be used to determine the termination point, given the probable variation in etch rate due to small changes in acid concentration. Also it should be kept in mind that the etching process can not be terminated instantly; etching can still continue for some seconds during rinsing, depending on the process conditions. The period of time marked as 15 s could be considered as an ideal time for the etch termination, but there is no clearly detectable drop in power to identify this region.

It was found to be difficult to etch the D-fibre to a predetermined depth due to the rapid drop in transmitted power as the core is approached, together with noisy fluctuations in the transmitted power level.

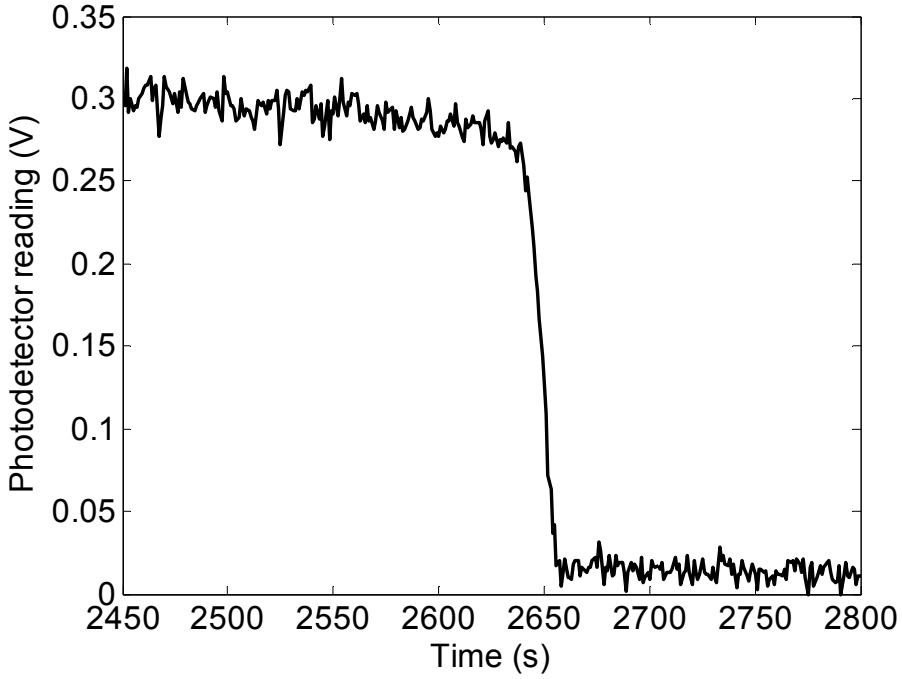

(a)

Figure 4.8. (a) Changes in the transmitted power during the D-fibre etching process.

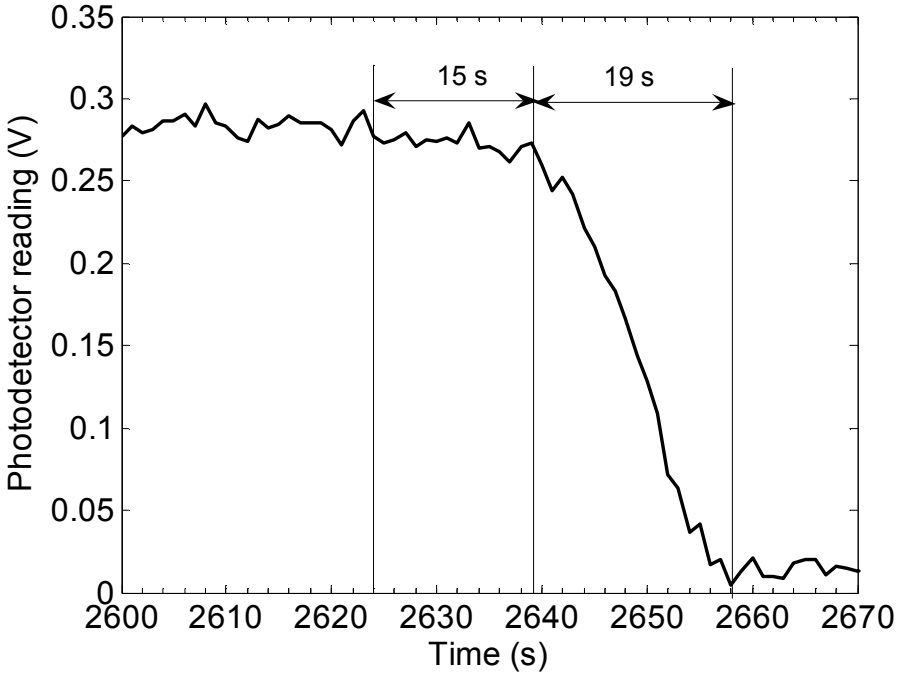

(b)

Figure 4.8. (b) Detailed view near the power drop point. HF concentration 20 %.

The use of D-shaped fibre as a distributed optical fibre sensor appears to be unattractive for the following reasons:

1. It is difficult to effectively couple the output of laser diode sources into this type of fibre geometry.

2. There are obvious difficulties in using HF etching on a large scale. These challenges are exacerbated by the fact that the etching process is difficult to control.

3. There are difficulties with connecting (splicing) D-fibre to conventional fibres or even other D-fibres.

4.3 Large core fibre as a sensing element

Despite the fact that significantly multimode large core fibres have a low evanescent field fraction, they provide high power throughput and are relatively easy to handle. Large core fibres with plastic cladding are readily available and allow the possibility of constructing an evanescent field sensor using a relatively simple stripping and decladding technique.

4.3.1 Decladding technique

Fibres with plastic cladding and pure silica core diameters of 200 μm and 600 μm (APC200/300N Low OH and APC600/700N Low OH - Anhydroguide PCS VIS-IR fibre from Fiberguide Industries) were used in the experiment. The fibre geometry is shown in Figure 4.9. These fibres have a theoretical numerical aperture of 0.37 (up to 2 meters length) and “steady state” numerical aperture of 0.23 (over a 50 meters length). The theoretical numerical aperture, as calculated from the refractive indices of the core and cladding materials, only persists for short fibre lengths as guided rays near to the maximum acceptance angle are selectively attenuated by the cladding material so that a somewhat reduced effective or "steady state" numerical aperture governs transmission for distances over 50 meters.

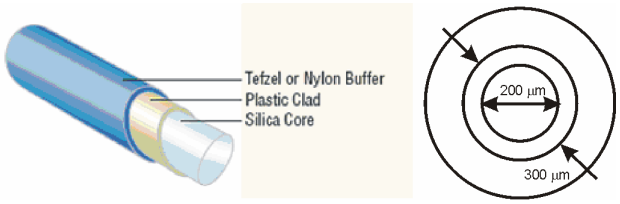

Figure 4.9. Large core fibre geometry.

The standard nylon buffer coating was removed with a surgical blade over the proposed sensing section. A sensor section was prepared by removing the plastic cladding using two different techniques: either chemically using a sulfochromic acid mixture or burning with a gas torch. The declad fibre was tested as a sensor by coupling a 780 nm laser diode into a 100 m length of optical fibre with the 20 cm declad section close to the far end. The declad sensor section was immersed in various liquids as required. The transmitted energy was measured at the far end using a Newport Optical Power Meter (Model 1830-C) with a Universal Fiber Optic Detector (Model 818-IS-1). This configuration allows the equilibrium mode distribution to be attained at the sensing region and avoids instability caused by leaky modes.

The sensor section was immersed in dimethyl sulfoxide (DMSO)/water mixtures to expose the declad core to environments with a range of refractive indices. The different methods of decladding result in significant differences in sensor performance. Burning with a torch causes noticeable damage of the core surface (see Figure 4.10) and leads to additional scattering at the core-cladding interface. The results for the transmitted power in the 200 μm diameter fibre are shown in Figure 4.11. The chemical

decladding technique was found to be much less disruptive of the core-cladding interface, delivering relatively constant transmission over the range shown.

Figure 4.10. SEM image of burned cladding fibre.

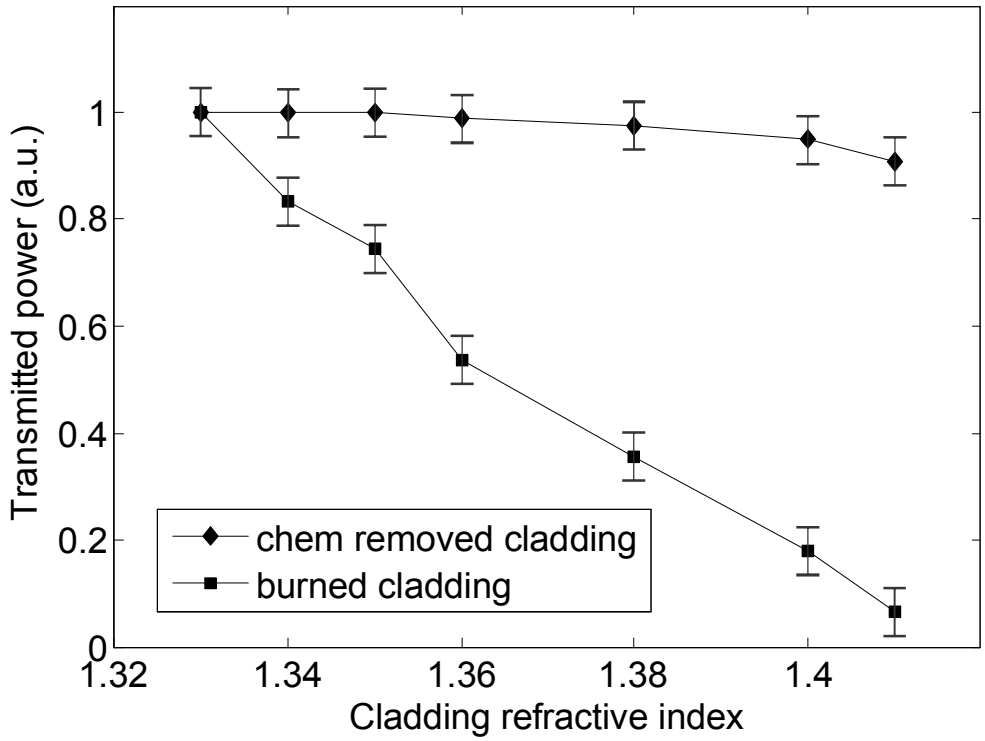

Figure 4.11. Dependence of fibre transmission on the environmental refractive index for the fibre with core diameter 200 μm declad by different methods. Wavelength was 780 nm. The curves are included as a guide for the eye.

Additional measurements of the environmental refractive-index dependence were performed with the 600 μm chemically declad fibre with 406 nm excitation. The results are shown in Figure 4.12 and are similar to those obtained for the 200 μm fibre. Therefore, the chemically declad sensor was used for further experiments with the refractive index of the test solution adjusted to a value less than 1.45 (the pure silica core refractive index) to meet guiding requirements and avoid losses.

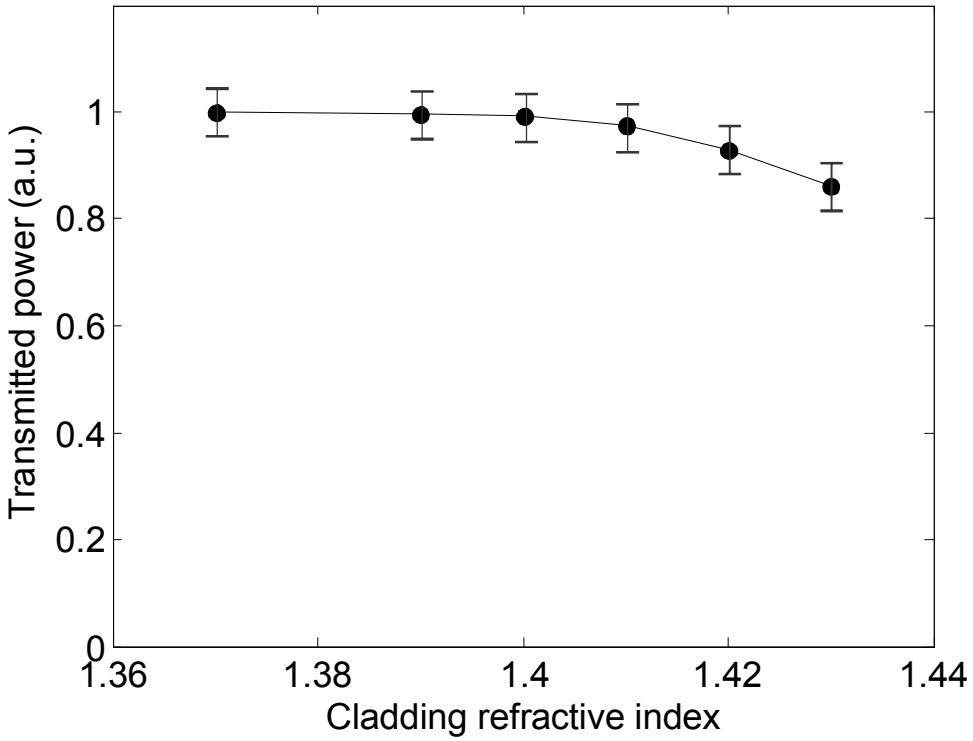

Figure 4.12. Dependence of fibre transmission on the refractive index of the environment for the fibre with core diameter 600 μm after chemical stripping. Wavelength was 405 nm. The curve is included as a guide for the eye.

4.3.2 IR spectral region. CW absorption and fluorescence

In order to evaluate the efficiency with which fluorescence is excited in the cladding region and coupled back into guided modes of the fibre, an experimental investigation was performed under conditions comparable to those modelled earlier (Chapter 3). However, it should be noted that the model of Chapter 3 exploits a sensor in which fluorescence is excited through the whole length of the fibre. It is not possible to exactly represent this situation in the present experiment where all measurements are conducted over a short length of declad fibre.

An organic laser dye (IR-125 from Exciton) with maximum absorption close to 780 nm and fluorescence band with maximum at 850 nm was used as a model system to be excited via the evanescent field in the optical fibre sensor. The optical properties of IR-125 are shown in Figure 4.13 where excitation, absorption and fluorescence bands all correspond to the modelling parameters used in Chapter 3.

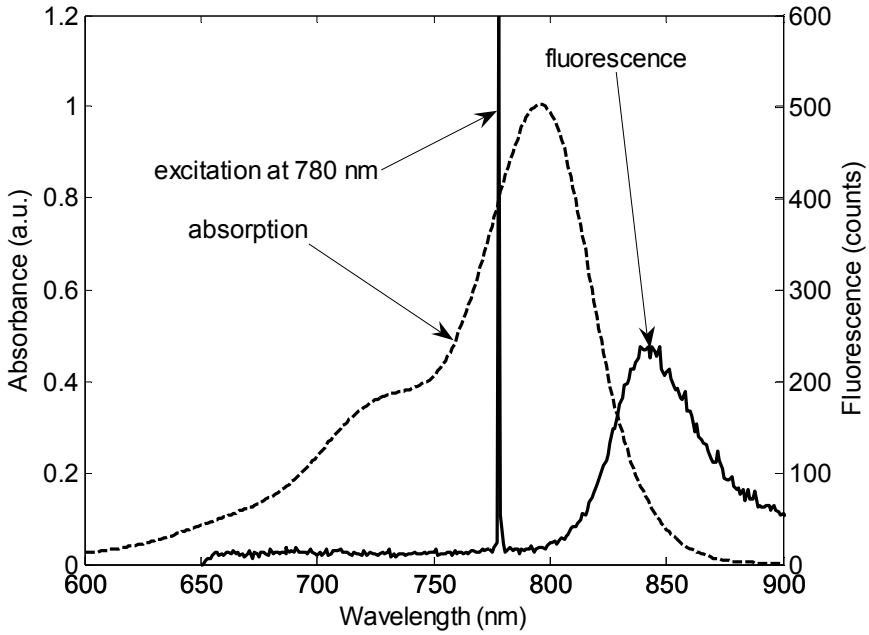

Figure 4.13. Spectral and fluorescent properties of IR-125 for excitation with a laser diode at 780 nm.

Measurements of absorption at 780 nm due to the presence of IR-125 in the solution surrounding the declad section of 200 μm fibre were performed at the far end of the fibre using a Newport Optical Power Meter (Model 1830-C) with a Universal Fibre Optic Detector (Model 818-IS-1). Spectral fluorescence measurements were also performed with an optical spectrum analyzer (ANDO AQ-6315E) using an ultrasteep longpass filter (Omega Optics 850 LP) to avoid detector overload by the excitation wavelength. A photomultiplier tube (Hamamatsu R928) was used to detect low level changes in fluorescence output as a function of fluorescent dye concentration. The experimental setup is shown in Figure 4.14.

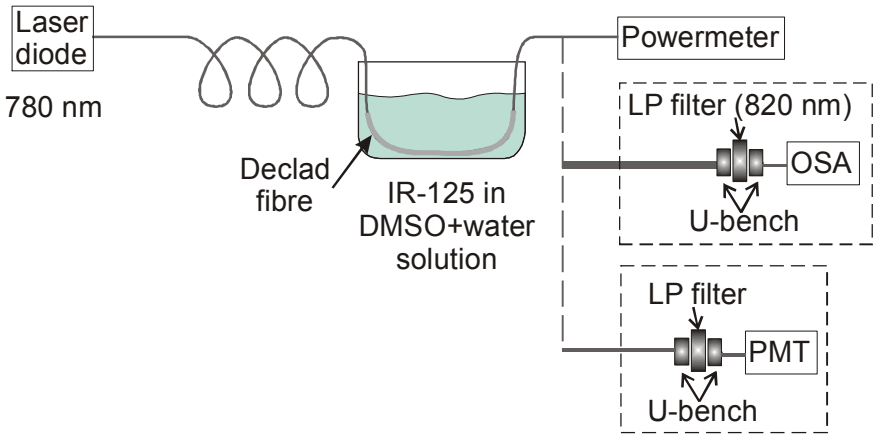

Figure 4.14. Experimental setup for spectral absorption and fluorescence measurements in the near IR region.

In-fibre measurements of the IR-125 fluorescence spectrum performed using the experimental setup with the optical spectra analyser are presented in Figure 4.15. The background and background-subtracted fluorescence signals for CW excitation are also shown. The IR-125 concentration was 10^{-4} mol/l in a 50/50 mixture of DMSO and water, with a refractive index of 1.37. The results show that detectable levels of fluorescence are coupled into forward propagating modes of the optical fibre. At the same time, a significant level of background is observed which can limit the sensitivity of the fibre sensor. This background is most probably due to residual spontaneous emission from the laser diode (Stoddart et al. 2005).

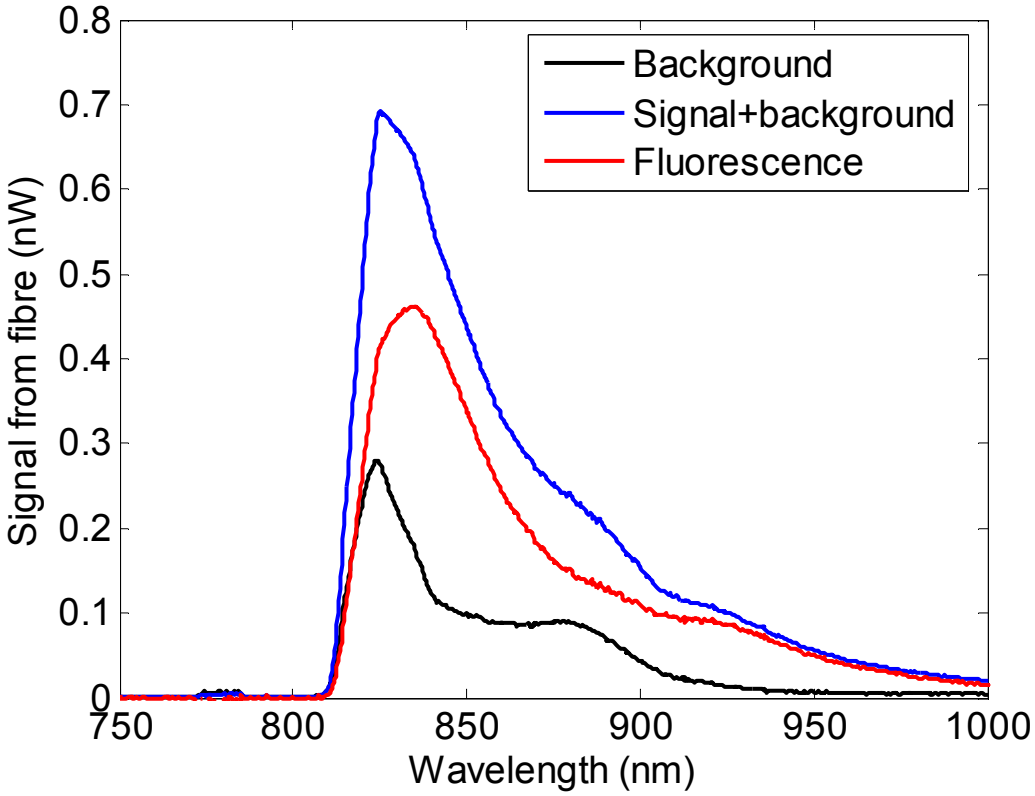

Figure 4.15. Change in the fluorescence spectrum collected by the sensing fibre in the presence of the laser dye (IR-125). "Background" – signal recorded in pure solvent (50/50 mixture DMSO and water); "Signal+Background" – recorded signal in a solution of 10^{-4} mol/l IR-125; "Fluorescence" – fluorescence signal after background subtraction.

The experimental dependence and fitted model curves of the sensor response to changes in fluorescent dye concentration are presented in Figure 4.16 and Figure 4.17. The change in transmission measured at 780 nm using the experimental setup with the powermeter caused by absorption in the IR-125 dye is shown in Figure 4.16. The fitting

equation for the transmitted power as a function of absorbing dye concentration can be written as

$$P = P_0\kappa + P_0 e^{(-r\varepsilon l N_{conc})}, \tag{4.1}$$

where P_0 is the power at the beginning of the sensing section, l is the sensing length, N_{conc} is the fluorescent dye concentration, ε is the absorption coefficient of the fluorescent material, r is a coefficient characterizing the level of interaction via the evanescent field and depends on waveguide properties of the optical fibre sensor. Consequently the product $r\varepsilon N_{conc}$ has the meaning of the power attenuation coefficient for cladding absorption. This fitting equation is similar to Beer's Law, but has an additional component $P_0\kappa$. The large core fibre is a significantly multimode structure (the number of modes at 780 nm ~ 10^4) and because different modes experience different levels of interaction with the absorbing materials surrounding the core area, some modes propagate through the fibre sensor with negligible attenuation, which is represented by the term $P_0\kappa$.

The parameters in the fitting equation (4.1) have the same physical meaning as those in the model of Chapter 3, but the fact that the experiment was designed for integrated (CW) rather than distributed measurements should be taken into account. The integrated measurement was performed under CW excitation using equipment that does not provide time resolution. Practically such equipment 'integrates' all measurements over a measurement period of time. In contrast, distributed measurements performed on equipment which provides time resolution, allow changes of the measurand to be observed over time. This time dependence can be converted to distance by a distributed system like OTDR. CW measurements were used to characterize the sensor performance from the point of view of spectral measurement or transmission loss measurement, for example. While this characterization cannot be directly converted to a distributed measurement, it gives valuable information about physical and chemical processes occurring in the optical fibre sensor.

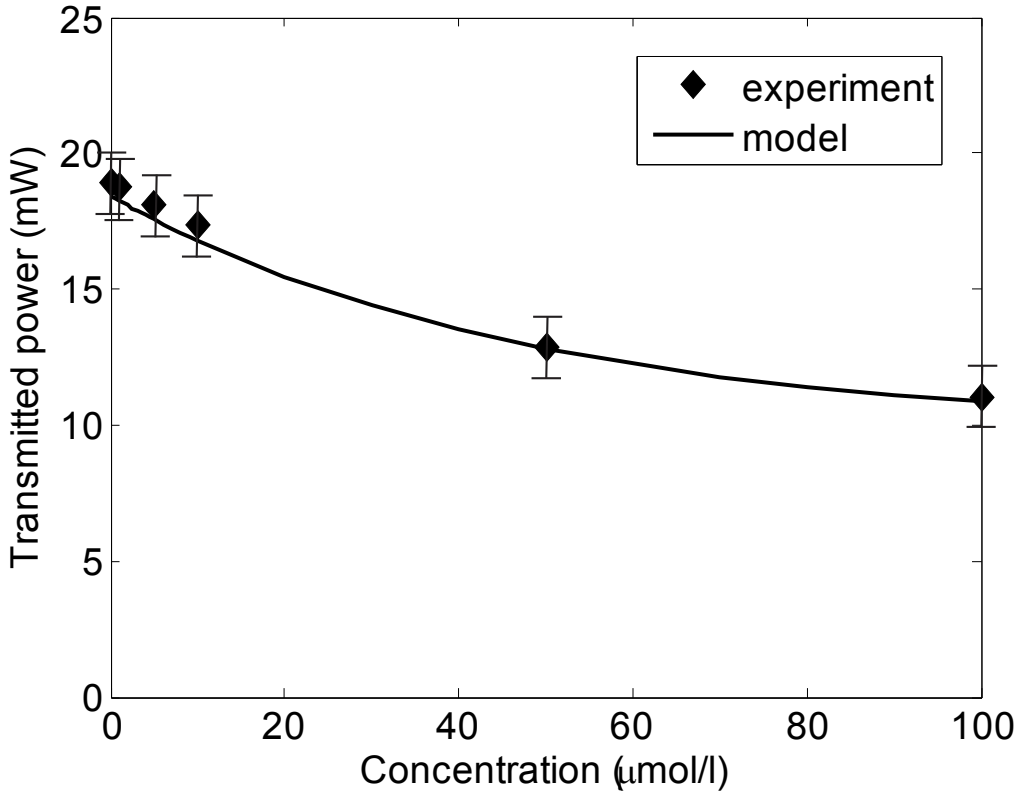

Figure 4.16. Transmission through the optical fibre sensor as a function of changes in IR-125 concentration. The fibre interaction length was 20 cm.

The points and curve in Figure 4.17 represent experimental and fitting results for the fluorescence signal as a function of fluorescent dye concentration. The experimental points were recorded using the experimental setup equipped with LP filter and photomultiplier tube. Curve fitting is based on the equation:

$$P = P' + \beta P_0 \left(1 - e^{(-r\varepsilon l N_{conc})}\right), \tag{4.2}$$

where β represents the evanescent field coupling efficiency and P' is the background signal in the absence of the fluorescent dye. The fitted parameter for the power attenuation coefficient for cladding absorption ($r\varepsilon N_{conc}$) is given in Table 4.2 for absorption and fluorescence experiments. Taking into account that the experiments were performed independently with slightly different propagation conditions for the excitation and fluorescence emission, the numbers in Table 4.2 are in reasonable agreement. A comparison of the fitting equations shows that the total forward propagating fluorescence signal is proportional to the power absorbed by the dye.

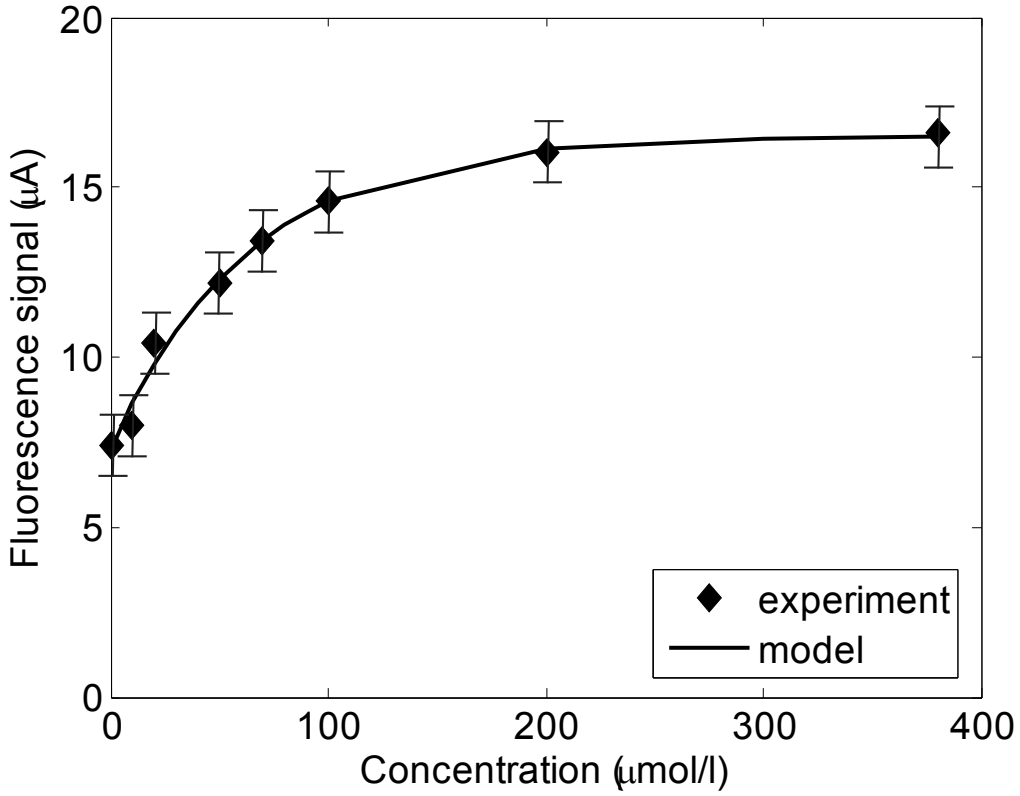

Figure 4.17. The intensity of the fluorescence signal collected by the optical fibre sensor as a function of changes in IR-125 concentration.

Table 4.2. Fitting parameter - power attenuation coefficient for cladding absorption ($r\varepsilon N_{conc}$).

Fitting for:	Power attenuation coefficient
The absorption experiment	$(4.7 \pm 0.4) \times 10^{-5}$
The fluorescence experiment	$(6.4 \pm 0.7) \times 10^{-5}$

4.3.4 Blue spectral region. CW absorption and fluorescence

An experiment was performed to evaluate the optical fibre sensor based on large core fibre in the blue spectral region. As described in Chapter 1, aluminium ions can be detected using the 8-HQ indicator. When mixed with the aluminium ions, 8-HQ produces a complex Alq_3, which emits fluorescence in the optical range of 490-550 nm with blue light excitation at 405 nm. The basis of using this reaction is well documented and proven to be used for aluminium detection (McAdam et al. 2005). Despite the optical fibres having their best performance in the near-IR spectral region, it is still possible to make effective use of them in the blue spectral region.

A 0.2 m long sensing section of plastic clad large core fibre (two samples with 200 μm and 600 μm core diameters) was prepared by mechanical stripping with a surgical blade and chemical decladding, as described earlier. The sensor section was immersed in a bath of Alq_3 solution in ethanol in a similar setup to that used previously for the IR experiment (see Figure 4.14). A 405 nm laser diode was used in CW mode to excite the system. The forward coupled fluorescence was registered with the ANDO AQ-6315E optical spectrum analyser through a longpass optical filter.

The first set of recorded spectra was obtained with a long pass filter with cut-on wavelength at 420 nm. A typical spectrum is shown in Figure 4.18. The spectrum shows the expected fluorescence in the wavelength range from 490-550 nm (see (a) in Figure 4.19, which shows a detailed view near the fluorescence wavelength range, as well as (b) the fluorescence spectrum with the background subtracted). However, the excitation wavelength of 405 nm is ineffectively blocked to permit clear fluorescence measurements. In addition, there is a spectral component at 410-500 nm that contributes to the background and may originate from the laser diode or from the optical fibre itself.

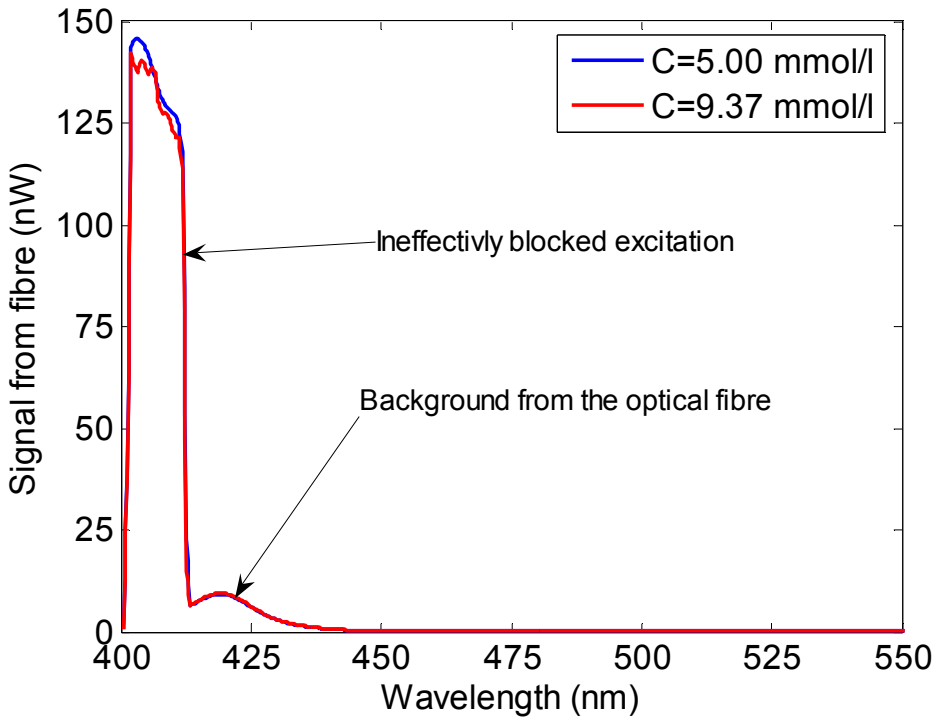

(a)

Figure 4.18. Forward coupled measurements of in-fibre Alq_3 fluorescence with 405 nm excitation. A typical spectrum.

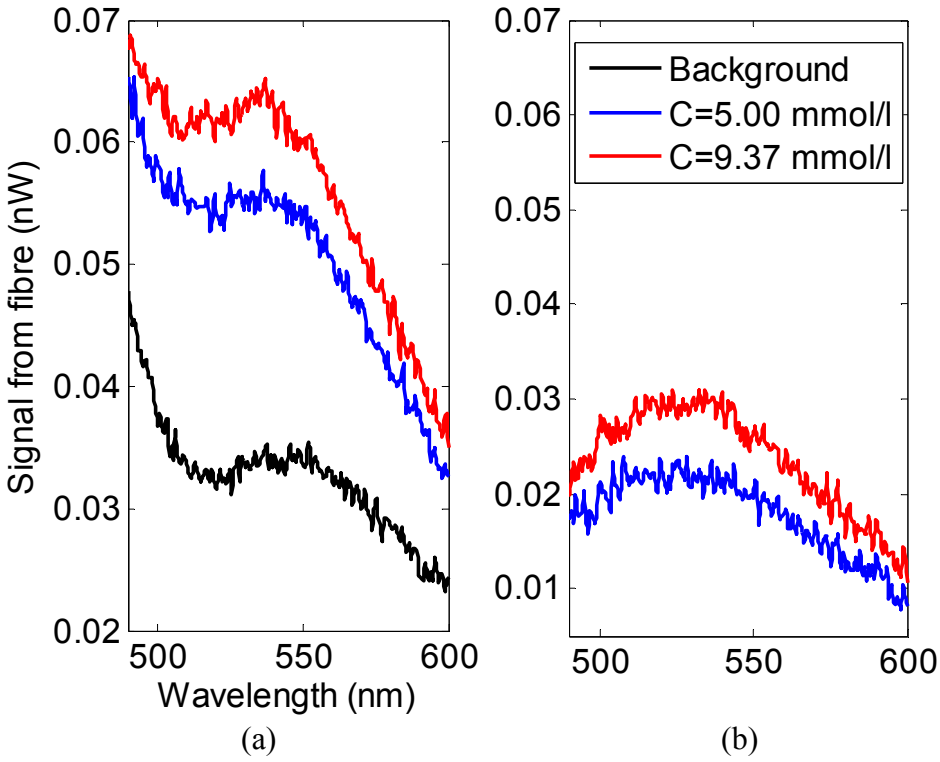

Figure 4.19. Forward coupled measurements of in-fibre Alq_3 fluorescence with 405 nm excitation. (a) A detailed view near the fluorescence wavelength range and (b) the fluorescence spectrum with the background subtracted.

An ultrasteep longpass filter from Iridian with the cut-on frequency 448 nm (ZX-000448) was used in the subsequent experiments to provide efficient suppression of the excitation and background emission. This was necessary because the relatively strong elastic (Rayleigh) scattering which happens at the excitation wavelength is detected in both back-reflected and forward measurements when sensitive detection methods like photon counting are used.

A fluorescence spectrum recorded in CW mode with the Iridian filter is shown in Figure 4.20. The Iridian filter provides excellent filtering of the exciting wavelength, while the fluorescent signal can be detected. However, the background signal is still high compared to the fluorescence signal, which potentially can limit detection sensitivity. This background signal originates from the long length of the fibre before the sensor section. Operating in the distributed (gated) mode could help to overcome this problem, because in CW mode the background signal is integrated along the fibre, whereas the fluorescence signal is only collected from the 0.2 m sensing part of the fibre.

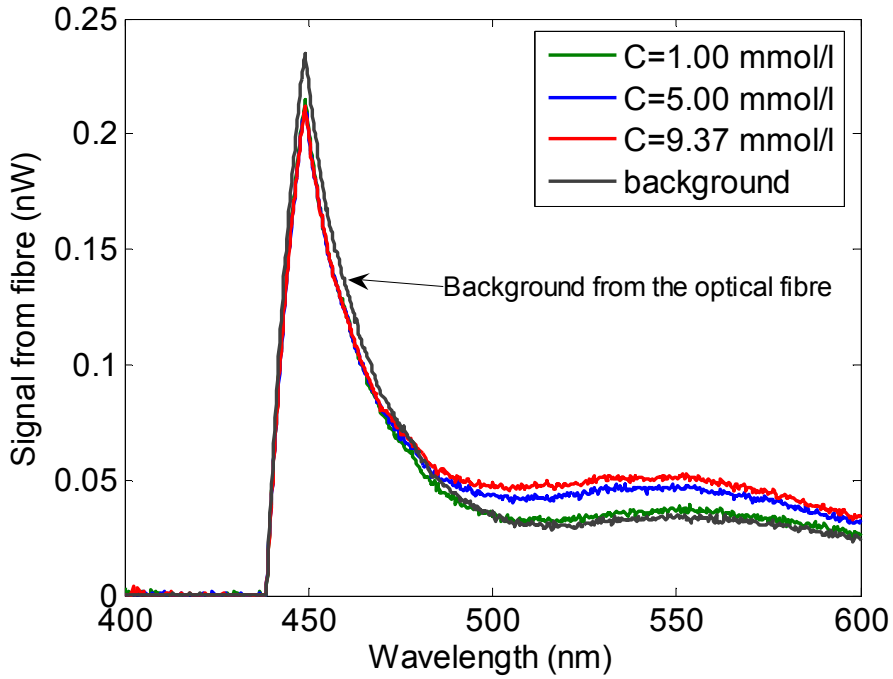

(a)

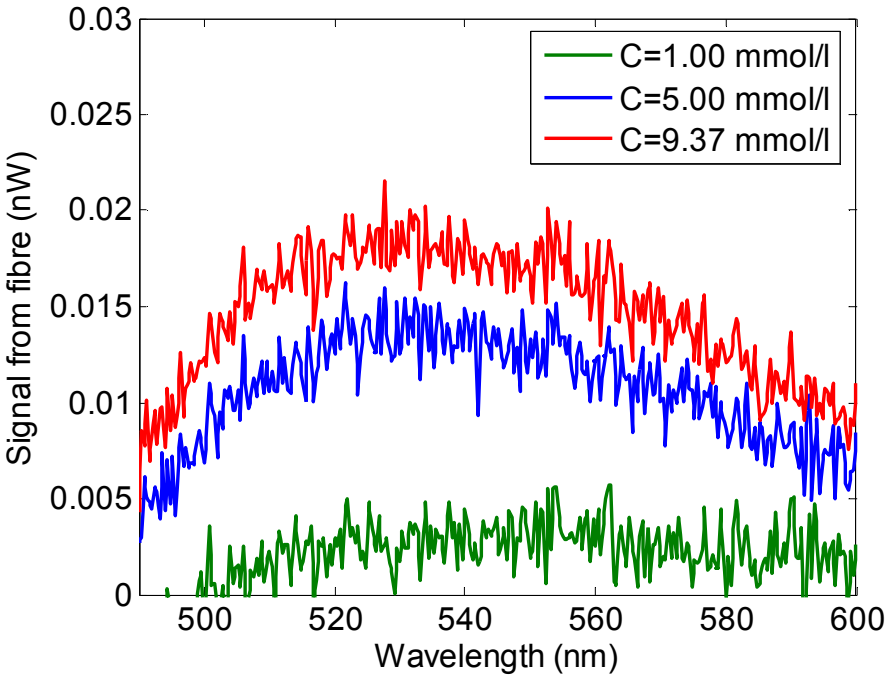

(b)

Figure 4.20. Spectral characterization of the sensing system for a 200 μm IR Fibreguide sensing fibre, 448 nm Iridian LP filter (a). Fluorescence spectrum with the subtracted background is also shown (b).

Further experiments were performed to compare the efficiency of fibres with different core diameters. An experiment with 600 μm core fibre showed a lower

coupled fluorescence signal (by about one order of magnitude) compared with the 200 μm core fibre. This result agrees with the theoretical estimation of the evanescent field interaction given in Section 3.2.2, where it was shown that the amount of power available for the evanescent interaction is inversely proportional to the fibre core radius. This resulted in a corresponding deterioration in signal/noise ratio. In addition, the 200 μm core fibre was easier to handle due to the smaller bend radius and less fragile declad section. Therefore, the 200 μm fibre was chosen for further testing.

4.4 Summary

Experimental work was carried out to evaluate a detection method based on the measurement of water ingress into conventional optical fibre during the corrosion process. This provided some promising results. However, at this stage the approach appears to be incompatible with distributed sensing requirements. This method may be attractive for sensor designs based on special types of fibre glasses which possess hydroscopic properties.

An optical fibre sensor based on etched D-fibre was found unattractive due to difficulties of coupling the output of laser diode sources into the fibre, difficulties in process control while using HF etching on a large scale and difficulties with connecting (splicing) D-fibre to conventional fibres or even other D-fibres.

The experimental results presented here have demonstrated the effect of exciting fluorescence in the area surrounding the core and coupling a detectable amount of fluorescence into the guided modes of the exposed core optical fibre sensor. The results support the theoretical basis of the model, which was based on guided light propagating in the optical fibre interacting with the environment via the evanescent field. However, the results also suggest that additional factors, such as background emission and the dependence of the fluorescence excitation on the propagating modes in the fibre, might have a significant deleterious effect on the performance in practice. As mentioned earlier, impurities and/or structural defects within the silica materials, as well as chemicals from the remaining cladding material on the surface of the core may produce fluorescence peaks, in addition to low levels of broadband spontaneous emission from the laser diode. Thus, to evaluate the factors which contribute to the background

emission, further investigations using excitation by a source with broad spectral range were undertaken. The results will be discussed in Chapter 5.

Chapter 5

Characterization of large core fibre sensor

In this chapter, the analysis of the absorbance and fluorescence response of the multimode optical fibre evanescent wave sensor is presented. The theoretical treatment is based on a geometrical optics approach which incorporates the wave effects (Snyder and Love 1983), (Rayss and Sudolski 2000). Experimental results were obtained with a length of multimode step-index plastic clad silica (PCS) fibre whose cladding was removed from a section at the fibre far end. The sensing region was immersed in various solutions to emulate different sensing conditions and investigate the sensor behaviour using the developed theoretical model. In addition, the effect of excitation wavelength was studied as well as the influence of launching conditions on the sensor performance.

5.1 Transmission dependence on refractive index

We will consider an optical fibre sensor based on large core fibre; interaction with the media under detection is proposed to be through the evanescent field. As mentioned before, the sensing mechanism could be based on either absorption or fluorescence. Both mechanisms need an estimation of the absorption in the sensing area – in our case the region where the cladding is modified. This estimation relates to the sensitivity because it characterises the level of interaction with the environment, which defines measured losses for the absorption method or the energy available for fluorescence excitation for the fluorescence method. Thus the sensitivity depends on the level of interaction with the environment for both intensity (absorption) and wavelength modulated (fluorescence) sensors. Signal processing and measurement interpretation depends on several factors. For example, a change in the detected signal could be caused by a change in the sample concentration or by a change in the refractive index of a polymer cladding due to environmental moisture. In the case of open core fibres,

frequent recalibration might be necessary to account for changes in the refractive index around the core.

5.1.1 Theory of waveguide transmission

The theoretical description of the evanescent wave sensor can be based either on mode analysis employing electromagnetic field theory or geometrical optics. The mode analysis can potentially give an exact description of the sensor, but needs complicated mathematical methods. Even for a few-mode fibre many simplifications have to be made. For highly multimode structures such as large core fibres, where the number of modes may exceed tens of thousands, finding an exact solution becomes an inaccessible task (Rayss and Sudolski 2000).

On the other hand, classical geometric optics provides an acceptable approximate description of light propagation in situations where the refractive index has no significant variations over distances comparable to the wavelength of light (Snyder and Love 1983). This is the case for multimode optical fibres used in sensing applications. The most direct and intuitive way to describe light propagation in multimode fibres is by tracing rays along the fibre core.

Therefore our intention is to describe the sensing mechanism in the multimode fibre sensor through the use of ray tracing methods. The power loss which is employed in the sensing process occurs in the cladding area or in the area where the fibre cladding is replaced with the sensitive material; formally this area can still be called a cladding. The power loss due to a light-absorbing cladding cannot be described directly by geometrical optics, because this loss occurs beyond the ray path. It must therefore be described by incorporating wave effects into the ray description as it is introduced in (Snyder and Love 1983).

The power transmitted by an optical fibre with absorbing cladding may be written in the form

$$P(z) = P(0)\exp(-\gamma_{cl} z), \tag{5.1}$$

where z is the distance along the fibre length, $P(0)$ is the power transmitted in the absence of an absorbing species in the cladding and γ_{cl} is an evanescent absorption

coefficient. This coefficient may be related to the bulk absorption coefficient α of the cladding material for two separate situations: either when all bound modes are launched and consequentially involved in the evanescent wave interaction, or when only selected modes are launched. In the first case the fraction of power (P_{clad}/P) propagating outside the core should be taken into account as described in Chapter 3. The second case is discussed here.

The approach is to describe light propagation along the fibre in terms of ray paths as done in geometrical optics and to assume that a ray only loses power at reflecting or turning points. The fraction of ray power lost at each reflection can be found by treating the ray locally as a plane wave. In the case of a fibre with a step-profile refractive index, the expression for power loss is identical to the expression for plane-wave reflection from a planar interface. Given the expression for power loss at each reflection, the attenuation of ray power along the fibre due to cladding absorption can be defined in terms of the density of reflection (number of reflections per unit length) which is determined by geometrical optics.

The attenuation of ray power is fully characterised by the evanescent absorption coefficient which can be written as:

$$\gamma_{cl} = NT, \tag{5.2}$$

where N is the number on reflections per unit length and T is the fraction of ray power lost at a single reflection.

Derivation of the expression for the evanescent absorption coefficient is presented in (Snyder and Love 1983):

$$\gamma_{cl} = \frac{\alpha}{V}\left(\frac{\vartheta_z}{\vartheta_c}\right)^2 \frac{1}{\sqrt{1-\left(\vartheta_z/\vartheta_c\right)^2 \sin^2(\vartheta_\varphi)}} \quad 0 \le \vartheta_z \le \vartheta_c \tag{5.3}$$

where V is the waveguide parameter corresponding to the core and cladding refractive indices n_{co} and n_{cl}:

$$V = \frac{2\pi\rho}{\lambda}\sqrt{n_{co}^2 - n_{cl}^2}\,, \tag{5.4}$$

ρ is the fibre core radius, λ is the light wavelength,

ϑ_z and ϑ_φ are the ray sperical polar angles to the fibre axial direction,

ϑ_c is the complementary critical angle defined by core and cladding refractive indices.

The expression for γ_{cl} is accurate for step-index profile fibres with a non-absorbing core and slightly absorbing cladding. The weakly guiding approximation was also applied. It describes all bound rays, including meridional and skew rays with the exception of those few rays propagating close to the critical angle. Note that for a fixed value of ϑ_z, attenuation is a maximum when the ray is meridional ($\vartheta_\varphi = \pi/2$), and decreases with increasing skewness. Although the skew rays can propagate for longer distances, their utilisation in the sensing process is limited because of the low level of interaction.

We will further simplify the expression for the evanescent absorption coefficient by eliminating the skew rays and once more using the weakly guiding approximation:

$$\gamma_{cl} = \frac{\alpha\lambda}{2\pi\rho n_{co}} \frac{\vartheta_z^2}{\vartheta_c^3}, \tag{5.5}$$

where

$$\vartheta_c = \sqrt{1 - \left(n_{cl} \big/ n_{co} \right)^2} \,. \tag{5.6}$$

In the general case of an evanescent field optical fibre sensor the weakly guiding approximation is not always applicable. The variation in the surrounding refractive index in the sensing area can be significant and low refractive index solutions such as aqueous solutions are widely used for sensing purposes. For an evanescent field sensor with low index cladding in the sensing area, the difference between core and cladding at the launch end of the fibre is much smaller than in the sensing area. Accordingly it is not possible to launch bound modes that will traverse the core/cladding interface in the sensing area at angles close to the critical angle. The situation is illustrated in Figure 5.1.

Plastic clad large core silica fibres which are widely used in sensing applications, including the present work, are normally characterised by two values of numerical aperture. One is the theoretical numerical aperture calculated from the refractive indices

of the core and cladding materials. It defines a critical angle and respectively an acceptance angle at the launching point. This NA persists only for short fibre lengths (~50 m) because guided rays near the critical angle are selectively attenuated by the plastic cladding, as shown in Equation 5.1. The original numerical aperture and acceptance angle are reduced to an effective or "steady state" value for distances over 50 m.

The above-mentioned facts allow us to use the expression for the evanescent absorption coefficient in the weakly guiding approximation, even if it is not the case for evanescent sensing in general.

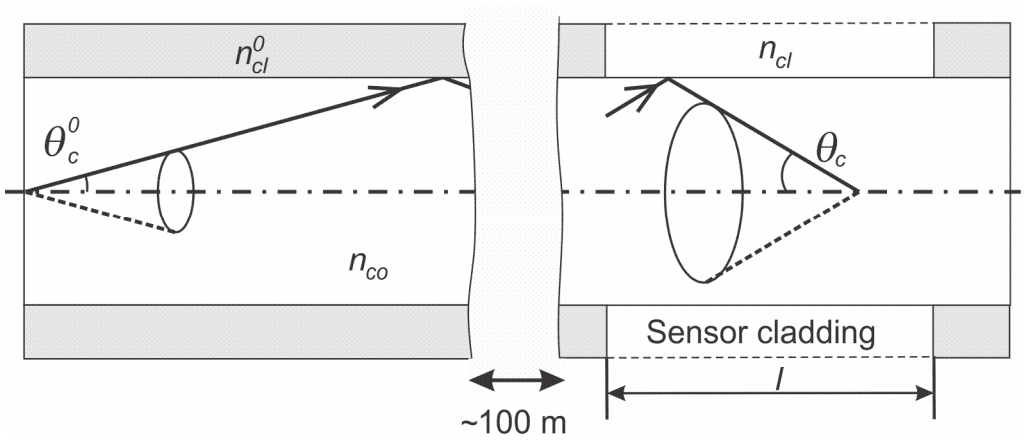

Figure 5.1. Acceptance cones and complimentary critical angles at the launching point and at the sensing area. Here it is assumed that $n_{cl} < n_{cl}^0$.

The expression (5.5) gives an evanescent absorption coefficient for each ray or mode propagating along the fibre within the acceptance angle shown at Figure 5.1. The ray propagation is characterised by the angle between the ray and the axial direction – ϑ_z.

The power transmitted by this particular ray propagating along an optical fibre with absorbing cladding is:

$$P_z(l) = P(0)\exp\left(-\frac{\alpha\lambda}{2\pi\rho n_{co}}\frac{\vartheta_z^2}{\vartheta_c^3}l\right), \tag{5.7}$$

where l is the length of the sensing fibre section with the absorbing cladding (see Figure 5.1). It is assumed that before and after the sensing section light propagates with negligible attenuation.

During a measurement the average value of light intensity, corresponding to a certain range of ϑ_z angles, is recorded. The number of modes or rays to be taken into account is defined by a mode distribution over the fibre cross section. In other words it is necessary to establish how many modes propagate at every angle ϑ_z and summarise those intensities through integration of the expression (5.7) employing a suitable mode distribution function.

Then the transmitted power by all excited modes of optical fibre with an absorbing cladding may be written:

$$P(l) = \int I(\vartheta_z) P_z(l) d\vartheta_z = \int I(\vartheta_z) P(0) \exp\left(-\frac{\alpha\lambda}{2\pi\rho n_{co}} \frac{\vartheta_z^2}{\vartheta_c^3} l \right) d\vartheta_z \qquad (5.8)$$

where $I(\vartheta_z)$ is the mode distribution function.

To get an idea of the mode distribution, experimental images of the output light distribution from the large core plastic clad optical fibre were used. The exact experimental set up will be presented later in this chapter. Typical output from the highly multimode optical fibre is presented at Figure 5.2. The CCD image of the fibre output on a screen shows a typical granular pattern for coherent excitation, consisting of a very large number of speckles. The distribution of these speckles can not be exactly represented by a smooth regular function. As a reasonable approximation Gaussian and quadratic functions were evaluated to describe the input intensity distribution. A uniform distribution was tested as an alternative.

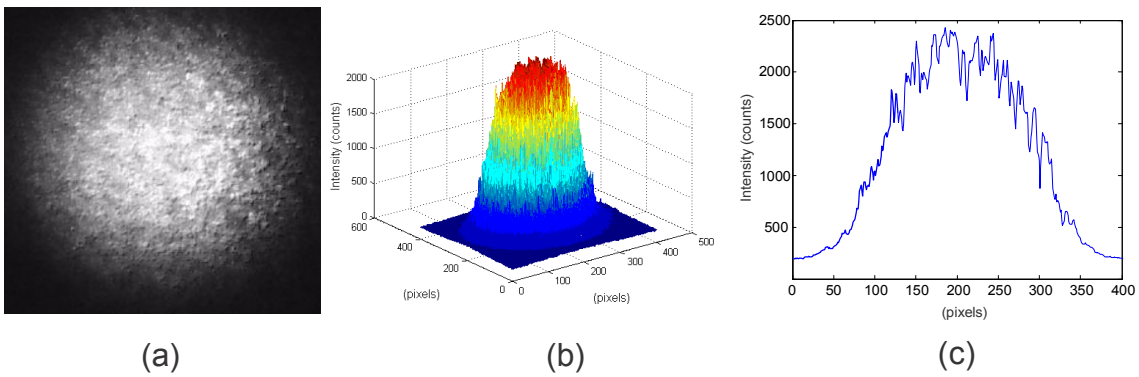

Figure 5.2. Output light distribution from the large core plastic clad optical fibre. (a) is the CCD image of the output from the fibre on a screen, (b) is a 3D representation of the light intensity distribution, (c) is the intensity profile at the image cross section.

In Table 5.1 graphical representations of the different input intensity distributions and their analytical expressions are shown. The formulae include parameters *s* for the Gaussian input intensity distribution and parameter *b* for the quadratic and uniform distributions. These parameters represent the widths of the input distributions and are related to the acceptance angle of the fibre. However, they can not be substituted simply by the fibre acceptance angle which is calculated from the total internal reflection critical angle on the core/cladding interface as it seems at a first glance. Values of the *s* and *b* parameters depend on the abovementioned effective or "steady state" acceptance angle values as well as the number of modes actually launched into the sensor. Therefore they can be considered as independent parameters for the input intensity distributions. Parameter I_0 represents an absolute maximum value of the input intensity.

Intensity measurements typically undergo a normalization process to cancel differences in the experimental routine such as different levels of laser excitation, variations in the connections losses for different measurement runs, etc. For that reason, the optical fibre sensor transmission is a convenient and representative factor to evaluate the sensor performance theoretically and experimentally. The sensor transmission can be written as:

$$P_{tr} = \frac{P(l)}{P^{total}(0)}, \tag{5.9}$$

where $P^{total}(0)$ is the power transmitted by all modes in the absence of an absorbing species in the cladding. It can be found by integration of the expression for the input intensity distribution over all angles corresponding to the propagating modes.

Table 5.1. Graphical representations of the different input intensity distributions and their analytical expressions.

INPUT INTENSITY DISTRIBUTION		
GAUSSIAN	QUADRATIC	UNIFORM
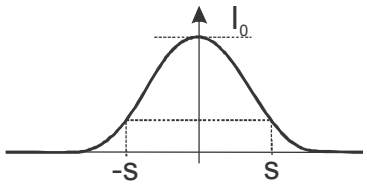	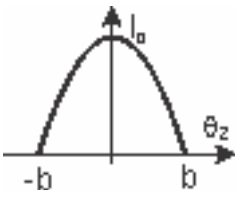	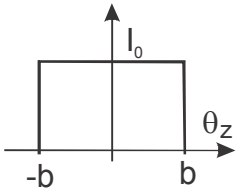
$I(\vartheta_z) = I_0 \exp\left(-\frac{1}{2}\left(\frac{\vartheta_z}{s}\right)^2\right)$	$I(\theta_z) = I_0\left(1-\left(\frac{\theta_z}{b}\right)^2\right),$ $-b \le \theta_z \le b$ $I(\theta_z) = 0,\ \theta_z < -b,\ \theta_z > b$	$I(\theta_z) = I_0,\ -b \le \theta_z \le b,$ $I(\theta_z) = 0,\ \theta_z < -b,\ \theta_z > b$

Now an expression can be derived for the sensor transmission for every case of the Gaussian, quadratic and uniform input intensity distributions using the formulae (5.8), (5.9) and Table 5.1. The parameter $A = \frac{\alpha\lambda l}{2\pi\rho n_{co}}$ is introduced to reduce the expressions and make them easier to read.

Then for the Gaussian distribution:

$$P(l) = \int_{-\infty}^{+\infty} I_0 \exp\left(-\frac{1}{2}\left(\frac{\vartheta_z}{s}\right)^2\right)\exp\left(-A\frac{\vartheta_z^2}{\vartheta_c^3}\right)d\vartheta_z \tag{5.10}$$

$$\text{and } P^{total}(0) = \int_{-\infty}^{+\infty} I_0 \exp\left(-\frac{1}{2}\left(\frac{\vartheta_z}{s}\right)^2\right)d\vartheta_z \tag{5.11}$$

The expression for the sensor transmission for a Gaussian input intensity distribution is:

$$P_{tr} = \frac{1}{\sqrt{1+\frac{2s^2A}{\vartheta_c^3}}} \tag{5.12}$$

For the quadratic input intensity distribution:

$$P(l) = \int_{-b}^{b} I_0 \left(1 - \left(\frac{\vartheta_z}{b}\right)^2\right) \exp\left(-A\frac{\vartheta_z^2}{\vartheta_c^3}\right) d\vartheta_z \tag{5.13}$$

$$P^{total}(0) = \int_{-b}^{b} I_0 \left(1 - \left(\frac{\vartheta_z}{b}\right)^2\right) d\vartheta_z \tag{5.14}$$

and $$P_{tr} = \frac{B}{\left(b\sqrt{\frac{A}{\vartheta_c^3}}\right)^3}\left(\operatorname{erf}\left(b\sqrt{\frac{A}{\vartheta_c^3}}\right)\left(\frac{2b^2A}{\vartheta_c^3} - 1\right) + \frac{2b}{\sqrt{\pi}}\sqrt{\frac{A}{\vartheta_c^3}}\exp\left(-\frac{b^2A}{\vartheta_c^3}\right)\right) \tag{5.15}$$

where B is a constant parameter and erf is the error function.

The expressions for the input, output power and sensor transmission for the case of a uniform input intensity distribution can be written as follows:

$$P(l) = \int_{-b}^{b} I_0 \exp\left(-A\frac{\vartheta_z^2}{\vartheta_c^3}\right) d\vartheta_z \tag{5.16}$$

$$P^{total}(0) = \int_{-b}^{b} I_0 d\vartheta_z \tag{5.17}$$

$$P_{tr} = \frac{\sqrt{\pi}}{2\sqrt{Ab}}\sqrt{\vartheta_c^3}\operatorname{erf}\left(b\sqrt{\frac{A}{\vartheta_c^3}}\right) \tag{5.18}$$

All of the expressions for P_{tr} depend on the sensor cladding refractive index in a complicated way through the complimentary critical angle $\vartheta_c = \sqrt{1 - \left(n_{cl}/n_{co}\right)^2}$, where n_{cl} is the sensor cladding refractive index. Nevertheless they demonstrate similar behaviour as it is depicted in Figure 5.3.

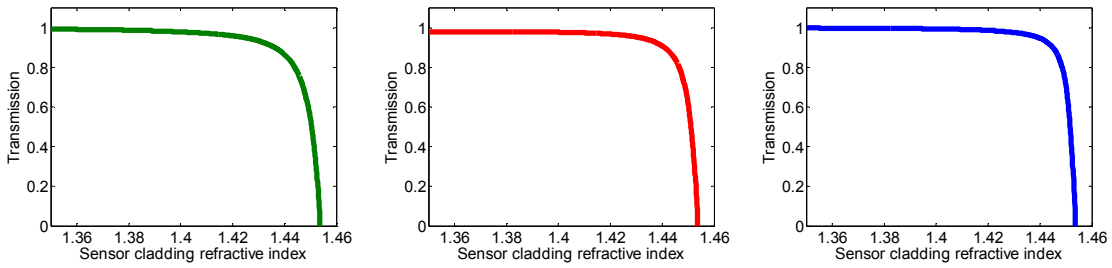

(a) (b) (c)

Figure 5.3. Sensor transmission (P_{tr}) for the different input intensity distributions: (a) Gaussian, (b) quadratic and (c) uniform.

5.1.2 Sensor performance dependence on the sensor cladding refractive index

The expressions derived in Section 5.1.1 characterising the optical fibre performance can be justified by an experiment providing a change in the sensor working conditions such as the cladding refractive index. The environment of the optical fibre sensor was changed by immersing the sensing fibre in a series of liquid mixtures where the refractive index was varied. A two component mixture of dimethyl sulfoxide (DMSO) and ethanol was chosen to allow refractive index variation from 1.36 to approximately 1.46, which covers the range of the guiding property of a silica core optical fibre. The chosen solvents not only provided a suitable refractive index variation range but also effectively dissolved an organic optical absorber which was used in further experiments for the sensor characterisation.

It was necessary to establish a method for preparing mixtures with the specified refractive index and to control it with suitable precision. The Lorentz-Lorenz equation is the most frequently used and empirically proven rule to express the refractive index of a fluid (Born and Wolf 1999). According to this equation, the refractive index n is related to the polarizability α of the fluid molecules and to the fluid density ρ by:

$$\frac{n^2-1}{n^2+2}=\frac{4}{3}\pi\rho\alpha \tag{5.19}$$

Molar refractivity can be introduced as:

$$R = \frac{n^2 - 1}{n^2 + 2}\frac{M}{\rho}, \tag{5.20}$$

where M is the molar weight of the fluid substance.

For a system in which simple mixing occurs without any chemical reactions happening, the additivity principle applies to molar refractivity. Therefore for a binary mixture of x mole fraction of component 1 and (1-x) mole fraction of component 2, the additive refractivity is given by:

$$R_{add} = R_1 + R_2 = \frac{n_1^2 - 1}{n_1^2 + 2}\frac{xM_1}{\rho_1} + \frac{n_2^2 - 1}{n_2^2 + 2}\frac{(1-x)M_2}{\rho_2}, \tag{5.21}$$

where R_1 and R_2 are the refractivity of each mixture component,

n_1 and n_2 are the refractive indices of each mixture component,

ρ_1 and ρ_2 are the densities of each mixture component,

M_1 and M_2 are the molar weights of the mixture components.

When we are dealing with mixtures with a large discrepancy between the sizes of the constituting molecules, volume fraction is a useful alternative to the mole fraction (Menra 2003). Also the volume fraction can be directly measured in the experiment. Introducing the volume fraction $\varphi = x\frac{M}{\rho}$, the mixture refractivity might be written:

$$R_{add} = \varphi_1 \frac{n_1^2 - 1}{n_1^2 + 2} + \varphi_2 \frac{n_2^2 - 1}{n_2^2 + 2}, \tag{5.22}$$

where φ_1 and φ_2 are the volume fractions of each component, $\varphi_1 + \varphi_2 = 1$. Therefore the Lorentz-Lorenz equation for binary liquid mixtures can be written:

$$\frac{n^2 - 1}{n^2 + 2} = \varphi_1 \frac{n_1^2 - 1}{n_1^2 + 2} + \varphi_2 \frac{n_2^2 - 1}{n_2^2 + 2}, \tag{5.23}$$

where n is the mixture refractive index.

In the experiment the volume fraction of each component necessary to achieve the required range of refractive index was estimated with the formula (5.23). Then the

refractive index of each mixture was measured using a Palm Abbe Digital Refractometer and adjusted if necessary.

As a rule standard Abbe refractometers measure the refractive index (n_D) at the sodium D_2 resonance line with wavelength λ=589.3 nm. Practically however, the excitation wavelength in the sensor system could be significantly different from the sodium D_2 line. Thus the measured refractive index should be corrected taking into account the dispersion behaviour of the materials and solvents used in the experiment.

The dispersion curves can be described with various dispersion equations. The most common used are the completely empirical Cauchy equation (Jenkins and White 1976):

$$n(\lambda) = A_0 + \frac{A_1}{\lambda^2} + \frac{A_2}{\lambda^4} + \frac{A_3}{\lambda^6} \tag{5.24}$$

and the Sellmeier equation (Paschotta 2008):

$$n(\lambda) = \sqrt{1 + \frac{B_1\lambda^2}{\lambda^2 - C_1^2} + \frac{B_2\lambda^2}{\lambda^2 - C_2^2}}, \tag{5.25}$$

where the *C* coefficients are related to the centre of gravity of the absorption bands in the relevant spectral range, called the resonance wavelength; *A* and *B* are wavelength independent constants.

In (Kozma et al. 2005) different solvent dispersion curves based on the aforementioned standard models were fitted to the extensive experimental data attained by authors. The models were tested to parameterize the wavelength dependence of the refractive index. It was shown that for different solvents one or the other of the above models produces the best results. Accordingly the Cauchy dispersion formula was used to calculate the dispersion curve for ethanol and the Sellmeier dispersion formula was used to calculate the dispersion curve for DMSO. The constants of the dispersion formulae are shown in Table 5.2.

Table 5.2. Dispersion formula constants (from (Kozma et al. 2005)).

Cauchy dispersion formula constants	Ethanol
A_0 (1)	1.34959
A_1 (nm^2)	4014.712280
A_2 (nm^4)	-59411155
A_3 (nm^6)	3.04975x10^{12}
Sellmeier dispersion formula constants	**DMSO**
B_1 (nm^{-2})	0.04419
B_2 (nm^{-2})	1.09101
C_1^2 (nm^2)	46390.67309
C_2^2 (nm^2)	12215.43949

The plastic clad silica optical fibre used in the sensor design has a core made from synthetic fused silica. Because it has been in common use by the optical industry and research laboratories for many years, information on the physical and chemical characteristics of this material is easily available. In the current investigation experimental values were used for the dispersion curve of synthetic pure silica (Kaye and Laby 2005).

5.1.3 Effect of absorption

The effect of absorption was experimentally investigated by measuring the absorption detection efficiency for an infrared fluorescent organic dye (IR-125). Its optical properties were described in detail in Section 4.3.2. The absorption peak of IR-125 is close to the laser diode wavelength of 785 nm. IR-125 was added to DMSO and ethanol solutions to simulate the effect of cladding refractive index variation as was explained before.

A sensing region of length 20 cm was prepared in a step index plastic clad silica (PCS) fibre (Anhydroguide APC200/300N, Fiberguide Industries, core diameter 200 μm, cladding diameter 300 μm, buffer diameter 370 μm) by applying the decladding technique described in Section 4.3.1.

Figure 5.4 shows the experimental setup used for the measurements performed in this study. For transmission measurements, a solid state infrared laser diode emitting CW at a wavelength of 785 nm was used. This wavelength corresponds to the maximum absorption peak of IR-125 and was coupled into a 100 m length of the sensing fibre. The transmitted power was detected with a power meter (Newport fiber optic detector with 818-IS-1 head).

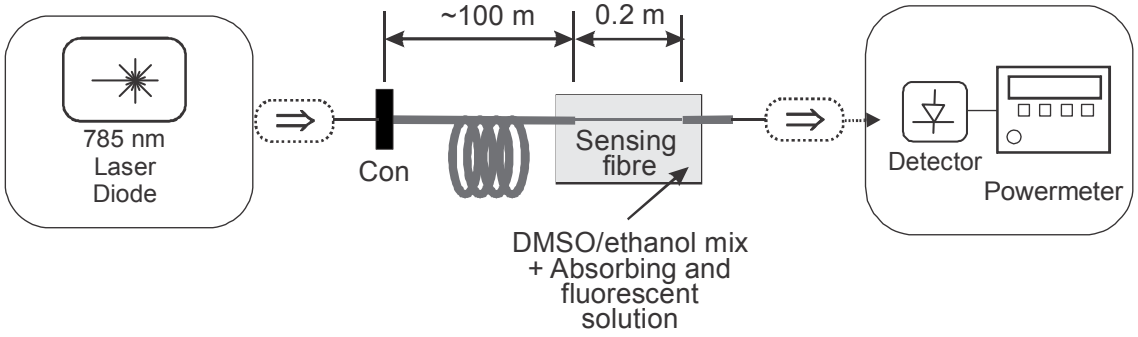

Figure 5.4. Experimental arrangement used to investigate the effect of absorption. Con = connector.

During the experiment the concentration of IR-125 was increased gradually, with altogether four different concentrations ($5x10^{-7}$ mol/l, $2x10^{-6}$ mol/l, $5x10^{-6}$ mol/l and 10^{-5} mol/l) being investigated, together with the case of no absorbing dye in the solutions at all. Those concentrations correspond to values of the bulk absorption coefficient of 0.1, 0.4, 1.0, 2.0 cm^{-1}.

The predicted behaviour of the sensor response from the theoretical model described in Section 5.1.1 (Equation 5.12) is shown in Figure 5.5 for the case of a Gaussian input power distribution. Calculation parameters for the sensor response are shown in Table 5.3.These values were indicative of the conditions used in the experiment.

Table 5.3. Calculation parameters for the predicted behaviour of the sensor response.

Parameter	Value
Input intensity distribution	Gaussian
Light wavelength, λ (nm)	780
Length of the sensing fibre with the absorbing cladding, l (m)	0.2
Fibre core radius, ρ (μm)	100
Core refractive index, n_{co}	1.454
Width of the input intensity distribution, s (rad)	0.2

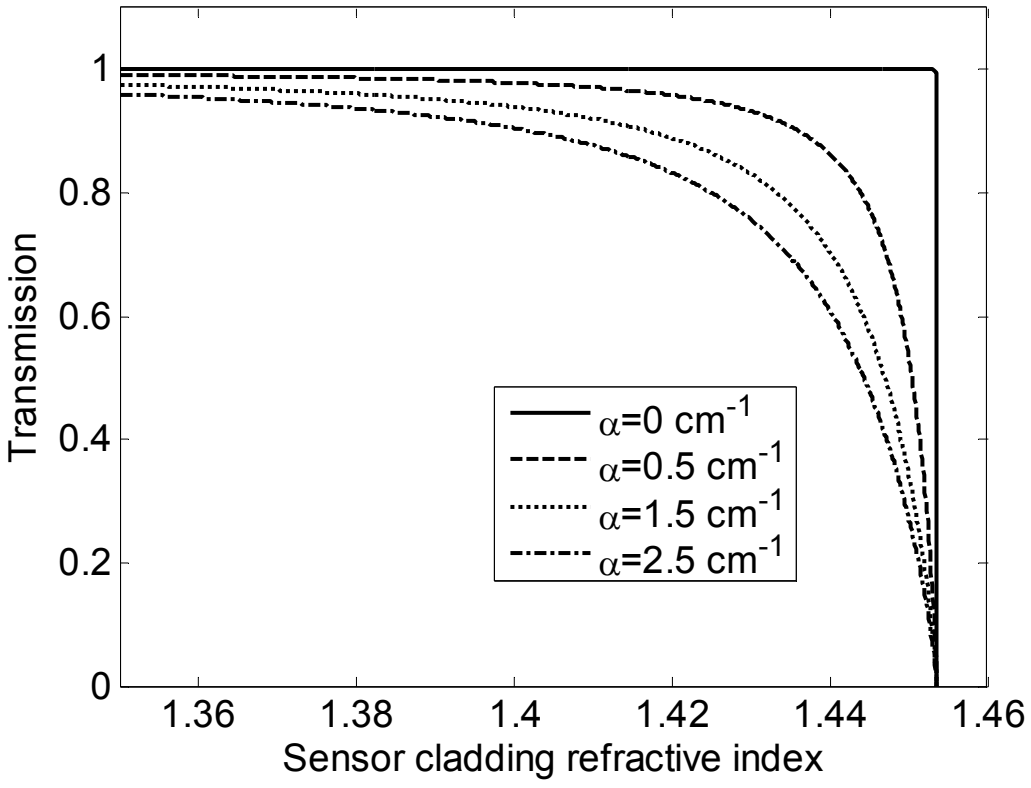

Figure 5.5. Predicted sensor behaviour with a Gaussian input power distribution and variation in the sensor cladding bulk absorption coefficient. α is the sensor cladding bulk absorption coefficient.

With the no absorber the curve is expected to behave as a step function, while increasing the bulk absorption coefficient should result in a more gradual reduction in transmission as the cladding refractive index approaches that of the silica core.

These calculated results were then compared against the measured power transmitted through the sensor section of the fibre immersed in solutions of differing refractive index. The transmission was measured relative to the transmission in pure ethanol. The results are shown in Figure 5.6 for a range of fluorophore concentrations, including the case of no additional absorber.

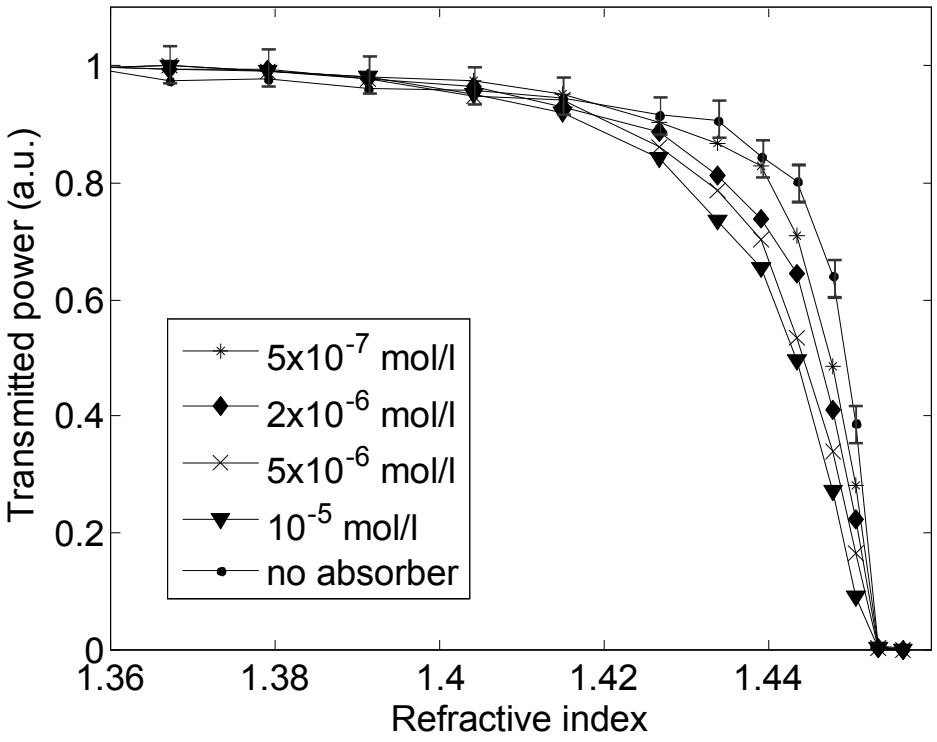

Figure 5.6. Experimental dependence of transmitted power on refractive index and absorbing dye concentration. Error bars are shown for the "no absorber" curve only. Error bars for the other curves were similar, but were omitted from the graph for the sake of clarity.

These results demonstrate that the sensor is relatively insensitive to changes in absorber concentration below about 1.415 refractive index units. However, the relatively small losses shown here might become significant for longer exposed regions in a practical distributed sensing arrangement. For the sensor setup used in this experiment, the absorption dependence is strongest in the refractive index range from 1.43-1.45 as it was expected from the calculated curves.

To estimate how precisely the experimental data agree with the theoretical model, all of the experimental curves were fitted with the expressions (5.12), (5.15) or (5.18) corresponding to different input power distributions. The derived expressions for the sensor response are accurate where the sensor cladding refractive index is lower than core refractive index. Hence the experimental points where refractive index exceeds 1.45 were excluded from the fitting.

The fitting showed an excellent agreement between the predicted and experimental data which can be characterised by means of R-Squared (r^2), also known as the coefficient of determination, which is commonly used to statistically evaluate model fits. Detailed information about the fitting procedure and goodness-of-fit parameters is provided in Appendix 2. For all of the fits the values of R-Squared were greater than 0.9.

In Figure 5.7 the fitted curves corresponding to different input power distributions together with the experimental data set are shown for the case of absorber concentration equal to 10^{-5} mol/l. A similar set of curves were attained for the other concentrations. The consistent agreement between the experimental results and the theoretical predictions confirms that the model provides a satisfactory understanding of the processes occurring in the optical fibre sensing system.

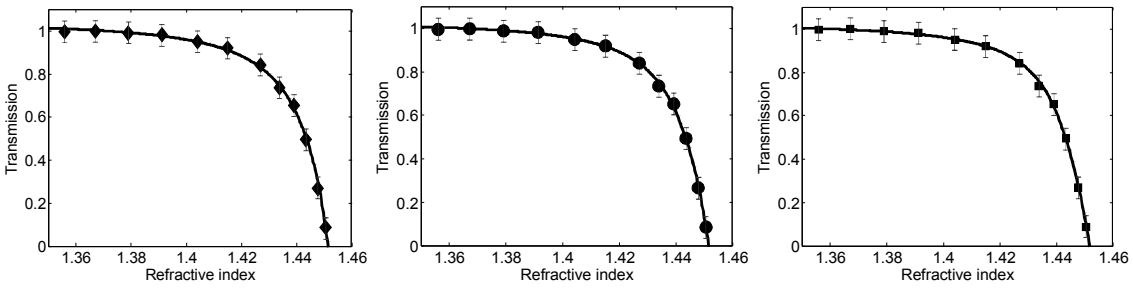

$r^2 = 0.9983$ $r^2 = 0.9991$ $r^2 = 0.9990$

(a) (b) (c)

Figure 5.7. Fitting the experimental sensor response with the models for different input intensity distributions: (a) Gaussian, (b) quadratic and (c) uniform. The points represent the experimental data set.

Analysis of the fitting results demonstrated that the system is insensitive to the exact shape of the input power distribution. A possible explanation could be provided

by the well known “modal noise” phenomenon in optical fibre communication systems. In simple terms, this means that energy carried by multimode optical fibres is constantly redistributed between the modes, whereas the total intensity remains unchanged. For the significantly multimode structure of a large core optical fibre, rapid changes in the speckle structure are inherent due to small external perturbations such as vibration (Oraby et al. 2009), (Spillman Jr et al. 1989). Thus the contribution of each mode to the evanescent interaction would constantly be changing during the sensing process, thereby creating an averaged impact of all modes to the detector. Further analysis of this issue is beyond the scope of this thesis.

The behaviour of the experimental curve without absorber in the solution is different to the step function behaviour expected from the model. Nevertheless a good fit was obtained by applying the model to the transmission curve with zero absorber concentration. Analysis of the fitting parameters shows an equivalent value of the bulk absorption coefficient α of approximately 0.50 cm^{-1}, which corresponds to an absorber concentration of 2.5×10^{-6} mol/l. This suggests that additional attenuation in the absence of an absorber may be caused by surface imperfections of the sensing fibre as well as contamination from the etching process. Further investigation is needed to address this problem, as this additional attenuation will tend to limit the sensor performance.

5.1.4 Measurement of fluorescence

The experimental setup for fluorescence measurements used the same excitation as the transmission measurements, as shown in Figure 5.8. Detection was performed with a PMT (Hamamatsu R928) equipped with an ultrasteep longpass filter (Omega Optics 850 LP, OD $\geq$ 5, edge steepness of 1 %, cut off wavelength 820 nm) to reject light at the excitation wavelength.

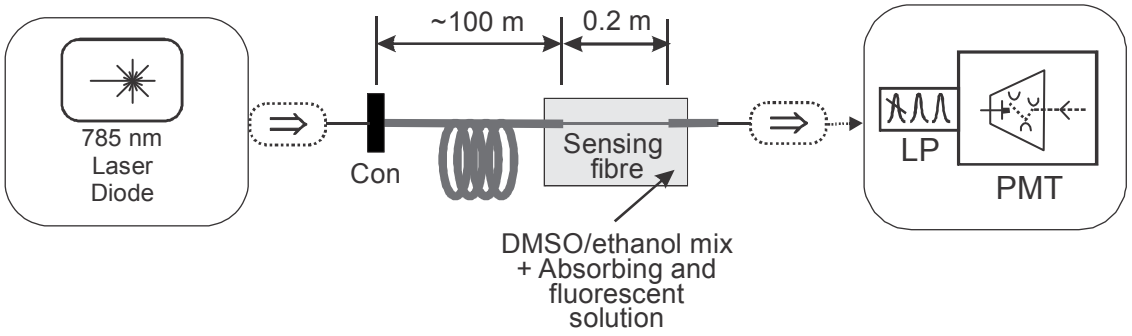

Figure 5.8. Experimental arrangements used in fluorescence measurements. Con = connector; LP = long pass filter.

Figure 5.9 shows the amplitude of the fluorescence signal acquired by means of the PMT for an IR-125 concentration of 10^{-5} mol/l. The fluorescent light is excited via the evanescent field and a small fraction is captured back into guided modes by the same mechanism. The detection sensitivity is relatively low for smaller values of refractive index, but increases for the refractive index above approximately 1.42 until the guiding behaviour is completely lost at $n_{cl} = 1.45$.

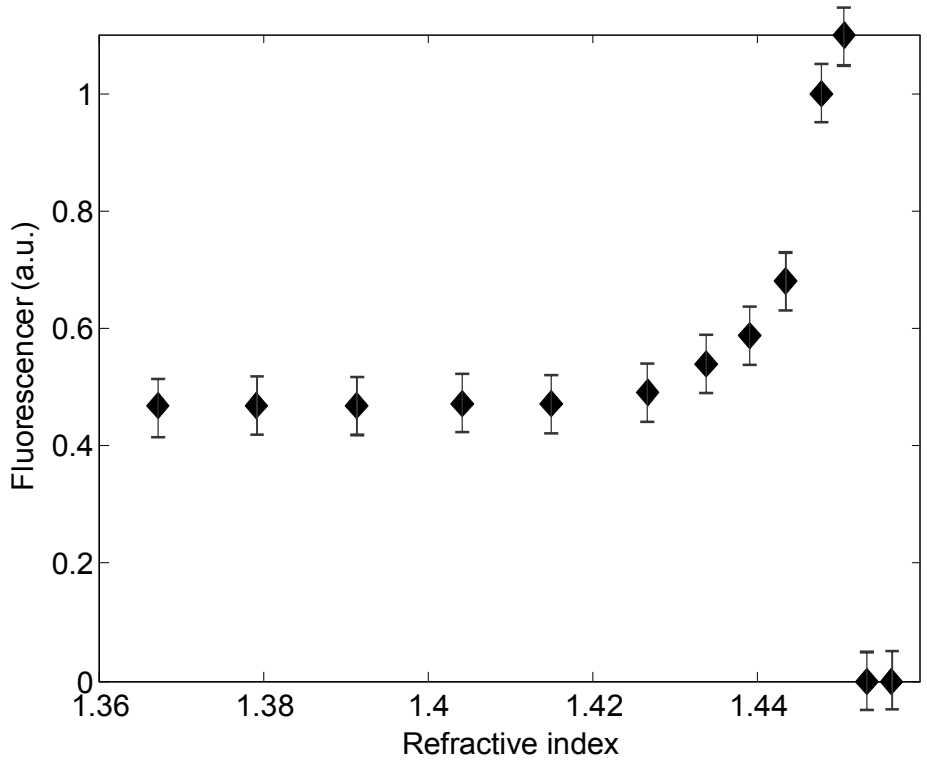

Figure 5.9. Dependence of fluorescence signal intensity on the refractive index in the sensing region. The fluorescence signal is both excited and captured back into guided modes by the evanescent field.

The theoretical model developed in Section 5.1 can also be used to describe the fluorescence response of the sensor. Keeping in mind that all expressions for the sensor transmission give the same quality of fit, the expression (5.12) with the Gaussian input power distribution is chosen for further modification. The detected fluorescence signal is proportional to the absorbed power in the sensor cladding and can be written as:

$$P_{fl} = C\left(1 - \frac{1}{\sqrt{1 + \frac{2s^2 A}{\vartheta_c^3}}}\right), \tag{5.26}$$

where C is a constant.

The experimental fluorescence measurements were fitted with Equation (5.26). The fitting provided excellent results as shown in Figure 5.10. Similarly to the transmission analysis, fluorescence data points with refractive index higher than 1.45 were excluded from the fitting.

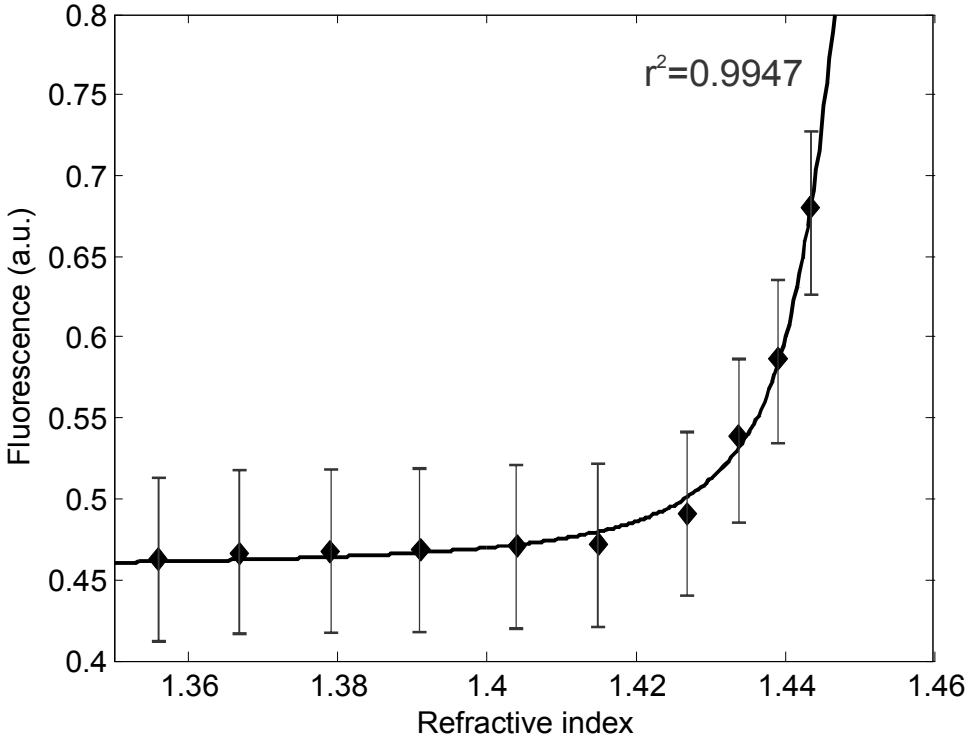

Figure 5.10. Fluorescence sensor response fitted with the Equation (5.9) is represented by the solid line; diamonds are the experimental measurements.

Although it is clear that the detection sensitivity can be significantly improved by careful choice of refractive index in the cladding region, the transmission measurements show that at the same time absorption losses rise significantly as well. In the case of distributed measurements, this improvement in sensitivity will come at the cost of reduced detection range.

5.2 Dispersion effects

The wide range of fluorescent indicators that are available for corrosion sensing, as described in Chapter 1, provide a number of possibilities to design corrosion detection systems. The combination of these various indicators with the multiplexing capability of optical fibre technology provides an opportunity to create distributed sensors that are able to fully characterize corrosion *in situ* by monitoring more than one parameter.

Particularly in corrosion monitoring it would be useful to measure pH, moisture, oxygen and the concentration of by-products. Such an approach would typically require the use of multiple emission sources with different wavelengths. The wavelength range would be dictated by the spectral properties of the indicators involved and could be rather broad.

The experiment presented here is aimed to evaluate large core optical fibre sensor behaviour within the broad wavelength range of excitation.

Broad band measurements of the transmission spectrum were performed with a super continuum optical light source (Super K Compact, Koheras). The supercontinuum output was coupled into the sensing fibre, which was prepared in the same way as for the transmission and fluorescence experiments. The sensor was immersed into DMSO/ethanol mixtures in the same manner as in the previous experiments. Transmitted spectra were recorded with an optical spectrum analyzer (OSA, ANDO AQ-6315E). The experimental setup for the supercontinuum excitation is depicted in Figure 5.11.

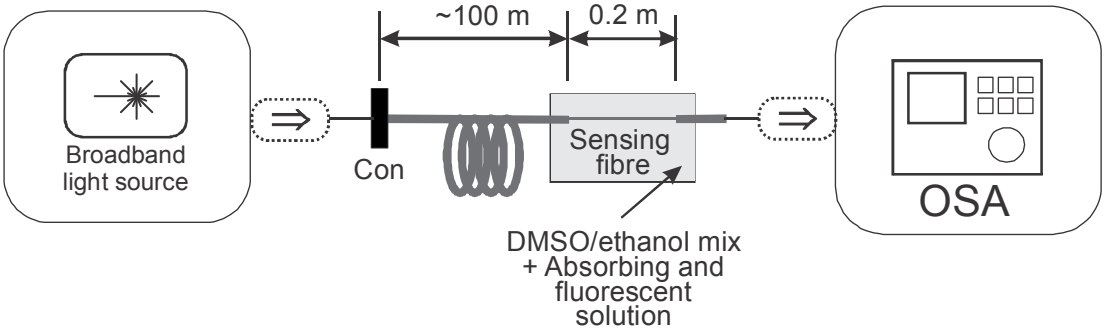

Figure 5.11. Experimental arrangement used in broadband transmission measurements. Con = connector.

The transmission spectra for selected DMSO/ethanol mixtures are shown in Figure 5.12. The shape of each spectrum is due to a combination of the super continuum source spectrum and the fibre absorption spectrum. Specifically, the peaks at ~ 810 nm and 1064 nm were owing to the broadband source spectrum, whereas the dip at 1400 nm corresponds to the water peak and a dip at 1200 nm was caused by H_2 absorption in the fibre material.

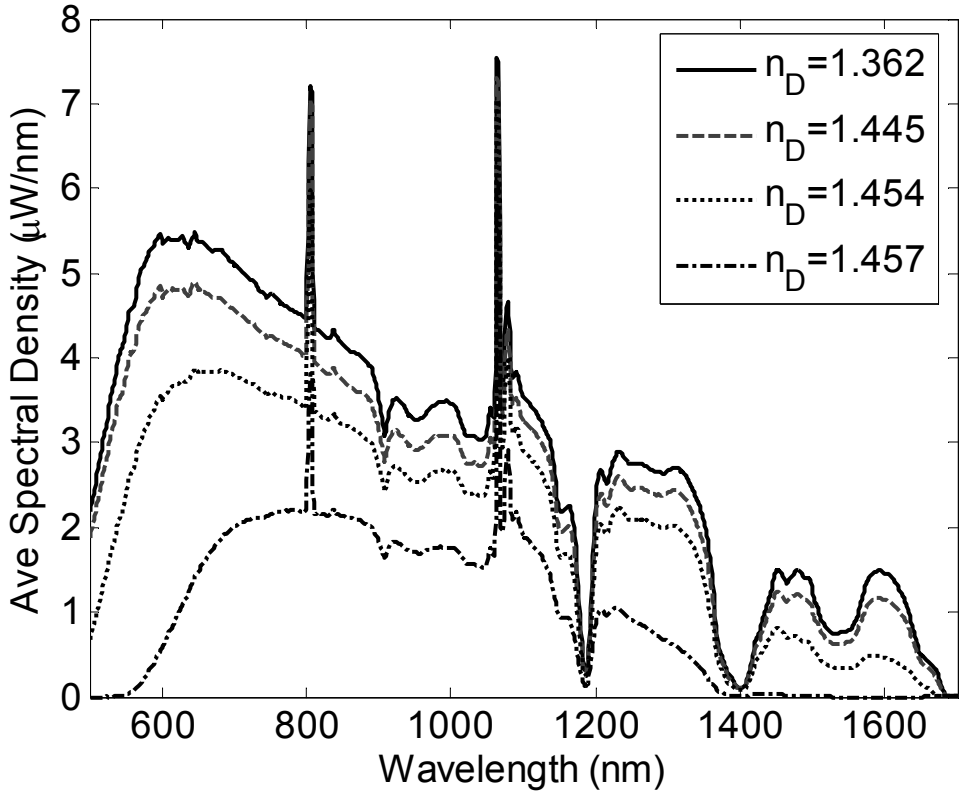

Figure 5.12. Transmission spectra for selected DMSO/ethanol mixtures.

Careful inspection shows that the reduction in transmitted power across the spectra is uneven. To explain this observation, analysis of refractive index behaviour is needed for all components of the optical fibre sensor across the entire spectral region. Therefore dispersion curves were calculated for the DMSO/ethanol mixtures using either the Cauchy or Sellmeier formulae and experimental values were used for the dispersion curve of pure silica, as described in Section 5.1.2. Figure 5.13 shows the spectral dependence of the refractive index of a DMSO/ethanol mixture and the silica. This demonstrates that the waveguide behaviour of the silica-DMSO/ethanol system can vary dramatically across the wavelength range of interest.

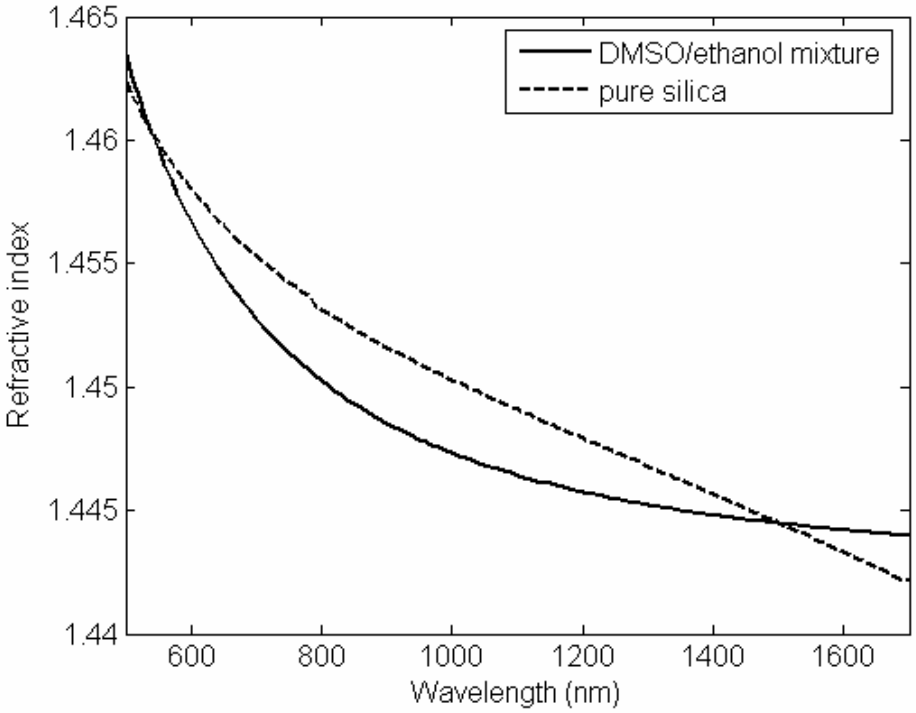

Figure 5.13. Dispersion curves of DMSO/ethanol and pure silica. The DMSO/ethanol mix shown here corresponds to a refractive index of 1.457 at λ=589.3 nm.

Dispersion curves similar to those of Figure 5.13 were calculated for each of the DMSO/ethanol mixtures that were used in this study. This allows the broadband spectra shown in Figure 5.12 to be reinterpreted in a more rigorous fashion, by applying the theoretical considerations presented in Section 5.1.1 to the data. For each DMSO/ethanol mix, the transmitted power at each wavelength can now be associated with a specific refractive index value for the cladding environment, as shown in Figure

5.14. The variation in transmission cut off serves to illustrate the importance of selecting a cladding refractive index appropriate for the operating wavelength of the sensor system.

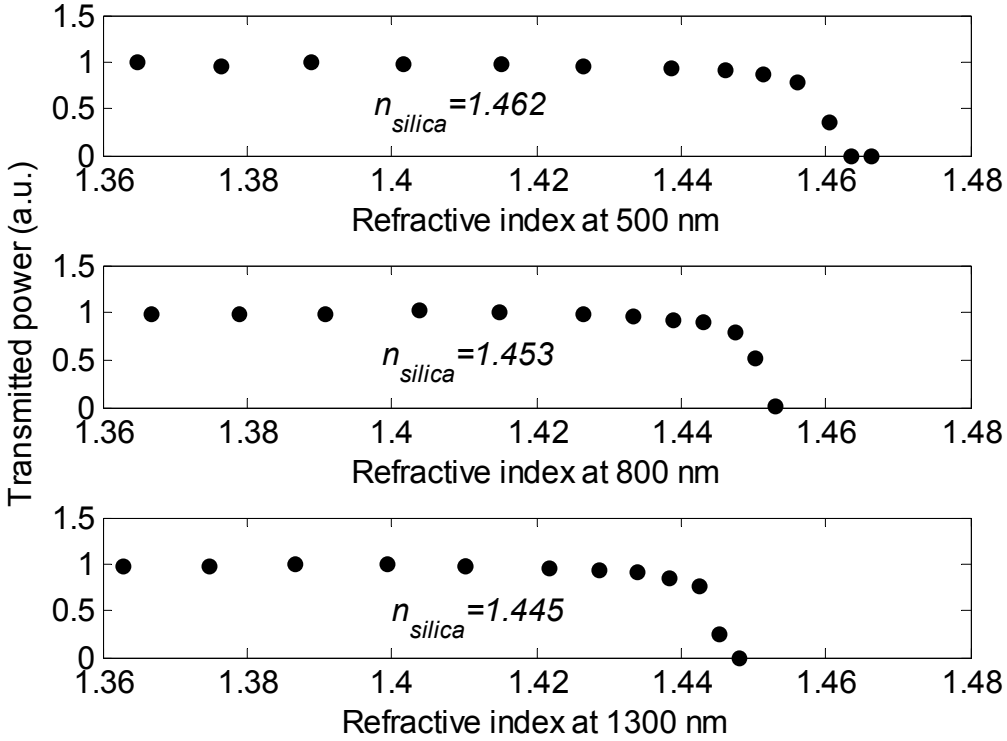

Figure 5.14. Variation in transmission with refractive index at selected wavelengths.

The difference between core and cladding refractive indices plays an important role in determining the range and sensitivity of distributed optical fibre sensors. Dispersion effects in the core and cladding materials can complicate matters when wavelength modulated measurements are performed, or in situations where multiple wavelengths are of interest for amplitude modulated schemes.

5.2.1 Investigation of the attenuation of the optical fibre sensor in the absence of an absorber

As described in Section 5.1.3, the behaviour of the experimental curves without absorber in the solution is different to the step function behaviour expected from the

model presented in this Chapter. This behaviour was observed for the all of the excitation wavelengths in the broad band experiment (see Figure 5.14). Nevertheless, by assuming a finite level of absorption in the model, good fits were obtained for all of the transmission curves with zero absorber concentration. This suggests that there is an additional attenuation in the modified cladding, even in the absence of an extrinsic absorber. SEM analysis of stripped fibre surfaces suggests that this may be caused by small residues of the cladding material on the surface of the sensing fibre (see Figure 5.15). Contamination from the etching process does not appear to play a significant role in this case, as energy dispersive spectroscopy did not reveal any obvious contamination.

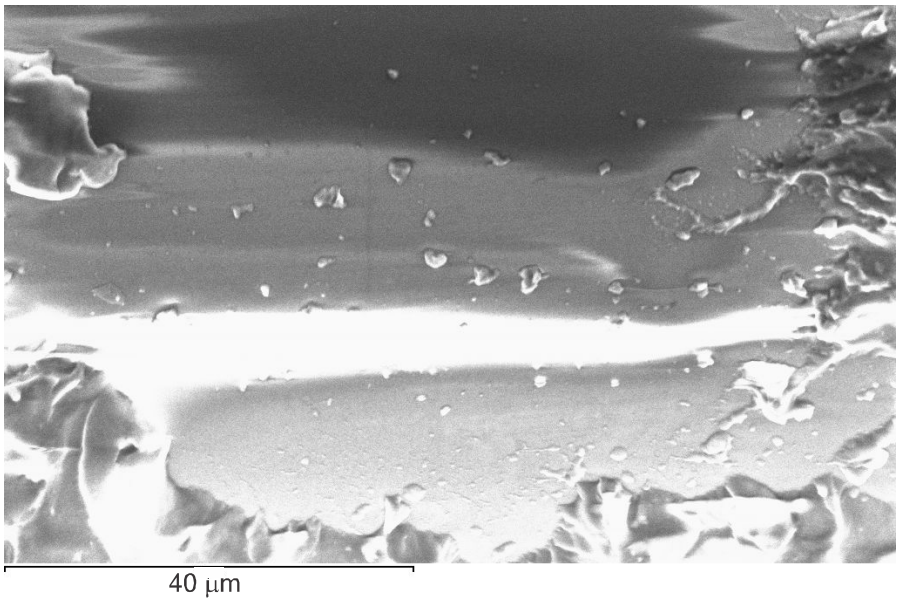

Figure 5.15. Typical SEM image illustrating residues of the cladding material on the surface of the sensing fibre. The longitudinal axis of the fibre is oriented along the horizontal axis of the image.

An intrinsic absorption coefficient, α_0, was extracted from the fitting parameters. The spectral dependence of the extracted parameter is shown in Figure 5.16, with a best fit polynomial proportional to $\lambda^{-1.5}$. This demonstrates that the intrinsic absorption is different from the characteristic λ^{-4} dependence, which is typical for Rayleigh-type scattering losses. Consequently it appears that the intrinsic absorption in the sensor region is caused by residues of the original cladding material. As this intrinsic loss mechanism will reduce the sensitivity of the sensor at low concentrations of an extrinsic

absorber, it is important to reduce the intrinsic losses as much as possible in practical applications.

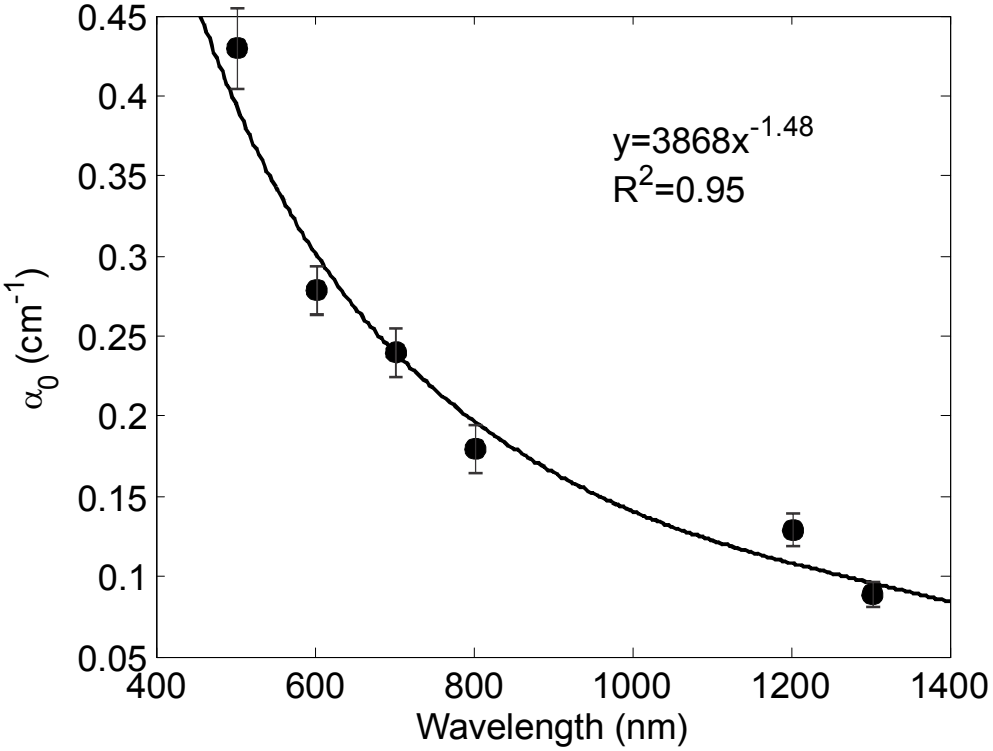

Figure 5.16. The intrinsic absorption coefficient (α_0) of the sensor for zero extrinsic absorber concentration, plotted as a function of wavelength. The best fit curve takes the form $\alpha_0 \propto \lambda^{-n}$, with n ≈ 1.5.

5.3 Modification of mode distribution

This Chapter has dealt with light propagating and interacting with the species in the modified cladding area by only taking into account meridional rays corresponding to the low order modes. This model is typical for the situation of "steady state" light propagation. Thus skew rays were excluded from consideration and the contribution of higher order meridional rays propagating at angles close to the critical angle was limited.

Although the model has demonstrated good agreement with the experimental results for "steady state" measurements, it would be useful to analyse the contribution of higher order modes to the sensor performance. On the one hand, it has been shown that selective excitation of the optical fibre higher modes can significantly improve optical fibre sensor sensitivity (Ma and Bock 2007). On the other hand, the modal distribution in a multimode fibre depends on a number of factors that are present in real detection

systems, such as bends (Khijwania 1999), strain, splices and components such as connectors, couplers, etc. These factors might affect the modal distribution causing mode coupling effects and consequently alter the sensor sensitivity.

To characterize higher order mode generation the Fraunhofer diffraction pattern at the fibre output was collected for the case when the fibre was undisturbed and the case when fibre was coiled once around a 35 mm cylinder. The collected far-field spatial pattern is a direct image of a power distribution of guided modes in the optical fibre (Potyrailo et al. 1999).

The experimental setup consisted of a solid-state infrared laser diode emitting CW at a wavelength of 785 nm and launched into a 100 m piece of large core optical fibre (Anhydroguide APC200/300N, Fiberguide Industries, core diameter 200 μm, cladding diameter 300 μm, buffer diameter 370 μm). The fibre output was projected onto a diffusing screen and the image was collected by means of a CCD camera at a fixed magnification. To populate the higher order modes, the fibre was coiled at a point 50 cm before the fibre far end.

Figure 5.17 presents a comparison of the far field spatial patterns for straight and coiled fibre. The CCD images were analysed to quantify changes in the spatial pattern. Central cross sections of the images were fitted using the Gaussian function, which allowed the full width at half maximum (FWHM) and amplitude to be extracted from the fitting parameters. The results are presented in Figure 5.17. Coiling causes a redistribution of power between fibre propagating modes, resulting in relative widening of the beam image as well as a reduction in amplitude. The broadening of the beam indicates an increased number of modes propagating at angles closer to the critical angle i.e. higher order modes. The total power carried in the fibre will remain the same under an ideal condition when only propagating higher modes are excited. However, in practice, some leaky modes are excited as well and so significant losses in power were observed in the experiment. For that reason a reduction in the distribution amplitude was observed.

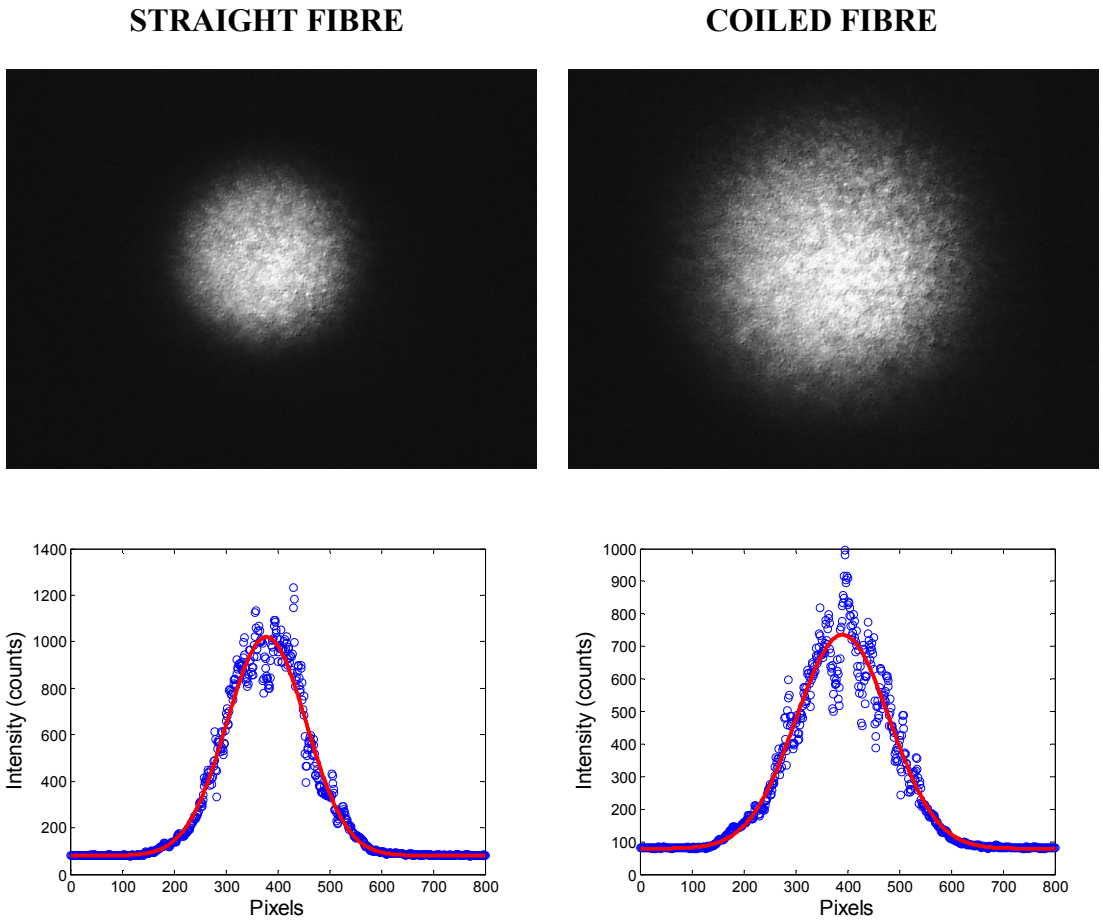

Amplitude = 940 pixels

FWHM = 181 pixels

(a)

Amplitude = 656 pixels

FWHM = 212 pixels

(b)

Figure 5.17. Mode redistribution characterization for (a) straight fibre and (b) coiled fibre. CCD images of the emitted beam (top) are presented together with the corresponding Gaussian fits to the image cross section and fitting parameters (bottom).

5.3.1 Influence of mode population on sensor performance

The influence of the mode population on sensor performance was assessed by measuring the change in the sensor transmission, as well as the ability to excite and couple back fluorescence.

The optical fibre sensor arrangement used in this experiment has the same construction and parameters as that of the previous experiments. The sensor was immersed in a series of IR-125 solutions with different concentrations. In order to adjust the refractive index of the solution for optimum guiding conditions, the IR-125 was dissolved in a 50/50 DMSO/water mixture.

The fibre was coiled once around a 35 mm cylinder at the section just before the sensor to excite higher order modes. The fibre in the sensing region was kept straight, because the intention is to characterise the sensor response to changes in launching conditions, rather than simply increasing the sensor sensitivity.

Transmission measurements were performed using the CW laser diode emitting at wavelength 785 nm. Transmitted power was collected at the far end of the fibre by means of a PMT (Hamamatsu R928) equipped with a neutral density filter to avoid PMT overloading (Figure 5.18).

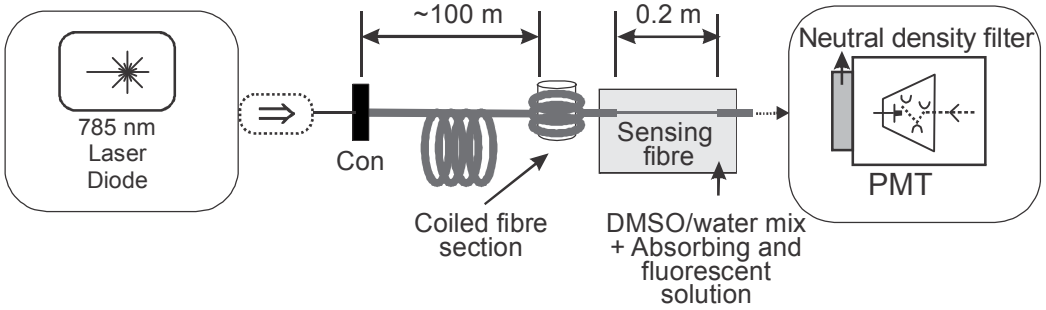

Figure 5.18. Experimental arrangement used in transmission measurements during the higher order mode excitation experiment. Con = connector.

The results of the transmission experiment are presented in Figure 5.19. The voltage measured by the PMT represents the power transmitted by the sensor.

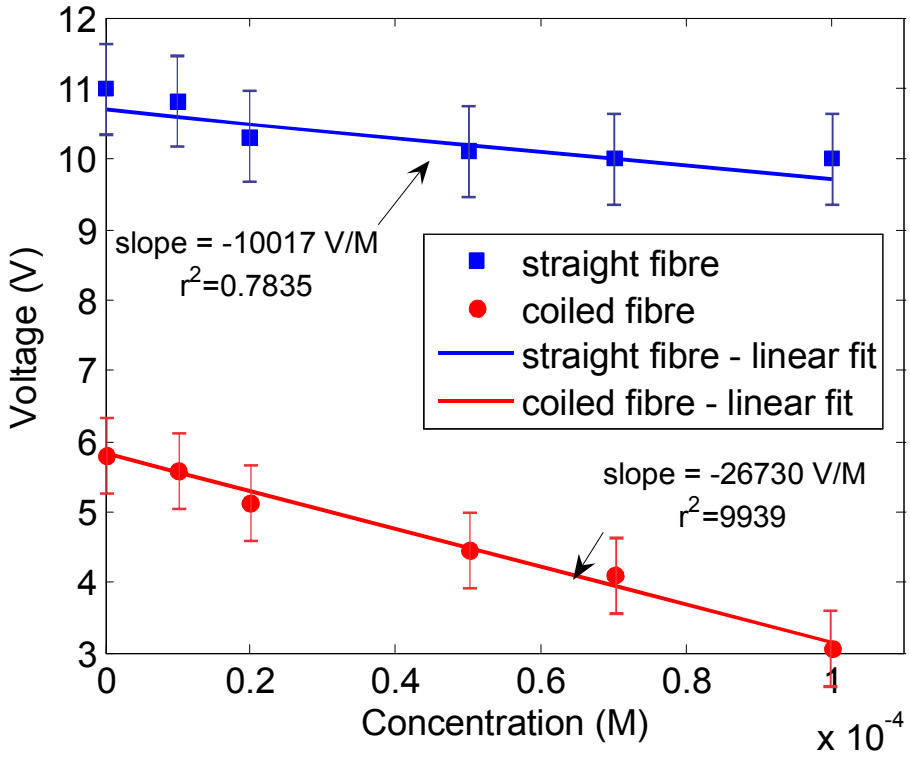

Figure 5.19. Dependence of the optical fibre sensor transmission on the concentration of absorbing dye in the cladding area.

Analysis of the transmission curves shows that introducing the coiling causes a significant drop in the transmitted power characterised by the offset at zero concentration. It indicates that the coiling introduces significant losses that are not related to the absorbance of the IR-125 in the cladding. Those losses most likely are caused by introducing leaky modes in the fibre mode structure. Thus, part of the propagating power is transferred to the optical rays propagating at angles greater than the critical angle, so that the power quickly dissipates in the cladding.

The experimental points were fitted with a linear equation to estimate the slope, which represents sensor sensitivity. Coiling the fibre before the sensor results in more than a twofold increase in sensitivity, which can be attributed to the excitation of higher order modes with strong evanescent field coupling.

Since the fluorescence signal level was expected to be quite low, a detection system with enhanced sensitivity was employed. The principles of pulsed, time-resolved detection using a PMT in single photon counting mode with signal accumulation are described in Chapter 3. The schematic is shown in Figure 5.20 and parameters of the

actual detection system adapted for use in the IR spectral region are provided in Chapter 6.

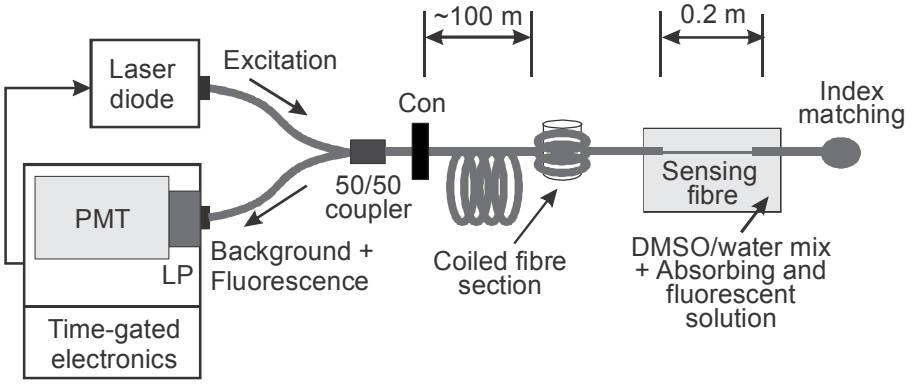

Figure 5.20. Experimental arrangement used in fluorescence measurements during the higher order mode excitation experiment. Con = connector.

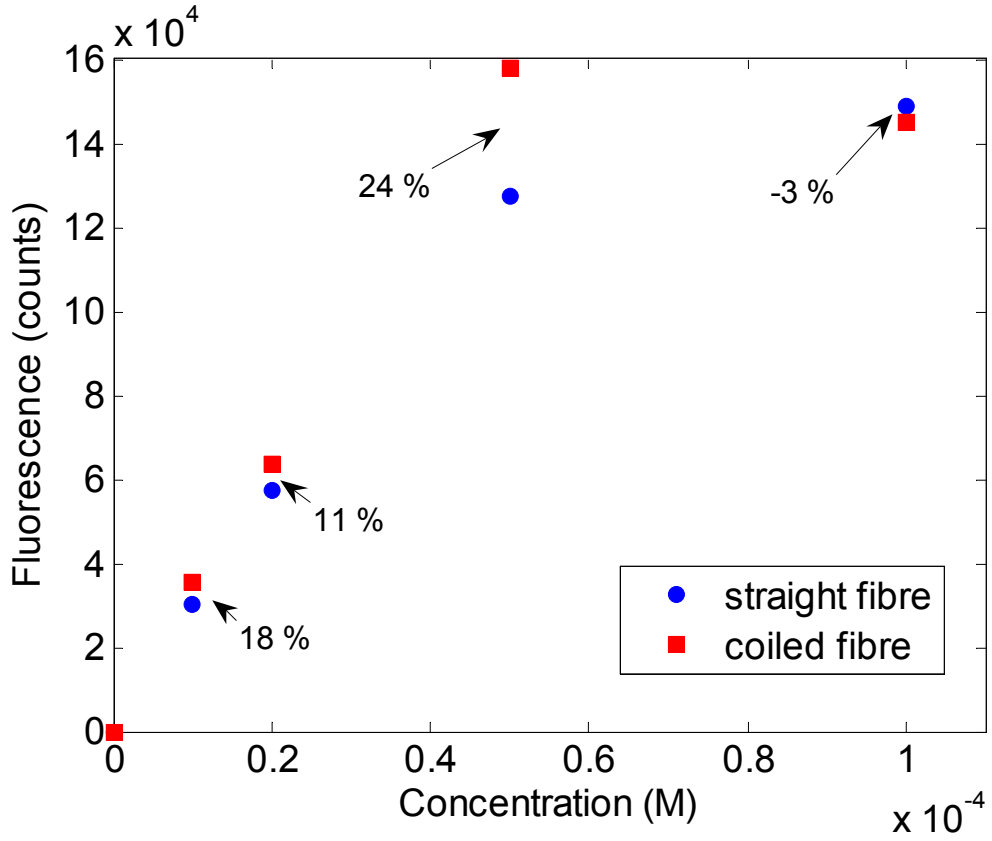

Figure 5.21. Dependence of the optical fibre sensor fluorescence signal on the concentration of the absorbing dye in the cladding area. Estimated error bars are smaller than the symbols.

Figure 5.21 shows the optical fibre sensor fluorescence response as a function of the absorbing dye concentration in the cladding area. For each data point, the time-resolved fluorescence pulse was integrated over the pulse duration and the background signal level measured in pure DMSO/water solution was subtracted. Accumulation time for each measurement was 10 minutes.

The data shows a rather moderate improvement in the fluorescence signal level; the percentage increase is shown in Figure 5.21 for each IR-125 concentration. Note that the fluorescence signal enhancement was uneven over the concentration range, which creates difficulties for signal interpretation. This relatively modest and variable improvement in sensor performance can be understood in terms of the increased losses associated with the transmission of both excitation and fluorescent light through the coiled section of fibre (see Figure 5.20). This interpretation is consistent with the one-way transmission losses observed in Figure 5.19.

From the point of view of distributed measurements, this result suggests that the excitation of higher order fibre modes is an undesirable effect, because the introduced losses reduce the detection range and the improvement in fluorescence capturing efficiency is not significant. However, it should be noted that this study represents an extreme case of higher-order mode excitation, based on a relatively small bending diameter. While it is conceivable that smaller shifts in mode population will lead to a more consistent change in sensitivity, it seems unlikely that this approach will lead to significant overall gains in sensitivity. Therefore further investigation of this issue was not pursued.

5.4 Summary

The results presented in this chapter show the evanescent field interaction with the surrounding environment is strongly dependent on the refractive index of the modified cladding region. This can lead to difficulties due to dispersion in the refractive index, particularly in fluorescence based sensors where the excitation and emission wavelengths are separated. Therefore a broadband supercontinuum light source has been used to characterize the refractive index dependence of the sensor response over a wide wavelength range. The critical effect of the cladding refractive index on the performance of an optical fibre sensor is demonstrated for both amplitude and

wavelength modulated situations. In principle, this approach can be used to predict the performance of the sensor over the full wavelength range of the broadband source.

The theoretical modeling applied to the amplitude and wavelength results as well as to the broadband results demonstrated a satisfactory understanding of the processes occurring in the optical fibre sensing system. Parameters extracted from the modelling gave additional information about the nature of losses in the sensing system. The results suggest that residues from the original cladding of the fibre cause those intrinsic losses, which reduces the sensitivity at low levels of extrinsic absorption. Therefore an important parameter to be addressed in practical sensing applications is the integrity of the interface between the core and the modified cladding.

The results of the investigation of the influence of the mode population on sensor performance suggest that the excitation of higher order fibre modes is an undesirable effect from the point of view of distributed measurements, because the induced losses reduce the detection range and the improvement in fluorescence capturing efficiency is not significant.

The next chapter will use evanescent excitation of a fluorescent indicator in a modified cladding region to explore the application of time-resolved measurements in a quasi-distributed model sensing arrangement.

Chapter 6

Quasi-Distributed Measurements

In this chapter a quasi-distributed optical-fibre sensing system based on pulsed excitation and time-gated photon counting is presented. The system has been designed and used to locate a fluorescent region along the fibre. As discussed in Section 1.4, fluorescence-based distributed systems have undergone relatively little development due to issues with sensitivity, stability, and fluorescence lifetime effects, even though they could potentially be used in a wide range of actual applications.

To overcome the problems of low excitation and coupling efficiency via the evanescent field interaction, an approach based on photon counting has been employed to increase the sensitivity of the detection system. This is analogous to distributed temperature sensors that use photon counting to detect weak anti-Stokes Raman scattering signals. Previous work has shown that this approach can be extremely effective when combined with appropriate background correction procedures (Stoddart et al. 2005).

Another very important sensor characteristic is the spatial resolution of the system. This parameter represents how accurately the detection system can localize the fluorescent region along the fibre length. Spatial resolution is determined by a combination of the lifetime of the fluorophore, the type and length of the fibre system, and the shape of the excitation pulse. Taking these factors into account is critical to interpret the response of the sensor.

In this chapter we present a model that has been developed to characterize this interaction and predict the behaviour of the fluorescent response at the detector. Experimental results are presented that validate the model for two different fluorophores with substantially different lifetimes in a laboratory-scale quasi-distributed arrangement.

The fluorescence from the aluminium complex Alq_3, excited at 405 nm, and from the dye IR-125, excited at 780 nm, was measured at the input end of the fibre by a time-gated detection system. The Alq_3 system, as described in Section 1.3.1, has proven potential application for the detection of corrosion in aluminium alloys.

6.1. Experimental set-up

The "Sentor" optical fibre distributed temperature sensor (DTS) developed by Tyree Optech and Swinburne University was modified during the experimental work presented in this Thesis for use in corrosion detection. The modified experimental arrangement is shown in Figure 6.1. An optical-fibre section of 0.2 m length was declad as described in Section 4.3 and immersed in solutions of either the complex Alq_3 for 405 nm excitation, or the infrared dye IR-125 for 780 nm excitation. To provide effective fluorescence excitation, wavelengths were chosen according to the absorption spectra shown in Section 1.3.1 (Figure 1.2) for the Alq_3 complex and in Section 4.3.2 (Figure 4.12) for IR-125. The Alq_3 complex and the IR-125 dye fluoresce in the 450–600 nm and 800–900 nm regions, respectively.

The declad section was approximately 3 m from the end of an 80 m length of fibre. The extended fibre length was designed to attenuate cladding modes near the excitation source and thus provide stable propagation conditions in the declad section.

The existing DTS was also equipped with new laser sources as follows. The 405 nm laser diode excitation source (OptoTech Ltd, Australia) had pulse widths of between 3 and 5 ns (FWHM) with an approximately Gaussian shape and a repetition frequency of 25 kHz. The 780 nm laser source was developed in house using a Sanyo DL7140-201S laser diode and a PCO-7110 laser diode driver module to provide Gaussian pulses of approximately 4 ns FWHM at the same repetition rate and coupled into an optical fibre. A 50/50 coupler that separated the forward and backward propagating light was custom made for the large core fibre (Diamond SA, Switzerland).

The detection system employed ultrasteep long-pass filters (ZX-000448 from Iridian with a cut-on wavelength of 448 nm and from Omega Optics with a cut-on wavelength of 850 nm) to remove the respective excitation wavelengths, and the photomultiplier tube (PMT, Hamamatsu R928) was operated in the photon-counting mode.

The PMT quantum efficiency varies from 14% at 500 nm to 0.5% at 850 nm. Photon counts were accumulated by the time-gated electronics (Tyree Optech, Australia) in bins of 2 ns width, which corresponds to a length resolution along the fibre of 0.2 m, as defined in Equation 3.2 and assuming a propagation velocity of 2×10^8 m/s. An accumulation time of 10 min was used to obtain adequate signal-to-noise discrimination.

The measurements consist of a number of photon counts corresponding to every bin interval. These were accumulated in computer memory and stored for further interpretation. The resultant bin accumulations can be regarded as waveforms of the fluorescence that originate at a distance along the fibre corresponding to the return time of flight as designated by the bin number. The raw count data was accumulated and stored using the Sentor DTS software (Tyree Optech, Australia), after which it was exported for subsequent processing in standard software (Matlab, Tablecurve, Excel).

As the propagation time through the length of the declad sensor section in the present experiment is of the order of the time resolution, the fluorescence can be regarded as effectively originating from a point source.

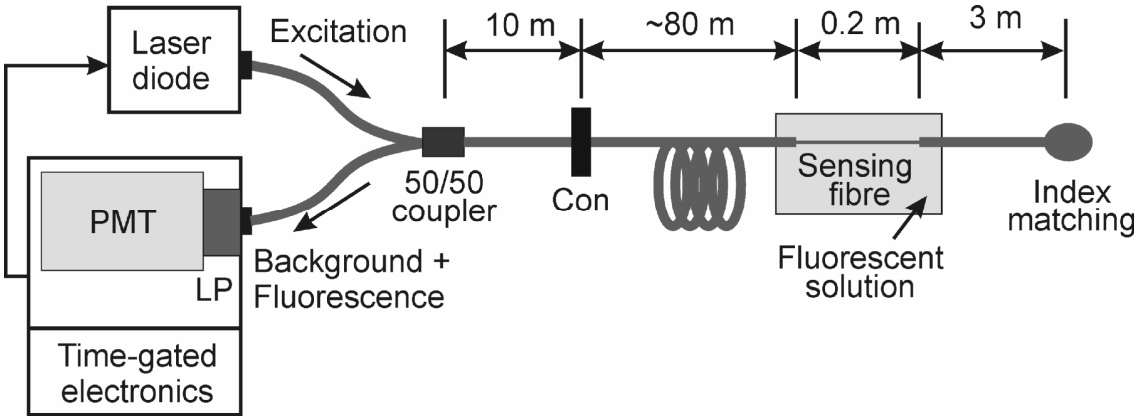

Figure 6.1. Experimental distributed measurements system: LP, long-pass filter; Con, temporary connector.

The Alq_3 complex was prepared by the reaction of aluminium nitrate with 8-hydroquinone (8-HQ) in ethanol solvent. The IR-125 dye was dissolved in a 50/50 mix of DMSO/water solvent chosen to obtain a refractive index close to that of the original cladding (n_{cl} = 1.42). The refractive index of ethanol is lower than the fibre original

cladding, but according to the investigation in Chapter 5 it should not significantly alter the fluorescent signal from the Alq_3.

6.2 Distributed fluorescence waveforms

A typical detected signal is shown in Figure 6.2. This represents the time-domain response of the detection system when the declad fibre section was immersed in a 5×10^{-3} M solution of Alq_3. Reflection peaks from the coupler, connector, and the distal end of the fibre can be clearly identified. These peaks are due to reflections of the pump wavelength that were not sufficiently attenuated by the long-pass filter. The prototype nature of the coupler and connector for this fibre type results in relatively high reflection signals. These could potentially be reduced by employing telecommunication grade couplers and fusion-splicing techniques. Although fusion splicers are commercially available for large core fibres (e.g. 3SAE Technologies, USA; Fujikura, Japan), we are not aware of off-the-shelf suppliers of couplers for this type of fibre.

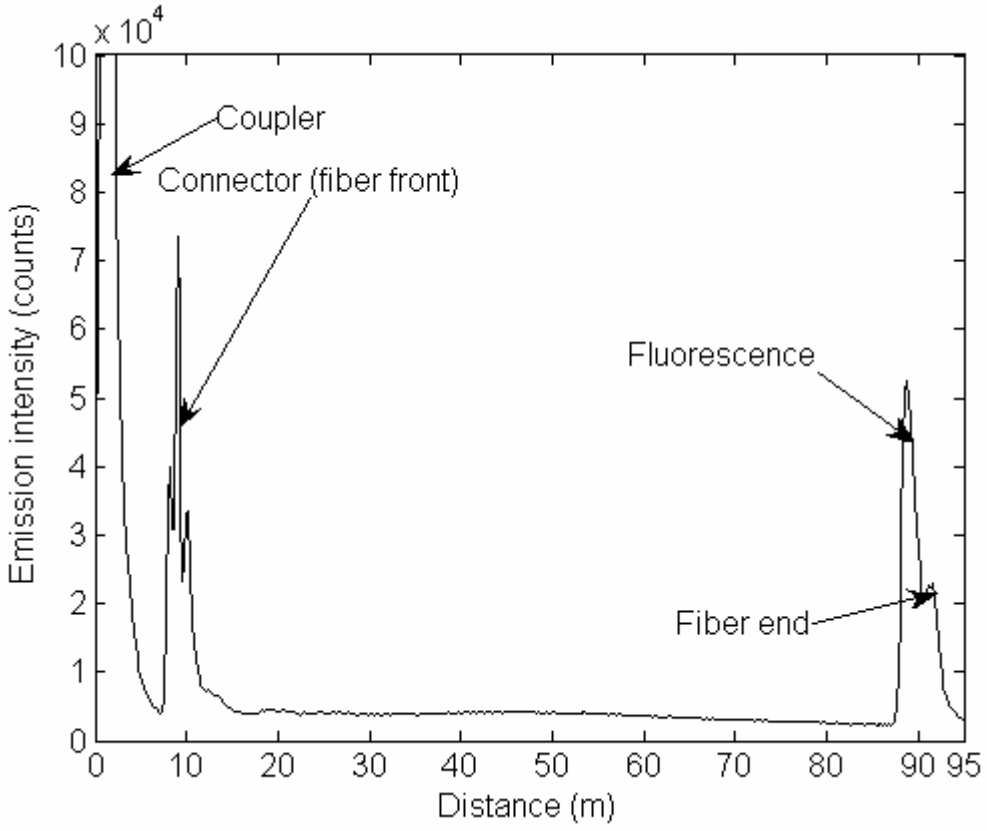

Figure 6.2. Time-resolved response of the distributed sensor, plotted in terms of distance travelled in the optical fibre.

6.3 Effect of fluorescence lifetime on localization

The time-domain response of the detection system when the declad fibre section was immersed into the fluorescence solution is determined by the interaction between the lifetime of the fluorophore and the shape of the excitation pulse, providing that the sensing fibre section is short enough to be considered as a point source. In this case the time-dependence of the fluorescence can be obtained from the solution of the rate equation for a 2-level system excited with a Gaussian shaped pulse. Thus,

$$\dot{n} - \frac{n}{\tau} = kNI_0 \exp\left(-\frac{1}{2}\left(\frac{t-T}{\sigma} \right)^2 \right) \tag{6.1}$$

where n, N give the respective populations of the fluorescing level and the ground state of the 2-level system, k represents the absorption, and I_0 is the exciting pulse amplitude. The Gaussian excitation is centred at time T with width parameter σ and τ is the lifetime of the fluorescing level.

Equation (6.1) has the solution, for $n << N$,

$$n(t) = k\sigma NI_0 \sqrt{\frac{\pi}{2}} \exp\left(\frac{2\sigma^2}{\tau^2} \right) \exp\left(-\frac{t-T}{\sigma} \right) \left[1 + \operatorname{erf}\left(\frac{1}{\sqrt{2}} \left(\frac{t-T}{\sigma} - \frac{\sigma}{\tau} \right) \right) \right] \tag{6.2}$$

The fluorescence intensity is proportional to the population n and can be written

$$I_t(t) = K \exp\left(-\frac{t-T}{\sigma} \right) \left[1 + \operatorname{erf}\left(\frac{1}{\sqrt{2}} \left(\frac{t-T}{\sigma} - \frac{\sigma}{\tau} \right) \right) \right] \tag{6.3}$$

where K is a collection of the time-independent terms and erf is the Error Function.

6.3.1 Alq_3 Fluorescence

The fluorescence waveforms for a range of Alq_3 concentrations are shown in Figure 6.3. The optical time delay due to the 80 m length of fibre preceding the sensor has been removed for clarity. Also shown is the background signal (solid line) from the ethanol solvent. The background signal arises from back-scattered excitation from the sensor section that leaks through the LP filter. The secondary peak which occurs approximately 30 ns after the signal from the declad section coincides with reflection from the end of the fibre.

Subtraction of the background signal results in single-peaked waveforms, a typical example of which is shown in Figure 6.4. The conspicuous trailing edge of these waveforms is indicative of a significant fluorescence lifetime; this is in contrast with the IR-125 results (see Figure 6.7 for the IR-125 fluorescence waveform).

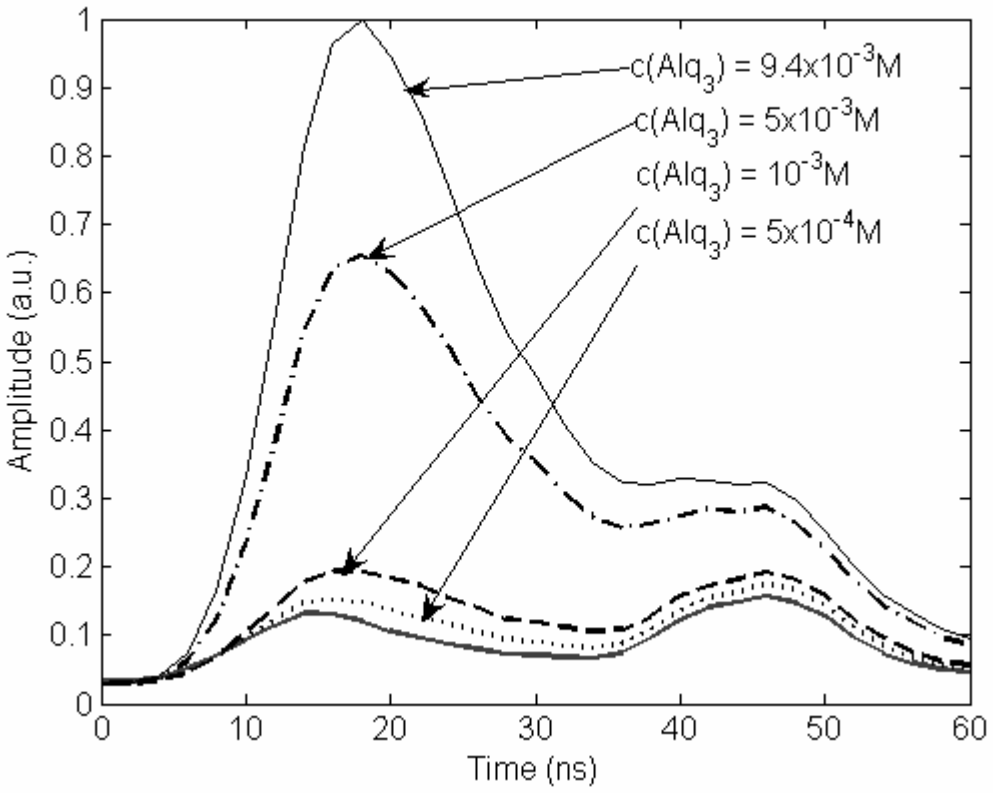

Figure 6.3. Alq3 fluorescence waveforms for a range of concentrations. The solid curve represents the background signal from the ethanol solvent. The waveform for the concentration of 1×10^{-4} M has been excluded for the sake of clarity.

Also included in Figure 6.4 is the model fit using Equation 6.3; the fitted parameters σ, τ and ΔT, which represents a time delay between the maxima of the excitation and fluorescence pulses, are given in Table 6.1 for the concentrations shown. The principles of the fitting procedure, as well as methods of estimating the fitting parameters and errors, are described in Appendix 2. It is apparent from the consistency of the fitted widths σ that the model developed provides a good description of the situation. The fitted values of σ correspond to a FWHM of 9 ns, which is somewhat larger than those expected from the FWHM of the excitation pulse (3-5 ns). This broadening of the measured waveform can be attributed to the effect of the finite bin

width (2 ns) and jitter in the synchronization between the excitation pulse and the bin gates during the 10 min signal accumulation time.

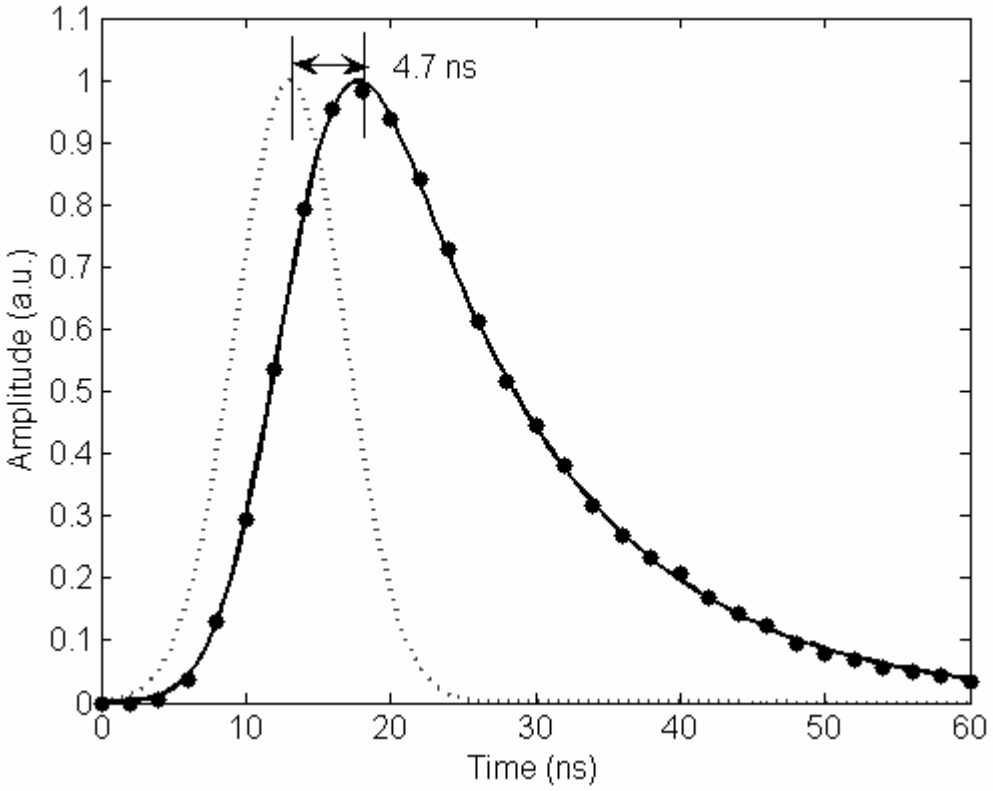

Figure 6.4. Alq_3 fluorescence (9.4×10^{-3} M, circles) after subtraction of the background component due to the ethanol solvent. The model fit from Equation (6.3), (solid curve) is shown together with a reconstruction of the excitation pulse from the fitted parameters (dashed curve). Estimated error bars are smaller than the symbols.

Table 6.1. Fitted model parameters for Alq_3 fluorescence waveforms for the concentrations shown together with the delay of the fluorescence peak from the peak of the reconstructed Gaussian input. The standard errors of the fitted parameters are also shown.

Alq_3 concentration (M)	σ (ns)	τ (ns)	ΔT (ns)
9.4×10^{-3}	3.73±0.04	12.3±0.1	4.70±0.03
5.0×10^{-3}	3.82±0.05	14.0±0.1	5.02±0.23
1.0×10^{-3}	4.11±0.20	17.6±0.6	5.71±0.17
0.5×10^{-3}	4.10±0.30	17.7±1.7	5.71±0.16
0.1×10^{-3}	4.19±0.26	17.9±2.4	5.82±0.23

Also shown in Figure 6.4 is a reconstruction of the Gaussian excitation pulse using the values of σ and ΔT in Table 6.1 for the concentration of 9.4×10^{-3} M. This shows that the peak of the fluorescence waveform is delayed as expected. The distance along the fibre from which the fluorescence originates can be calculated more precisely by correcting for the time delay between the excitation and fluorescence response. For the data shown in Figure 6.4 for example, the delay is 4.7 ns, which is equivalent to 0.47 m in terms of range. Thus the developed model provides a significant improvement in spatial resolution for fluorophores with lifetimes that are longer than the resolution of the sensing system.

The decrease in τ with concentration is indicative of collisional de-excitation of the fluorescence level of the Alq_3 as can be seen in Figure 6.5 where the decay rate is plotted as a function of concentration. Decay rate is the inverse of lifetime and is plotted here to demonstrate the linear dependence on concentration, which is expected for collisional de-excitation (Valeur and Berberan-Santos 2013). The intrinsic lifetime of 18.2 ± 0.9 ns at zero concentration is comparable with the previously observed values of 10.2 - 22.7 ns in different organic solvents (Ravi Kishore et al. 2003).

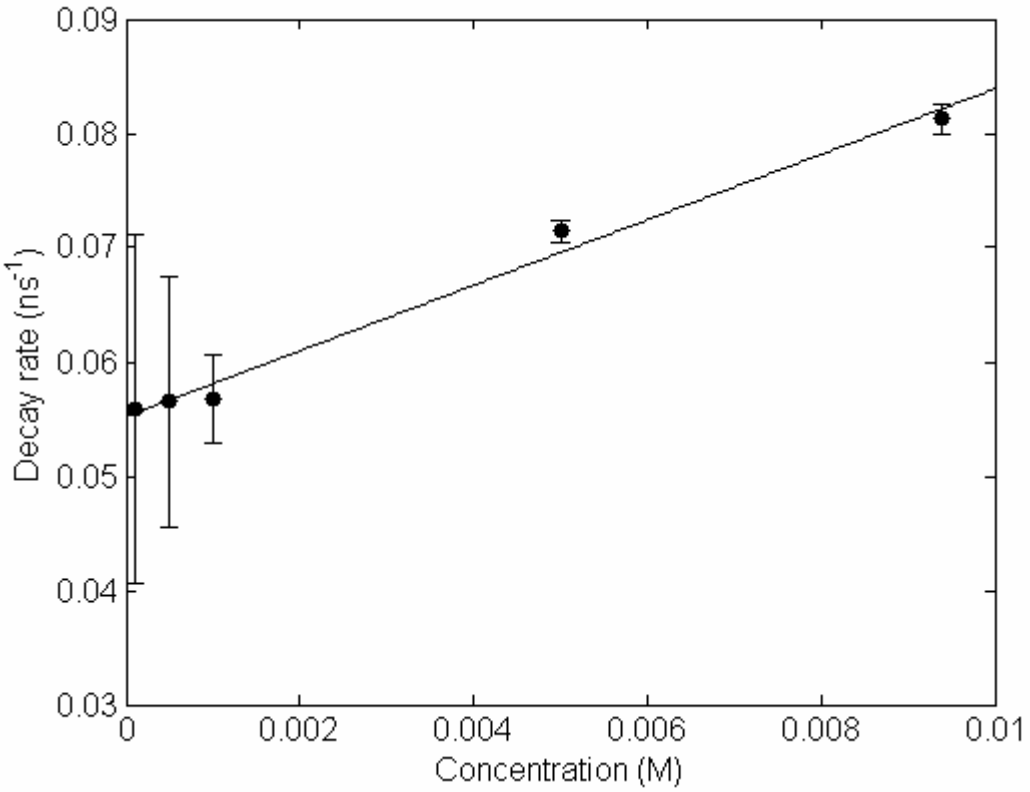

Figure 6.5. Concentration dependence of the Alq_3 fluorescence decay rate. The zero concentration intercept corresponds to an intrinsic lifetime of 18.2 ± 0.9 ns.

The peak fluorescence signal is shown to be proportional to concentration in Figure 6.6 and from this it is estimated that the minimum concentration that can be detected is ~ 5×10^{-5} M or ~ 20 ppm (wt) over an exposed length of 0.2 m. Greater or lesser sensitivities would be expected for greater or lesser lengths of exposed fibre. The sensitivity could also be improved by increasing the laser repetition rate and/or the total accumulation time.

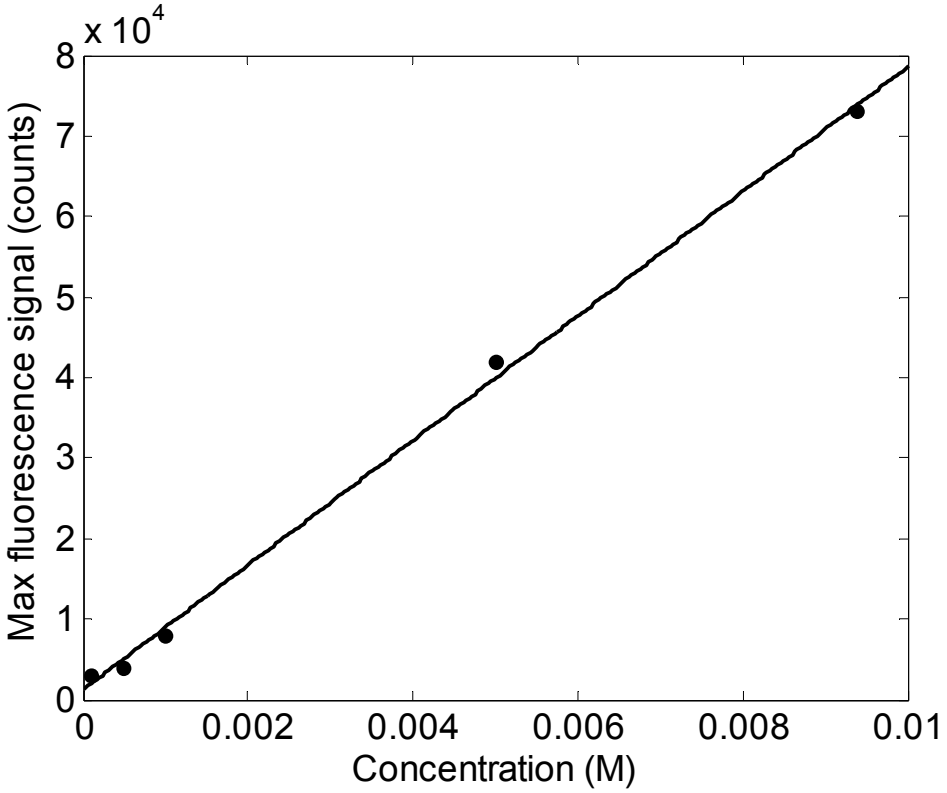

Figure 6.6. Dependence of peak Alq_3 fluorescence on concentration (circles) together with a linear fit. Estimated error bars are smaller than the symbols.

6.3.2 IR-125 Fluorescence

In contrast with Alq_3, the lifetime of fluorescence from IR-125 is known (Lee et al. 2008) to be much smaller than 1 ns, which is shorter than the measurement resolution of this system; hence the fluorescence waveform would not be expected to show a significant trailing edge. A typical waveform is shown in Figure 6.7 where it can be seen that the waveform is roughly symmetrical with little evidence of a significant fluorescent lifetime, τ. However, model fitting using Equation 6.3 gives a time delay of approximately 2.2 ns and τ of 3.7 ns (8.6 ns in terms of FWHM). These parameters could be associated with the instrument response function. The FWHM of 8.6 ns is in reasonable accord with the resolution of 6 ns obtained for distributed temperature sensing with a similar detection system (Stoddart et al. 2005).

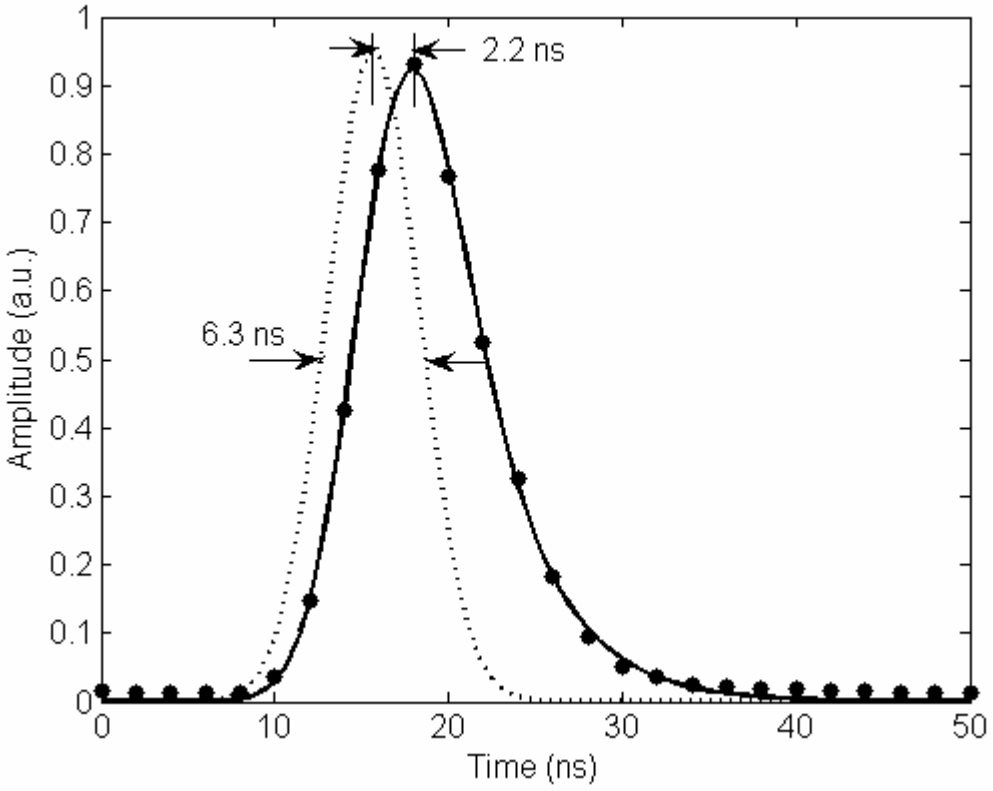

Figure 6.7. Fluorescence waveform for the IR-125 dye at a concentration 5×10^{-5} M (circles) together with the model fit (Equation 6.2). Estimated error bars are smaller than the symbols.

It is interesting to note that the background noise level for IR-125 is much lower than that observed in the wavelength range relevant to the Alq_3. This may be due to the fact that the low-OH silica optical fibre used in this study is not optimized for use with Alq_3 at wavelengths in the UV-violet range. The reduced quantum efficiency of the R928 PMT in the near infrared wavelength range does not appear to play a significant role in this regard. In any event, the background level is sufficiently reduced to allow a detection sensitivity of 2×10^{-6} M (~1.2 ppm) for IR-125. This result suggests that evanescent field excitation of fluorescence can provide a sufficiently sensitive detection mechanism for quasi-distributed chemical sensing, under appropriate conditions.

6.4 Summary

In this chapter, a declad silica-core optical fibre was used to demonstrate the evanescent field detection of fluorescence at a single point in a laboratory-scale quasi-distributed arrangement. With pulsed excitation and time-gated detection, the system has the potential to localize the source of fluorescence along the fibre length. Photon

counting with a sensitive PMT detector allowed the inherent problem of low signal collection efficiency via the evanescent field mechanism to be overcome.

The system was used to investigate two different fluorescent environments with substantially different lifetimes: the complex Alq_3 excited at 405 nm and the infrared dye IR-125, excited at 780 nm. The former environment is potentially relevant to the early detection of aluminium cations produced as a by-product during the early stages of corrosion. The results show that the spatial resolution of the detection system can be limited by the lifetime of the fluorophore. A model has been developed to characterize the behaviour of the fluorescent response at the detector. This model incorporates Gaussian excitation in the signal processing procedure and allows the fluorescence lifetime to be determined. Application of the model to the detected signal allows improvement of the spatial resolution.

In principle, the results of these experiments confirm that evanescent field excitation can be used to detect and localise fluorescence at an arbitrary point along a length of optical fibre. This is a promising result in terms of the aim of this thesis, namely to detect corrosion at an arbitrary location along an optical fibre. While it would also be of interest to demonstrate the simultaneous detection of fluorescence at multiple locations, or even the potential for fully distributed measurements, priority was given to a demonstration of corrosion detection. Other extensions of the work should be considered in future work. A demonstration of corrosion detection is presented in the next chapter.

Chapter 7

Corrosion sensing

This chapter presents a practical demonstration of corrosion detection using the distributed optical-fibre sensing system described in Chapter 6.

Based on past experience, as noted in (McAdam et al. 2005), areas that are prone to corrosion in real metal structures can generally be identified and these locations are seen as the most suitable to install optical fibre corrosion sensors. Particularly attractive sensor locations include at lap joints and under sealant beads.

Therefore to demonstrate the sensor, a model lap-joint was constructed using aluminium 2024 alloy, which is one of the most utilized high strength aluminium alloys. Due to the high strength and excellent fatigue resistance of 2024, it is commonly used on structures and components in the aircraft and transportation industries. It demonstrates good machinability but has limited corrosion resistance.

The optical fibre sensor was mounted in the model lap-joint. It was connected to the distributed sensing unit; after that the model lap-joint with the mounted sensor underwent simulated corrosion testing in a controlled environment. The model that was developed to predict the behaviour of the fluorescence response at the detector was applied to interpret the experimental data. The optical fibre allowed changes in the sensor response to be continuously monitored during the stimulated corrosion test. Hence we obtained a useful tool to investigate the dynamics of the corrosion process.

7.1 Lap joint construction

A lap joint is formed by overlapping two plates and joining them by screws, as shown in Figure 7.1. A gap between the top plates was introduced to allow visual inspection of the sensor if necessary. Channels sized 1×1 mm were cut along the

bottom plates to accommodate the optical fibre sensor. Two of the sections shown in Figure 7.1 were connected together and an extra aluminium sheet was added underneath to connect the structure. The aluminium sections were not treated with any corrosion protection techniques such as painting, coating, etc.

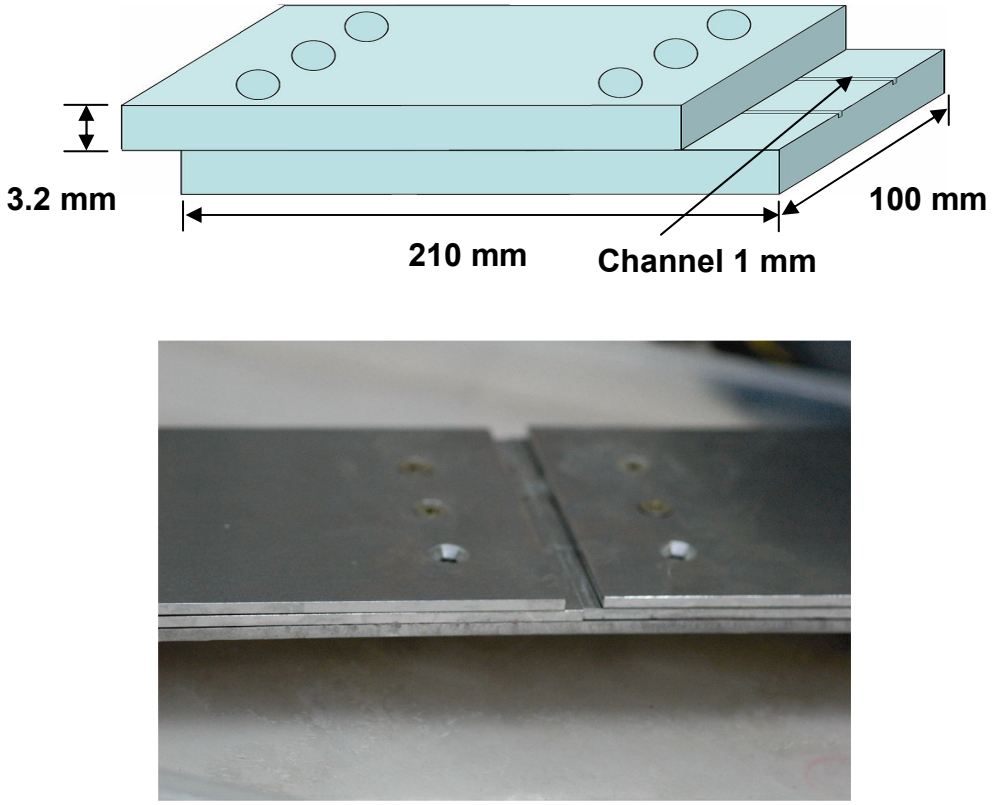

Figure 7.1. Drawing and image of the model lap joint.

7.2 Fluorescent sensor composition

The 8-HQ was used as a fluorescent indicator to show the presence of aluminium ions in the examined location. As discussed in Chapter 1, aluminium ions provide an early indication of corrosion occurring in the aluminium alloy placed in the corrosion environment. It has been demonstrated that the optical fibre sensing system can detect fluorescence from the complex of Al^{3+} ions and the 8-HQ fluorescent dye. However to produce a working optical fibre sensor, a polymer is required to provide a solid support for the indicator dye (8-HQ) together with permeation of the species of interest.

A supporting polymer was synthesized using the copolymer polyethylene glycol (3-PEG) as a precipitant together with a crosslinker (Tolonate) in the presence of an amine catalyst. Tolonate is used in synthetic polymer chemistry as a crosslinker of one-

pack heat-activated coatings (as the only crosslinker or in conjunction with aminoresins).

After stripping as described in Section 4.3.1, an optical fibre sensing section was positioned in the model lap-joint channel and covered with the polymer synthesis components mixed together. The open channel lap-joint was allowed to cure in an oven at 50 ºC for 3 days. To activate the synthesised polymer with the 8-HQ dye, the model lap joint channel with optical fibre sensor surrounded by the polymer was treated with 1% 8-HQ in 99% Ethanol for approximately 30 minutes. After that the parts of the lap joint were joined together and fastened up.

The polymer condition at the lap joint was visually inspected during the curing process. Changes in the polymer colour were observed after curing and activating the polymer with 8-HQ (see Figure 7.2). Whereas the 8-HQ in 3-PEG is a colourless solution, application and activation on the lap joint resulted in the polymer changing to an opaque white colour. This indicates that there were some amount of metal ions dissolved in the polymer which created a complex with the 8-HQ. The three day curing process at an elevated temperature with moisture present in the uncured polymer may cause degradation in the unprotected aluminium material, thereby producing Al^{3+} ions.

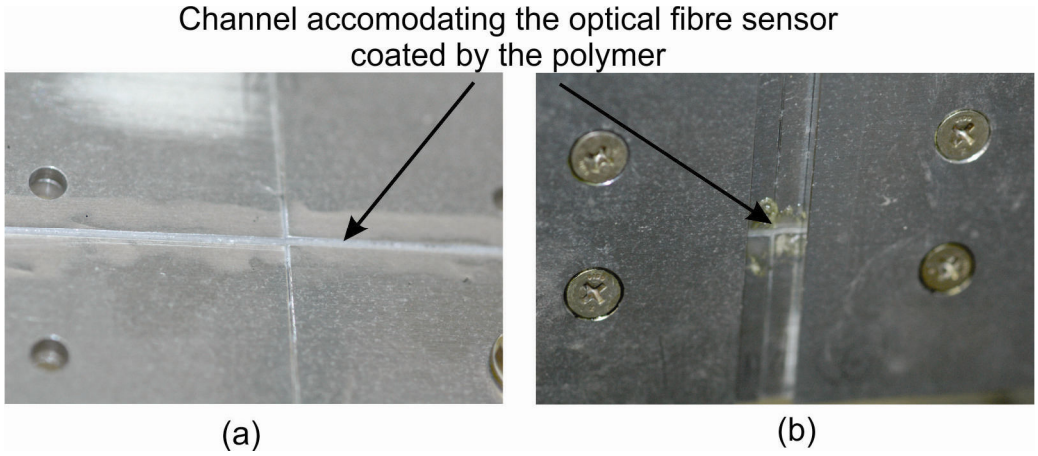

Figure 7.2. Polymer in the model lap-joint: (a) - before 8-HQ activation, (b) - after the polymer was activated by 1 % 8-HQ solution in 99 % ethanol with the top plates in position.

7.3 Salt spray chamber

Corrosion simulation was performed in a 450 l Ascott Salt Spray Chamber (Ascott Analytical Equipment). The chamber creates a controlled corrosive environment in which the corrosion behaviour of the samples can be investigated. In the salt spray chamber, compressed air is delivered via the air saturator and mixed with salt water, which is delivered via the salt solution pump and flowmeter. This creates a finely divided salt spray (also called 'salt mist' or 'salt fog') that is oxygen rich and highly corrosive. The salt spray goes through an atomizer into the chamber atmosphere, where it then falls out onto the objects under the test.

The corrosion simulation was performed according to the American Society of Testing and Materials (ASTM) test B117. This continuous salt spray test specification is used to test the relative corrosion resistance of coated and uncoated metallic specimens, when exposed to a salt spray climate at an elevated temperature. Test specimens are placed in an enclosed chamber and exposed to a continuous indirect spray of neutral (pH 6.5 to 7.2) salt water solution, which is deposited on to the specimens at a rate of 1.0 to 2.0 ml/80 cm²/hour, in a chamber temperature of +35 °C. This climate was maintained under constant steady state conditions by programming the apparatus of the Ascott Salt Spray Chamber.

Salt fog testing was performed by placing the model lap joint in the test cabinet; the lap joint was placed at an approximately 15° angle from vertical (as shown in Figure 7.3) to allow the condensation to run down the specimen and to minimize condensation pooling.

Figure 7.3. Model lap-joint with incorporated optical fibre sensor in the salt spray chamber.

The connecterized optical fibre input and output pigtails were fixed outside the salt spray chamber allowing continuous monitoring of the sensor response without interrupting the corrosion simulation. The corrosion test was run for 50 hours; after that the model lap-joint was inspected visually for qualitative signs of corrosion development.

7.4 Results

The distributed optical fibre sensing system employing photon counting provides high sensitivity, but at the same time it is not highly wavelength selective. To prove that the distributed optical-fibre sensing system was registering the Alq_3 fluorescence, optical spectra were recorded before the corrosion test started and after it had been running for 24 hours. The emission from a 390 nm Ocean Optics LED source was launched into the optical fibre sensor to excite fluorescence in the model lap joint before it was placed in the salt spray chamber. To measure the spectrum of the fluorescence emission the optical fibre sensor output was connected to an Ocean Optics S2000 Spectrometer. The 390 nm Ocean Optics LED source was used for convenience to excite the fluorescence instead of the 405 nm laser diode, due to the availability of equipment in the experiment location.

The recorded spectra are shown in Figure 7.4. Even without treatment in the salt chamber, the 440-650 nm fluorescence emission band is present, as would be expected for the Alq_3 complex. This indicates the presence of an initial aluminium ion concentration, as was suggested in Section 7.2. A rise in the fluorescence signal was observed after corrosion simulation for 24 hours, but it was accompanied by a rise in the level of the transmission at shorter wavelengths (less than 450 nm). This combination of excitation and fluorescence wavelengths, integrated over the length of the fibre, makes it difficult to interpret the data unambiguously.

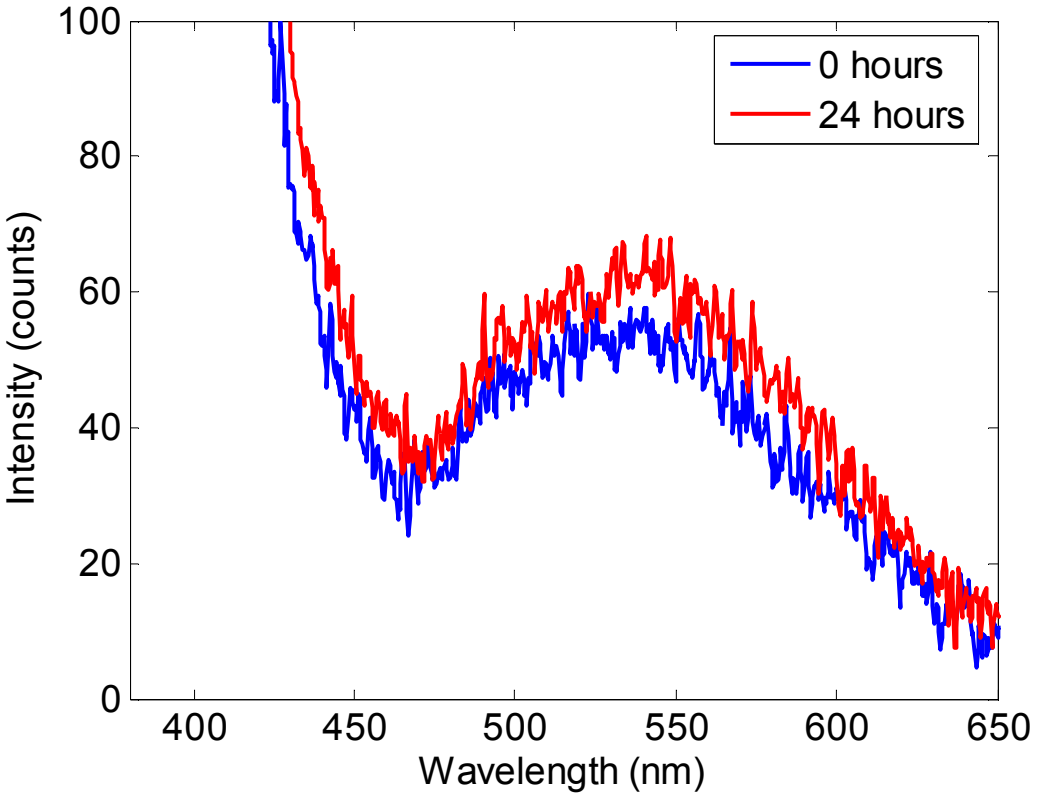

Figure 7.4. Fluorescence spectra from the optical fibre sensor in the model lap joint before exposure to the salt spray chamber and after 24 hours exposure.

The distributed optical-fibre sensing system described in Chapter 6 was employed to investigate corrosion development in the model lap joint in more detail. A series of readings representing the time domain response of the detection system was recorded at different times during the corrosion simulation test. Figure 7.5 shows the measurement obtained after the model lap joint had been in the salt spray chamber for 30 hours.

Reflection peaks from the coupler, connector, as well as the fluorescence peak from the sensor can be clearly identified. The accumulation time for each reading was 10 min.

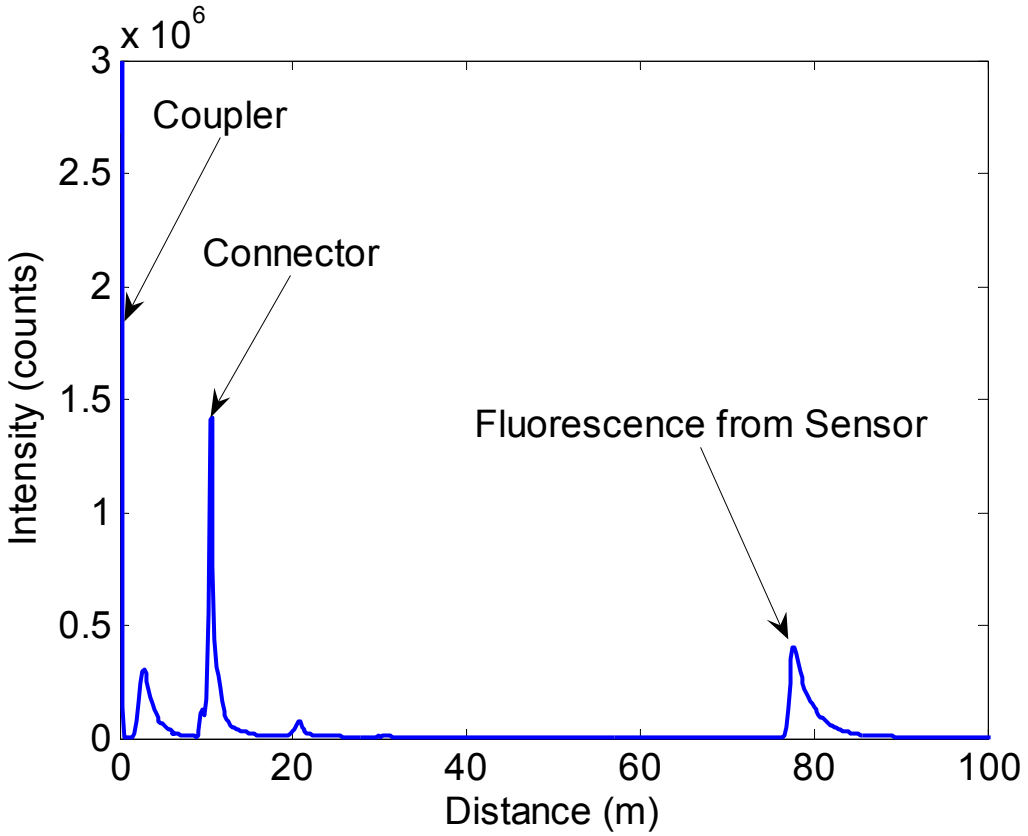

Figure 7.5. Time-resolved response of the distributed sensor during simulated corrosion testing, plotted in terms of position in the optical fibre. The fluorescence peak corresponds to the response of the optical fibre sensor embedded in the model lap joint after 30 hours of testing.

The time dependence of the fluorescence intensity from the optical fibre sensor in the model lap joint is shown in Figure 7.6. Every point represents the fluorescence intensity integrated over the duration of the fluorescence waveform. The fluorescent signal increased rapidly during the first part of the experiment and peaked after about 14 hours. From that point the signal saturated and stayed approximately the same until the end of the experiment. Unfortunately the data in the period from 5 to 14 hours was incomplete due to technical issues. A subsequent failure of the control computer made it impossible to repeat the experiment within the time available.

The fluorescent signal level is related to the concentration of aluminium ions and therefore characterises the development of the corrosion process in the model lap joint, particularly in the channel in close proximity to the optical fibre sensor. It is clear that

the sensing system was able to detect the corrosion process from an early stage. Recording the signal profiles more frequently would provide additional information about the corrosion process in the transition period from 5 to 15 hours of the experiment. The results shown here suggest that the sensor could be used to develop a better understanding of the progression of the corrosion process in future work, assuming that more frequent signal recording is possible.

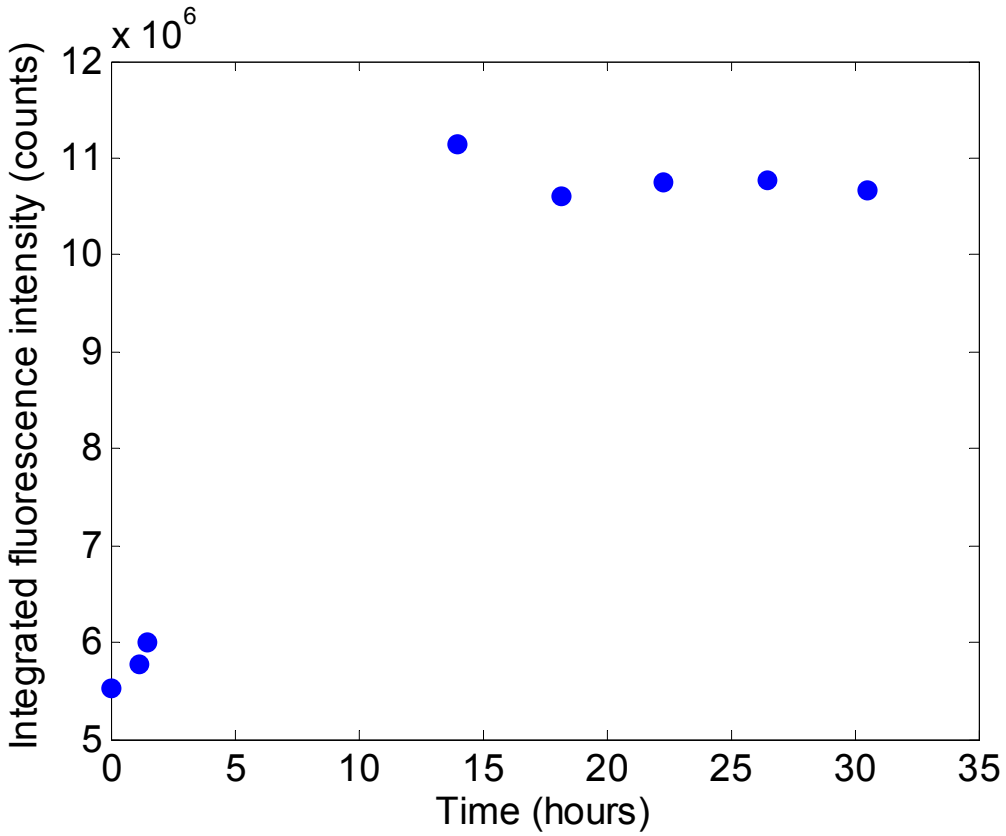

Figure 7.6. Time dependence of the fluorescence sensor response over the duration of the corrosion test. The fluorescence intensity has been integrated over the duration of the waveform in the sensor region. Estimated error bars are smaller than the symbols.

The distributed detection system records fluorescence waveforms which contain additional information about internal processes occurring in the sensor environment. Examples of the waveforms are shown in Figure 7.7 for the initial stage before the corrosion test and after 30 hours of the corrosion simulation testing. The difference between the trailing edges of these waveforms indicates a significant change in the fluorescence lifetime over the course of the experiment.

The recorded waveforms were fitted using Equation 6.2 with the resulting curves also shown in Figure 7.7. The fluorescence lifetimes (τ) were extracted from the waveform data for each measurement and are shown in Table 7.1.

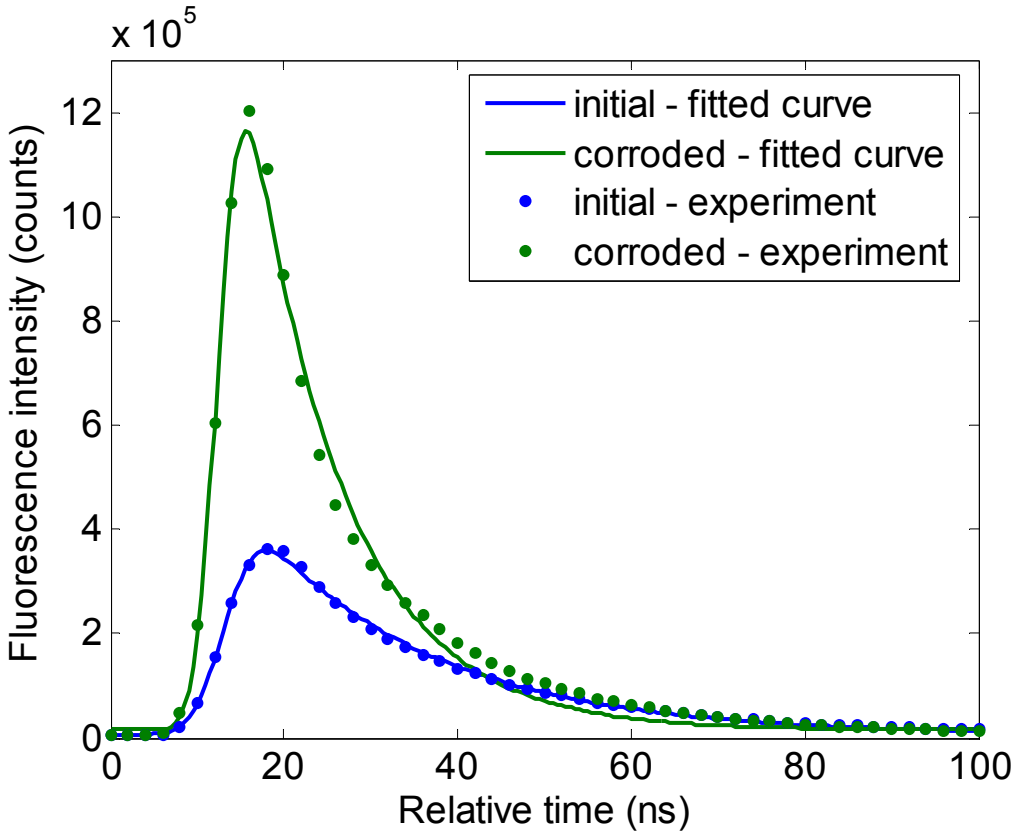

Figure 7.7. Alq_3 fluorescence waveforms recorded before the test and after 30 hours of corrosion simulation testing. Estimated error bars are smaller than the symbols.

A significant decrease in the fluorescence lifetime is indicative of collisional de-excitation of the fluorescence level of the Alq_3. Typically it is associated with a rise in the concentration of the fluorescent molecules, as seen in Section 6.3.1 for Alq_3 dissolved in ethanol. However, the Alq_3 fluorescence lifetime is known to depend on a number of factors, including whether it is dissolved in a solvent, used as a solid film or incorporated in a polymer matrix (Ravi Kishore et al. 2003).

Table 7.1. The extracted fluorescence lifetimes (τ).

Corrosion simulation test duration (hours)	τ (ns)
0	20.6±0.2

1.2	20.5±0.2
1.5	20.4±0.2
14.0	12.0±0.3
18.2	13.0±0.5
22.3	11.0±0.3
26.5	11.0±0.3
30.5	11.0±0.3

Indeed, the fluorescence lifetimes obtained in the initial stage of the corrosion experiment (up to 1.5 hours) were larger than the lifetime observed for the lowest concentration of Alq_3 in ethanol in Section 6.3.1. Similarly, the lifetimes in the later stage of the corrosion experiment are significantly lower than those observed for the saturation concentration of Alq_3 in ethanol (9.7×10^{-3} mol/l). This confirms that the precise relationship between fluorescence lifetime and concentration for Alq_3 is dependent on the particular matrix used. Nevertheless, the overall trend indicates that the concentration of aluminium ions rose with the progression of the corrosion, causing an increase in the Alq_3 concentration and consequently in the fluorescence signal. This continued until the Alq_3 concentration reached a saturation point where the polymer matrix doped with 8-HQ could not take up any more aluminium ions.

After the simulated corrosion experiment was terminated, the lap joint was visually inspected and a significant level of corrosion was observed (Figure 7.8).

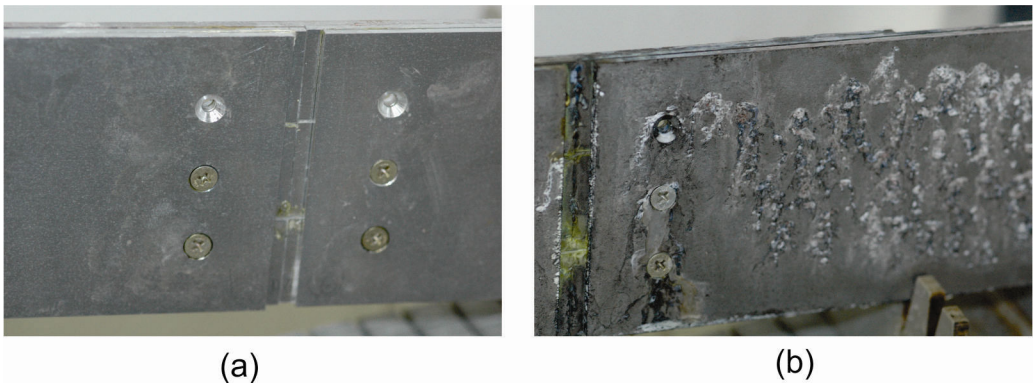

Figure 7.8. The model lap-joint shown (a) before the corrosion test and (b) after the corrosion test was terminated.

7.5 Summary

The sensing system demonstrated an ability to perform *in situ* detection of corrosion in a model aluminium lap-joint. The optical fibre sensor was installed in the lap-joint, representing a predetermined position that is vulnerable to corrosion. The sensing system was able to detect the occurrence of corrosion in the model lap-joint, as well as locating the corrosion point along the sensing fibre. The results also indicated some initial corrosion in the unprotected aluminium during the polymer curing process. This effect would not be acceptable in practical applications. Therefore future work should aim to avoid this effect by applying a protective coating before installing the dye with 3-PEG polymer.

The experimental data was interpreted by means of the Gaussian excitation model. The model gives an opportunity to extract the fluorescence lifetime from the experimental data. Knowing the fluorescence lifetime provides additional information about corrosion development at different stages during the test.

Chapter 8

Conclusion and Further Work

8.1 Summary of the Project

The problem of optical fibre corrosion detection is still current despite considerable efforts during the past few decades. The literature search presented here has shown that, despite some technical improvements, the basic principles and achievements have remained much the same for the past few years and the problem of optical fibre corrosion detection is far from resolved. In general, recent reviews (Yin et al. 2008, Norris 2000) suggest that fluorescence-based techniques remain attractive due to their exceptional selectivity and the large amount of previous research and development that can be drawn upon.

The theoretical and experimental studies presented here resulted in the development of a system that could perform distributed detection of fluorescent light coupled into optical fibre guided modes. Theoretical models were developed to investigate and improve the efficiency of the optical fibre detection system. The theoretical models allowed the spatial resolution of the sensor to be improved, while also confirming a sound understanding of the physics underlying the sensor. This understanding in turn helps to gain insight into the processes giving rise to the fluorescence signal and will underpin future efforts to analyse the data from fully distributed sensing arrangements. The developed detection system was successfully tested in a practical application. It was able to detect the development of corrosion at an early stage in a predetermined site placed at an arbitrary location along the optical fibre.

Initial work was carried out to evaluate the most promising potential solutions, including the detection of water diffusion into a fibre and sensing via the evanescent field. Firstly a novel detection method based on the measurement of water ingress into

conventional optical fibre during the corrosion process was tested. The approach was based on changes in the water peak absorption in a sensor made from conventional optical fibre, but it did provide promising results. This method may be attractive for sensor designs based on hygroscopic glasses or fibres with small cladding thickness that allow faster diffusion rates.

Two constructions of an evanescent field-based optical fibre sensor were examined as sensing elements for distributed measurements: etched D-shaped fibre and declad plastic clad fibre. Work was carried out to establish a technique for creating an optical fibre sensor using commercially available D-shaped fibre. The optical fibre sensor based on etched D-fibre was difficult to construct due to problems with controlling the etching process and, for this reason, it was found unsatisfactory.

As a result of these preliminary investigations, an approach based on the detection of fluorescence excited through the evanescent field in an exposed core optical fibre sensor was selected for further study. This approach has the potential for fully distributed measurements of arbitrary chemical concentration along an optical fibre. Theoretical modelling confirmed the feasibility of using the proposed photon counting system to detect fluorescence excited by the evanescent field surrounding a conventional multi-mode fibre with a modified cladding. The modelling suggested that under ideal conditions sub part per million sensitivity can be achieved over distances of more than a kilometre, which is sufficient for practical application in corrosion monitoring.

Large core multimode plastic clad fibre with the cladding chemically removed was evaluated in the IR and blue spectral regions. It was shown using that fluorescence could be coupled into the guided modes of the fibre and detected. A theoretical model describing the absorption and fluorescence response of the large core multimode plastic clad fibre sensor was developed. The model was based on a geometrical optics approach which incorporates the effects of the input intensity distribution. This provided a basis to investigate the processes occurring in the optical fibre sensing system, including the effects of cladding refractive index, dispersion and modal distribution. The theoretical model was justified by an experiment providing a change in the sensor working conditions such as the cladding refractive index. The effects of absorption and fluorescence were experimentally investigated by measuring the absorption and

fluorescence detection efficiency for an infrared fluorescent organic dye (IR-125). The obtained experimental data were fitted with the model expressions showing an excellent agreement between the predicted and experimental data.

In terms of practical output, these results demonstrate that the sensor is relatively insensitive to changes in the absorber concentration below about 1.415 refractive index units. However, the relatively small losses shown here might become significant for longer exposed regions in a practical distributed sensing arrangement. At the same time the absorption and fluorescence dependences are strongest in the RI range from 1.43-1.45 as it was expected from the calculated curves. Consequently, the detection sensitivity can be significantly improved by careful choice of refractive index in the cladding region. However, the transmission measurements show that at the same time absorption losses rise significantly as well. In the case of distributed measurements, this improvement in sensitivity will come at the cost of reduced detection range.

The large core optical fibre sensor behaviour within the broad wavelength range of excitation was evaluated experimentally. It was shown that dispersion effects in the core and cladding materials of the large core multimode optical fibre sensor can complicate measurement interpretation when wavelength modulated measurements are performed, or in situations where multiple wavelengths are of interest for amplitude modulated schemes.

In addition, the effect of launching conditions on the sensor performance were investigated. The higher order modes were excited in the optical fibre at the point before the sensor by coiling the fibre section. Sensitivity of absorption and fluorescence detection was evaluated. Coiling the fibre before the sensor results in more than a twofold increase in the absorption sensitivity, which can be attributed to the excitation of higher order modes with strong evanescent field coupling. At the same time, a rather moderate improvement in the fluorescence signal level was attained. Moreover, the fluorescence signal enhancement was uneven over the concentration range, which can create difficulties for signal interpretation. From the point of view of distributed measurement, this result suggests that the excitation of higher order fibre modes is an undesirable effect, because the introduced losses reduce the detection range and the improvement in fluorescence capturing efficiency is not significant.

The use of a declad silica-core optical fibre for the evanescent field detection of fluorescence has been demonstrated in a distributed sensing system. With pulsed excitation and time-gated detection, the system has the potential to localize the source of fluorescence along the fibre length. Photon counting with a sensitive PMT detector allowed the inherent problem of low signal collection efficiency via the evanescent field mechanism to be overcome.

The system was used to examine two different fluorescent environments: the complex Alq_3 excited at 405 nm and the infrared dye IR-125, excited at 780 nm. The former environment is potentially relevant to the early detection of aluminium cations produced as a by-product during the early stages of corrosion. Although the experiments were conducted on a laboratory-scale in a quasi-distributed arrangement, the results would be applicable to a fully distributed system, where the complete fibre length was clad with sensitive material. The results show that the spatial resolution of the detection system can be limited by the lifetime of the fluorophore. Analysis of the fluorescence waveforms confirmed that the use of a model incorporating Gaussian excitation in the signal processing procedure could significantly improve the spatial resolution.

The model also allows the fluorescence lifetime to be determined, with the results obtained showing good agreement with published data. It is estimated that the minimum concentration of Alq_3 that can be detected under these experimental conditions is $\sim 5\times10^{-5}$ M or ~ 20 ppm (wt) over an exposed length of 0.2 m. The detection limit for IR-125 was found to be 2×10^{-6} M (~1.2 ppm). Given the relatively small total number of molecules that fall within the range of the evanescent field and contribute to the fluorescent signal, these results suggest that the evanescent field excitation mechanism can provide sensitive detection of chemical distributions. Greater or lesser sensitivities would be expected for greater or lesser lengths of exposed fibre.

The distributed optical-fibre sensing system was used to monitor corrosion in a model aluminium lap-joint. The sensing system demonstrated an ability to perform *in situ* detection of corrosion under practical conditions. The experimental data was interpreted by means of the Gaussian excitation model, which provided the fluorescence lifetime. This delivers additional information about corrosion development at different stages during the test. Employing the optical fibre sensor gave an opportunity to continuously monitor changes in the sensor response during the stimulated corrosion

test. Hence it provides a useful tool to investigate the dynamic evolution of the corrosion process.

8.2 Research Outlook

This study has shown that an approach based on distributed measurements of fluorescence excited through the evanescent field in an optical fibre sensor has great potential for corrosion detection. In principle it can be applied to hidden areas at an early stage of the corrosion process.

However an optimal optical fibre sensor construction remains the main challenge. It has been found that a significant level of background most likely related to imperfections at the core-cladding interface can limit the sensitivity of the fibre sensor. Therefore effective protection of the optical fibre sensing element from the environment is a significant problem. This problem is strongly related to the development of a suitable polymer carrier for the sensing dye to be employed as a sensing cladding in the optical fibre sensor construction. If the current polymer carrier is used in future development of the corrosion sensing application, care should be taken to prevent the carrier from initiating corrosion during installation of the sensor.

Investigation of the effect of immobilizing the 8-HQ indicator in a cladding material is an interesting perspective as this could lead to changes in the Alq_3 fluorescence lifetime and therefore affect the spatial resolution of the detection system. While further development is required to address the requirements of the modified cladding, mode distribution effects can be addressed with an appropriate background correction procedure, provided that the application allows a stable mode distribution to be maintained.

Future work could also seek to evaluate other fibre core designs for sensitivity to variations in cladding refractive index. For example, a structure that achieves high sensitivity to sample concentration with reduced sensitivity to refractive index changes would be attractive for a range of distributed sensing applications.

The results show that an intense broadband light source can be used to obtain a large body of data relating to the overall system performance. Although the results presented here rely on an estimated form of the dispersion curve for the DMSO/ethanol

mixtures, it is expected that the dispersion curves can be obtained more directly by quantitative analysis of the normalized transmission curves. This may establish the technique as a convenient way to measure the dispersion of arbitrary fluids and could be addressed in future work.

Another interesting direction follows from the fact that fluorescent probes are generally sensitive to multiple analytes or parameters e.g. temperature and pH that can interfere with the fluorescence response. One solution to this problem might be to build some redundancy into the system by including multiple fluorescence probes. For example, assuming that the materials issues can be resolved, an ability to simultaneously measure metal ions and pH would be attractive.

Finally, future work should aim to investigate the potential for measurements of continuously distributed chemical concentrations along the length of the fibre. In principle it is understood that an iterative technique will be required to disentangle the "shadowing" effect, where the absorption due to target compounds near the start of the fibre will reduce the pump power transmitted to locations further down the fibre. Despite this understanding, there have been limited reports of studies that have explored this situation with evanescent excitation of fluorescence.

References

Afshar, S. V., Warren-Smith, S. C. and Monro, T. M. (2007) 'Enhancement of fluorescence-based sensing using microstructured optical fibres', *Optics Express,* 15(26), 17891-17901.

Agnihotri, N. K., Singh, H. B., Sharma, R. L. and Singh, V. K. (1993) 'Simultaneous determination of beryllium and aluminium in mixtures using derivative spectrophotometry ', *Talanta,* 40(3), 415-423

Ahmad, M. and Narayanaswamy, R. (2002) 'Optical fibre Al(III) sensor based on solid surface fluorescence measurement', *Sensors and Actuators B: Chemical,* 81(2-3), 259-266.

Alieva, R. A., Alieva, F. S. and Chyragov, F. M. (2006) 'Bis-(2,3,4-Trihydroxyphenylazo)benzidine as a reagent for the photometric determination of aluminum', *Journal of Analytical Chemistry,* 61(7), 630-633.

Amelin, V. G. and Gan'kova, O. B. (2007) 'Test determination of aluminum, beryllium, and cationic surfactants using phenolcarboxylic acids of the triphenylmethane series immobilized on cloths from synthetic and natural fibers', *Journal of Analytical Chemistry,* 62(3), 285-290.

Anderson, G. P., Golden, J. P., Cao, L. K., Wijesuriya, D., Shriver-Lake, L. C. and Ligler, F. S. (1994) 'Development of an evanescent wave fiber optic biosensor', *IEEE Engineering in Medicine and Biology Magazine,* 13(3), 358-363.

Arregui, F. J., Otano, M., Fernandez-Valdivielso, C., Matias, I.R. (2002) 'An experimental study about the utilization of Liquicoat® solutions for the fabrication of pH optical fiber sensors', *Sensors and Actuators B: Chemical,* 87(2), 289-295.

Badr, I. H. A., Johnson, R. D., Diaz, M., Hawthorne, M. F. and Bachas, L. G. (2000) 'A selective optical sensor based on [9]mercuracarborand-3, a new type of ionophore with a chloride complexing cavity', *Analytical Chemistry,* 72(18), 4249-4254.

Bariain, C., Matias, I. R., Arregui, F. J. and Lopez-Amo, M. (2000) 'Optical fiber humidity sensor based on a tapered fiber coated with agarose gel', *Sensors and Actuators B: Chemical,* 69(1-2), 127-131.

Berger, S. and Tomozawa, M. (2003) 'Water diffusion into a silica glass optical fiber ', *Journal of Non-Crystalline Solids,* 324(3), 256-263.

Block, J. and Morgan, E. (1962) 'Determination of parts per billion iron by fluorescence extinction', *Analytical Chemistry,* 34 (12), 1647-1650.

Born, M. and Wolf, E. (1999) '2.3 The Lorentz-Lorenz formula and elementary dispersion theory' in *Principles of Optics: Electromagnetic Theory of Propagation, Interference and Diffraction of Light*, 7 ed., Cambridge: University Press, 89-103.

Börner, S., Orghici, R., Waldvogel, S. R., Willer, U. and Schade, W. (2009) 'Evanescent field sensors and the implementation of waveguiding nanostructures', *Applied Optics,* 48(4), B183-B189.

Bossi, R. H., Criwell, T., Ikegami, R., Nelson, J., Normand, E., Rutherford, P. S. and Shrader, J. (1995) 'Novel methods for aicraft corrosion monitoring', *Proceeding of SPIE,* 2455, 70-81.

Browne, C. A., Tarrant, D. H., Olteanu, M. S., Mullens, J. W. and Chronister, E. L. (1996) 'Intrinsic sol−gel clad fiber-optic sensors with time-resolved detection', *Analytical Chemistry,* 68 (14), 2289-2295.

Buerck, J., Sensfelder, E. and Ache, H.-J. (1996) 'Distributed measurement of chemicals using fiber optic evanescent wave sensing', *Proceeding of SPIE,* 2836, 250-260.

C.U. Wetlesen and Omang, S. H. (1961) 'Spectrophotometric determination of aluminium with stilbazo', *Analytica Chimica Acta,* 24, 294-297.

Campa, M. R. F. d. l., García, M. E. D. and Sanz-Medel, A. (1988) 'Room-temperature liquid phosphorimetry of the aluminium-ferron chelate in micellar media : Determination of aluminium', *Analytica Chimica Acta,* 212, 235-243.

Chandani, S. M. and Jaeger, N. A. F. (2005) 'Fiber-optic temperature sensor using evanescent fields in D Fibers', *IEEE Photonics Technology Letters,* 17(12), 2706-2708.

Chandani, S. M. and Jaeger, N. A. F. (2007) 'Optical fiber-based liquid level sensor', *Optical Engineering,* 46(11), 114401 (7 pages).

Chang, K. (2005) 'The importance of minimizing hydrogen aging lossses and alkali impurities OFS AllWave Zero Water Peak (ZWP) Fiber', *OFS white papers*, available online: www.ofsoptics.com.

Chang, X., Wang, S., Haiqing, L. and Gong, G. (2003) 'Study on fluorescence characteristic of quercetin–nanoporous anodic aluminum oxide composites', *Journal of Fluorescence,* 13 (5), 421-425.

Chen, X., Zhou, K., Zhang, L. and Bennion, I. (2005) 'Optical chemsensors utilizing long-period fiber gratings UV-inscribed in D-fiber with enhanced sensitivity through cladding etching', *IEEE Photonics Technology Letters,* 16(5), 1352-1354.

Chin, R., Hallidy, W., Cruce, C., Salazar, N., Keith, J., Patonay Gabor, S., Lucjan and Gorecki, T. (1996) 'NIR-PRFS fiber optic corrosion sensor', *Proceeding of SPIE,* 2682, 275-287.

Clark, R. A. and Krueger, G. L. (1985) 'Alurninon: Its limited application as a reagent for the detection of aluminum species', *The Journal of Histochemistry and Cytochemistry,* 33(7), 729-732.

Cooper, K. R., Elster, J., Jones, M. and Kelly, R. G. (2001) 'Optical fiber-based corrosion sensor systems for health monitoring of aging aircraft', *AUTOTESTCON Proceedings. IEEE Systems Readiness Technology Conference*, 847 - 856.

Cordeiro, C. M. B., Franco, M. A. R., Chesini, G., Barretto, E. C. S., Lwin, R., Cruz, C. H. B. and Large, M. C. J. (2006) 'Microstructured-core optical fibre for evanescent sensing applications', *Optics Express,* 14(26), 13056-13066.

Cordero, S. R., Beshay, M., Low, A., Mukamal, H., Ruiz, D. and Lieberman, R. A. (2005) 'A distributed fiber optic chemical sensor for hydrogen cyanide detection', *Advanced Environmental, Chemical, and Biological Sensing Technologies III, edited by Tuan Vo-Dinh, Robert A. Lieberman, Gunter Gauglitz, Proc. of SPIE,* 5993, 599302.

Cordero, S. R., Mukamal, H., Low, A., Beshay, M., Ruiz, D. and Lieberman, R. A. (2006a) 'Fiber optic sensor coatings with enhanced sensitivity and longevity', *Advanced Environmental, Chemical, and Biological Sensing Technologies IV edited by Tuan Vo-Dinh, Robert A. Lieberman, Günter Gauglitz Proc. of SPIE,* 6377, 63770C.

Cordero, S. R., Mukamal, H., Low, A., Locke, E. P. and Lieberman, R. A. (2006b) 'A fiber optic sensor for nerve agent', *Chemical and Biological Sensors for Industrial and Environmental Monitoring II edited by Steven D. Christesen, Arthur J. Sedlacek III, James B. Gillespie, Kenneth J. Ewing. Proc. of SPIE,* 6378, 63780U-3.

Culshaw, B. (2004) 'Optical fiber sensor technologies: opportunities and - perhaps - pitfalls', *Journal of Lightwave Technology,* 22(1), 39-50.

Dong, S., Liao, Y. and Tian, Q. (2005) 'Intensity-based optical fiber sensor for monitoring corrosion of aluminum alloys', *Applied Optics,* 44(27), 5773-5777.

Dong, S., Liao, Y., Tian, Q. (2005) 'Sensing of corrosion on aluminum surfaces by use of metallic optical fiber', *Applied Optics,* 44,(30), 6334-6337.

Dong, S., Peng, P. and Luo, Y. (2007) 'Preparation techniques of metal clad fibres for corrosion monitoring of steel materials', *Smart Materials and Structures,* 16, 733–738.

Draxler, S., Kieslinder, D., Trznadel, K. and Lippitsch, M. E. (1996) 'Fluorescence lifetime-based sensors using inhomogeneous waveguiding', *Proceeding of SPIE,* 2836, 50-56.

Duncan, R. G., Childers, B. A., Gifford, D. K., Pettit, D. E., Hickson, A. W., Duke Jr, J. C. and Brown, T. L. (2003) 'Use of a fiber optic distributed sensing system for nondestructive testing of aerospace structures', *Materials Evaluation,* 61(7), 838-843.

Fain, V. Y., Zaitsev, B. E. and Ryabov, M. A. (2004) 'Metal complexes with Alizarin and Alizarin Red S: Electronic absorption spectra and structure of ligands', *Russian Journal of Coordination Chemistry,* 30(5), 365-370.

Falciai, R., Mignani, A. G., Ciaccheri, L. and Cosi, F. (1997) 'Tapered multimode optical fibers for enhanced evanescent-wave absorption spectroscopy of liquids', *Proceedings of SPIE,* 3105, 2-12.

Foulgoc, K. L., Neindre, L. L., Zhang, X. H. and Lucas, J. (1996) 'Tapered TeX glass optical fiber for remote IR spectroscopic analysis', *Proceeding of SPIE,* 2836, 26-36.

Fuhr, P. L. and Huston, D. R. (1998) 'Corrosion detection in reinforced concrete roadways and bridges via embedded fiber optic sensors', *Smart Materials and Structures,* 7(2), 217-228.

Fuhr, P. L., Huston, D. R. and MacCraith, B. (1998) 'Embedded fiber optic sensors for bridge deck chloride penetration measurement', *Optical Engineering,* 37(4), 1221-1228.

Ghandehari, M. and Vimer, C. S. (2004) 'In situ monitoring of pH level with fiber optic evanescent field spectroscopy', *NDT and E International,* 37(8), 611-616.

Gibson, B. C. and Dower, P. M. (2007) 'Refractive index design and validation for evanescent field power maximization in optical fibre sensors', *Optics Communications,* 279(2), 303-312.

Gloge, D. (1971) 'Weakly guiding fibers', *Applied Optics,* 10(10), 2225-2258.

Grahn, W., Makedonski, P., Wichern, J., Kowalsky, W. and Wiese, S. (2002) 'Fiber optic sensors for an in-situ monitoring of moisture and pH value in reinforced concrete', *Imaging Spectrometry VII, Michael R. Descour; Sylvia S. Shen; Eds. - Proc. SPIE,* 4480, 395-404.

Greene, J. A., Jones, M. E., Tran, T. A., Murphy, K. A., Schindler, P. M., Bhatia, V., May, R. G., Sherrer, D. W. and Claus, R. O. (1996) 'Grating-based optical-fiber-based corrosion sensors', *Proceedings of SPIE,* 2718, 170-174.

Guray, T., Uysal, Ü. D., Gedikbey, T. and Huseyinli, A. A. (2005) '2,2′,3,4-Tetrahydroxy-3′-sulpho-5′-nitroazobenzene for spectrophotometric

determination of aluminium in pharmaceutical suspensions and granite', *Analytica Chimica Acta,* 545(1), 107-112.

Hale, Z. M. and Payne, F. P. (1997) *A tapered single-mode optical fibre as an intrinsic pH sensor*, Cambrige University, Department of Engineering.

Henning, P. E., Benko, A., Schwabacher, A. W., Geissinger, P. and Olsson, R. J. (2005) 'Apparatus and methods for optical time-of-flight discrimination in combinatorial library analysis', *Review of scientific instruments,* 76, 062220.

Henry, W. (1994) 'Evanescent field devices: a comparison between tapered optical fibres and polished or D-fibres', *Optical and Quantum Electronics,* 26(3), S261 - S272.

Hill, U. T. (1959) 'Photometric determination of aluminum in steel', *Analytical Chemistry,* 31 (3), 429-431.

Hinkley, E. D. (1976) *Laser Monitoring of the Atmosphere,* New York: Springer-Verlag.

Huang, Z., Pickrell, G. and Wang, A. (2004) 'Penetration rate of water in sapphire and silica optical fibers at elevated temperature and pressure', *Optical Engineering,* 43(6), 1272-1273.

Huntington, S. T., Nugent, K. A., Roberts, A., Mulvaney, P. and Lo, K. M. (1997) 'Field characterization of a D-shaped optical fiber using scanning near-field optical microscopy', *Journal of Applied Physics,* 82, 510-513.

Jenkins, F. A. and White, H. E. (1976) *Fundamentals of Optics,* New York: McGraw-Hill.

Jensen, J. B., Pedersen, L. H., Hoiby, P. E., Nielsen, L. B., Hansen, T. P., Folkenberg, J. R., Riishede, J., Noordegraaf, D., Nielsen, K., Carlsen, A. and Bjarklev, A. (2004) 'Photonic crystal fiber based evanescent-wave sensor for detection of biomolecules in aqueous solutions', *Optics Letters,* 29(17), 1974-1976.

Jeppesen and Sanderson (1985) *Aircraft Corrosion Control,* Englewood, Co. : Jeppesen Sanderson, Inc.

Jin, W., Stewart, G., Wilkinson, M., Culshaw, B., Muhammad, F., Murray, S. and Norris, J. W. (1995) 'Compensation for surface contamination in a D-fiber evanescent wave methane sensor', *Journal of Lightwave Technology,* 13(6), 1177-1183.

Johnson, R. E. and Agarwala, V. S. (1994) 'The use of fluorescent compounds and complexes of metals as early warning detectors for corrosion', *Corrosion 94. The annual Conference and Corrosion Show,* 1, 332/1-332/10.

Johnson, R. E., S, R. K. and Agarwala, V. S. (1997) 'Fluorescent based sensors for corrosion detection', *Microstructural Science,* 25, 65-70.

Kao, H. P., Yang, N. and Schoeniger, J. S. (1998) 'Enhancement of evanescent fluorescence from fiber-optic sensors by thin-film sol-gel coatings', *Journal of the Optical Society of America A,* 15(8), 2163-2171.

Kara, D., Fisher, A. and Hill, S. J. (2007) 'The sensitive and selective determination of aluminium by spectrofluorimetric detection after complexation with N-o-vanillidine-2-amino-p-cresol', *Journal of Environmental Monitoring,* (9), 994.

Kaye and Laby (2005) 'Tables of Physical & Chemical Constants (16th edition 1995). 2.5.8 Refractive index of optical materials. Kaye & Laby Online. Version 1.0', available online: www.kayelaby.npl.co.uk.

Khijwania, S. K., Gupta, B.D. (1999) 'Fiber optic evanescent field absorption sensor: effect of fiber parameters and geometry of the probe', *Optical and Quantum Electronics,* 31(8), 625-636.

Kim, K. T., Song, H. S., Mah, J. P., Hong, K. B., Im, K., Baik, S.-J. and Yoon, Y.-I. (2007) 'Hydrogen sensor based on palladium coated side-polished single-mode fiber', *IEEE Sensors Journal,* 7(12), 1767-1771.

Koch, G. H. and Thompson, N. G. (1994) 'Corrosion monitoring as a means to increase maintenance efficiency in aircraft', *Corrosion/94 "Corrosion and corrosivity sensors"*, 287-295.

Kozma, I. Z., Krok, P. and Riedle, E. (2005) 'Direct measurement of the group-velocity mismatch and derivation of the refractive-index dispersion for a variety of solvents in the ultraviolet', *Journal of the Optical Society of America B,* 22(7), 1479-1485.

Kumar, P. S., Lee, S. T., Vallabhan, C. P. G., Nampoori, V. P. N. and Radhakrishnan, P. (2002) 'Design and development of an LED based fiber optic evanescent wave sensor for simultaneous detection of chromium and nitrite traces in water', *Optics Communications* 214(1-6), 25-30.

Kurashima, T., Usu, T., Tanaka, K., Nobiki, A., Sato, M. and Nakai, K. (1997) 'Application of fiber optic distributed sensor for strain measurement in civil engineering', *Proceeding of SPIE,* 3241, 247-258.

Lee, H., Berezin, M. Y., Henary, M., Strekowski, L. and Achilefu, S. (2008) 'Fluorescence lifetime properties of near-infrared cyanine dyes in relation to their structures ', *Journal of Photochemistry and Photobiology A: Chemistry,* 200(2-3), 438-444.

Lee, S. M., Yang, C. and Pan, W. (1996) 'Evanescent coupling fiber optic pollution monitoring system using etched D-shape E-core fiber', *Proceeding of SPIE,* 2836, 267-274.

Lee, S. T., Gin, J., Nampoori, V. P. N., Vallabhan, C. P. G., Unnikrishnan, N. V. and Radhakrishnan, P. (2001) 'A sensitive fibre optic pH sensor using multiple sol–gel coatings', *Journal of Optics A: Pure and Applied Optics,* 3 355-359.

Lee, S. T., Kumar, P. S., Unnikrishnan, K. P., Nampoori, V. P. N., PGVallabhan, C., Sugunan, S. and Radhakrishnan, P. (2003) 'Evanescent wave fibre optic sensors for trace analysis of Fe3+ in water', *Measurement Science and Technology,* 14, 858-861.

Li, X. M., Chen, W., Zhu, Y., Huang, S. and Bennett, K. D. (2000) 'Monitoring the corrosion of steel in reinforced concrete using optical waveguide methods', *Smart Structures and Materials 2000: Sensory Phenomena and Measurement Instrumentation for Smart Structures and Materials,* 3986, 172-179.

Lieberman, R. A., Blyler, L. L. and Cohen, L. G. (1989) 'A distributed fiber optic sensor based on cladding fluorescence', *Journal of Lightwave Technology,* 8(2), 212 - 220

Lo, Y. L. and Xiao, F.-Y. (1998) 'Measurement of corrosion and temperature using a single-pitch Bragg grating fiber sensor', *Journal of Intelligent Material Systems and Structures (USA),* 9(10), 800-807.

Ma, J. and Bock, W. J. (2007) 'Dramatic performance enhancement of evanescent-wave multimode fiber fluorometer using non-Lambertian light diffuser', *Optics Express,* 15(25), 16457-16470

MacCraith, B. D. and McDonagh, C. (2002) 'Enhanced fluorescence sensing using sol-gel materials', *Journal of Fluorescence,* 12(3-4), 333-342.

MacCraith, B. D., Ruddy, V., Potter, C., O'Kelly, B. and McGilp, J. F. (1991) 'Optical waveguide sensor using evanescent wave excitation of fluorescent dye in sol-gel glass', *Electronics Letters,* 27(14), 1247-1248.

Mackenzie, H. F. and Payne, F. P. (1990a) 'Evanescent field amplification in a tapered single-mode optical fibre', *Electronics Letters,* 26(2), 130-132.

Mackenzie, H. F. and Payne, F. P. (1990b) 'Saturable absorption in a tapered single-mode optical fibre', *Electronics Letters,* 26(21), 1744-1745.

MacLean, A., Moran, C., Johnstone, W., Culshaw, B., Marsh, D. and Parker, P. (2003) 'Detection of hydrocarbon fuel spills using a distributed fibre optic sensor ', *Sensors and Actuators A: Physical,* 109(1-2), 60-67.

Madrakian, T., Afkhami, A., Borazjani, M. and Bahram, M. (2005) 'Partial least-squares regression for the simultaneous determination of aluminum and beryllium in geochemical samples using xylenol orange', *Spectrochimica Acta Part A,* 61 2988-2994.

Maleki, N., Safavi, A. and Sedaghatpour, F. (2004) 'Single-step calibration, prediction and real samples data acquisition for artificial neural network using a CCD camera', *Talanta,* 64 830-835.

Marcuse, D. (1988) 'Launching light into fiber cores from sources located in the cladding', *Journal of Lightwave Technology,* 6(8), 1273-1279.

Marcuse, D., Ladouceur, F. and Love, J. D. (1992) 'Vector modes of D-shaped fibres', *Optoelectronics, IEE Proceedings J,* 139(2), 117 - 126.

McAdam, G., Newman, P. J., McKenzie, I., Davis, C. and Hinton, B. R. W. (2005) 'Fiber optic sensors for detection of corrosion within aircraft', *Structural Health Monitoring,* 4, 47 - 56.

Mendoza, E. A., Khalil, A. N., Sun, Z., Robinson, D., Syracuse, S. J., Egalon, C. O., Gunther, M. F. and Lieberman, R. A. (1995) 'Embeddable distributed moisture and pH sensors for nondestructive inspection of aircraft lap joints', *Proceeding of SPIE,* 2455, 102-112.

Mendoza, E. A., Robinson, D. and Lieberman, R. A. (1996) 'Miniturized integrated optic chemical sensors for enviromental monitoring and remediation', *Proceeding of SPIE,* 2836, 76-87.

Menra, R. (2003) 'Application of refractive index mixing rules in binary systems of hexadecane and heptadecane with n-alkanols at different temperatures', *Chemical Science - Indian Academy of Sciences,* 115(2), 147-154.

Misra, V., Mishra, H., Joshi, H. C. and Pant, T. C. (2002) 'An optical pH sensor based on excitation energy transfer in Nafion® film', *Sensors and Actuators B: Chemical,* 82(2-3), 133-141.

Moar, P. N., Huntington, S. T., Katsifolis, J., Cahill, L. W., Roberts, A. and Nugent, K. A. (1999) 'Fabrication, modeling, and direct evanescent field measurement of tapered optical fiber sensors ', *Journal of Applied Physics,* 85(7), 3395-3398.

Morisawa, M., Uchiyama, K., Hosaka, T., Inoue, H., Muto, S., Namazue, A., Nihei, E. and KoikeYasuhiro (1996) 'New cladding polymer for optical oxygen sensor using fluorescent plastic fiber', *Proceeding of SPIE,* 2836, 336-340.

Mukamal, H., Cordero, S. R., Ruiz, D., Beshay, M. and Lieberman, R. A. (2005) 'Distributed fiber optic chemical sensor for hydrogen sulfide and chlorine detection', *Fiber Optic Sensor Technology and Applications IV edited by Michael A. Marcus, Brian Culshaw, John P. Dakin - Proceedings of SPIE,* 6004, 600406.

Murphy, V., MacCraith, B. D., Butler, T. M., McDonagh, C. M. and Lawless, B. (1996) 'Quasi-distributed fiber optic chemical sensing using telecomoptical fibers', *Proceeding of SPIE,* 2836, 261-266.

Muto, S., Suzuki, O., Amano, T. and Morisawa, M. (2003) 'A plastic optical fibre sensor for real-time humidity monitoring', *Measurement Science and Technology,* 14(6), 746-750.

Nadzhafova, O. Y., Lagodzinskaya, S. V. and Sukhan, V. V. (2001) 'Test paper for the determination of aluminum in solution', *Journal of Analytical Chemistry,* 56(2), 178-181.

Norris, J. O. W. (2000) 'Optical fiber chemical sensors: Fundamental and applications' in Grattan, K. T. V. and Meggitt, B. T., eds., *Optical Fiber Sensor Technology*, Kluwer Academic Publishers, 337-378.

Oraby, O. A., Spencer, J. W. and Jones, G. R. (2009) 'Monitoring changes in the speckle field from an optical fibre exposed to low frequency acoustical vibrations ', *Journal of Modern Optics,* 56(1), 55 - 66.

Orghici, R., Willer, U., Gierszewska, M., Waldvogel, S. R. and Schade, W. (2008) 'Fiber optic evanescent field sensor for detection of explosives and CO2 dissolved in water', *Applied Physics B: Lasers and Optics,* 90(2), 355-360.

Encyclopedia of Laser Physics and Technology (2008) Berlin: Wiley-VCH.

Pendock, G., Mackenzie, H. S. and Payne, F. P. (1992) 'Tapered optical fibre dye laser', *Electronics Letters,* 28(2), 149-150.

Potyrailo, R. A. and Hieftje, G. M. (1998a) 'Optical time-of-flight chemical detection: Absorption-modulated fluorescence for spatially resolved analyte mapping in a bidirectional distributed fiber-optic sensor', *Analytical Chemistry,* 70, 3407-3412.

Potyrailo, R. A. and Hieftje, G. M. (1998b) 'Optical time-of-flight chemical detection: Spatially resolved analyte mapping with extended-length continuous chemically modified optical fibers', *Analytical Chemistry,* 70, 1453-1461.

Potyrailo, R. A. and Hieftje, G. M. (1999) 'Use of the original silicone cladding of an optical fiber as a reagent-immobilization medium for intrinsic chemical sensors', *Fresenius J Anal Chem,* 364, 32-40.

Potyrailo, R. A., Ruddy, V. P. and Hieftje, G. M. (1996) 'Kramers-Kronig analysis of molecular evanescent-wave absorption spectra obtained by multimode step-index optical fibers', *Applied Optics,* 35(21), 4102-4111.

Potyrailo, R. A., Ruddy, V. P. and Hieftje, G. M. (1999) 'Use of analyte-modulated modal power distribution in multimode optical fibers for simultaneous single-wavelength evanescent-wave refractometry and spectrometry', *Analytical Chemistry,* 71(21), 4956-4964.

Potyrailo, R. A., Szumlas, A. W., Danielson, T. L., Johnson, M. and Hieftje, G. M. (2005) 'A dual-parameter optical sensor fabricated by gradient axial doping of an optical fibre', *Measurement Science and Technology,* 16, 235-241.

Ravi Kishore, V. V. N., Narasimhan, K. L. and Periasamy, N. (2003) 'On the radiative lifetime, quantum yield and fluorescence decay of Alq in thin films', *Physical Chemistry Chemical Physics,* 5(7), 1386-1391.

Rayss, J. and Sudolski, G. (2000) 'Complex refractive index conceptfor the description of sevanescent wave sensor', *Opto-Electronics Review,* 8(2), 129-135.

Roberge, P. R. (2007) *Corrosion Inspection and Monitoring,* John Wiley & Sons.

Rogers, A. (1999) 'Distributed optical-fiber sensing', *Measurement Science and Technology,* 10, R75-R99.

Ruddy, V., MacCraith, B. D. and Murphy, J. A. (1990) 'Evanescent wave absorption spectroscopy using multimode fibers', *Journal of Applied Physics,* 67(10), 6070-6074.

Rutherford, P. S., Ikegami, R., Shrader, J., Sherrer, D. W., Zabaronick, N., Zeakes, J. S., Murphy, K. A. and Claus, R. O. (1996) 'Novel NDE fiber optic corrosion sensor', *Proceeding of SPIE,* 3042, 248-259.

Schaefer, P., Lou, K.-A., Yaniv, G. and Stevens, D. (1996) 'Development of a novel low-cost fiber optic system for structural applications', *Proceeding of SPIE,* 2719, 238-246.

Schubert, E. F. (2006) *Light-Emitting Diodes,* 2 ed.*,* Cambridge University Press.

Singh, N., Jain, S. C., Aggarwal, A. K., Singla, M. L. and Singh, M. (2000) 'A simple fiber optic technique for in-situ corrosion sensing in structures', *Nondestructive Evaluation of Aging Materials and Composites IV,* 3993, 201-205.

Smolka, S., Barth, M. and Benson, O. (2007) 'Highly efficient fluorescence sensing with hollow core photonic crystal fibers', *Optics Express,* 15(20), 12783-12791.

Snyder, A. W. and Love, J. D. (1983) *Optical Waveguide Theory,* London New York: Chapman and Hall.

Spillman Jr , W. B., Kline, B. R., Maurice, L. B. and Fuhr, P. L. (1989) 'Statistical-mode sensor for fiber optic vibration sensing uses', *Applied Optics,* 28(15), 3166-3176.

Stewart, G., Jin, W. and Culshaw, B. (1997) 'Prospects for fibre-optic evanescent-field gas sensors using absorption in the near-infrared', *Sensors and Actuators B: Chemical,* 38-39, 42-47.

Stewart, G. and Johstone, W. (1996) 'Evanescently coupled components' in Culshaw, B. and Dakin, J., eds., *Optical Fiber Sensors. Components and Subsystems*, Boston, London: Artech House, 69-102.

Stoddart, P. R., Cadusch, P. J., Pearce, J. B., Vukovic, D., Nagarajah, C. R. and Booth, D. J. (2005) 'Fibre optic distributed temperature sensor with an integrated background correction function', *Measurement Science and Technology,* 16(6), 1299-1304.

Szunerits, S. and Walt, D. R. (2002) 'Aluminum surface corrosion and the mechanism of inhibitors using pH and metal ion selective imaging fiber bundles', *Analytical Chemistry,* 74(4), 886-894.

Totten, G. E. and MacKenzie, D. S. (2003) *Handbook of Aluminum,* New York Basel: Marcel Dekker Inc.

Trego, A., Haugse, E. and Udd, E. (1998) 'Material removal rate fiber optic corrosion sensor', *Pacific Northwest Fiber Optic Sensor Workshop 4th, Jung, Chuck C., Udd, Eric; Eds. - Proc. SPIE,* 3489, 105-109.

Valeur, B. and Berberan-Santos, M. N. (2013) *Molecular Fluorescence: Principles and applications,* Wiley.

Vargel, C. (2004) *Corrosion of Aluminium,* Amsterdam - San - Diego - Oxford - London: Elsevier.

Wallace, P. A., Campbell, M., Yang, Y., Holmes-Smith, A. S. and Uttamlal, M. (1997) 'A distributed optical fibre fluorosensor for pH measurement ', *Journal of Luminescence,* 72-74 1017-1019.

Wallington, S.-A., Labayen, T., Poppe, A., Sommerdijk, N.A.J.M., Wright, J.D. (1997) 'Sol-gel entrapped materials for optical sensing of solvents and metal ions ', *Sensors and Actuators B: Chemical,* 38(1-3), 48-52.

Warren-Smith, S. C., Sinchenko, E., Stoddart, P. R. and Monro, T. M. (2010) 'Distributed fluorescence sensing using exposed core microstructured optical fiber', *IEEE Photonics Technology Letters,* 22(18), 1385-1387.

Wauer, G., Heckemann, H.-J. r. and Koschel, R. (2004) 'Analysis of toxic aluminium species in natural waters', *Microchimica Acta,* 146, 149-154.

Wolfbeis, S. O. (1997) 'Chemical sensing using indicator dyes' in Dakin, J. and Culshaw, B., eds., *Optical fiber sensors. Applications, Analysis, and Future Trends*, Boston, London: Artech House, 53-103.

Xu, Z., Rollins, A., Alcala, R. and Marchant, R. E. (1998) 'A novel fiber-optic pH sensor incorporating carboxy SNAFL-2 and fluorescent wavelength-ratiometric detection', *Journal of Biomedical Materials Research Part A,* 39(1), 9 - 15.

Yin, S., Ruffin, P. B. and Yu, F. T. S., eds. (2008) *Fiber Optic Sensors, Second Edition,* New York: CRC Press.

Zen, J. M., Lipowska, M. and Patonay, G. (1992) 'Near-infrared probe for in situ characterization of nafion thin films', *Journal of Applied Polymer Science,* 46(7), 1167-1176.

Zen, J. M. and Patonay, G. (1991) 'Near-infrared fluorescence probe for pH determination', *Analytical Chemistry,* 63(24), 2934 - 2938.

Zhou, W., Gao, B., Yue, Q., Liu , L. and Wang, Y. (2006) 'Al-Ferron kinetics and quantitative calculation of Al(III) species in polyaluminum chloride coagulants ', *Colloids and Surfaces A: Physicochemical and Engineering Aspects,* 278(1-3), 235-240.

Zhu, Y., Du, H. and Bise, R. (2006) 'Design of solid-core microstructured optical fiber with steering-wheel air cladding for optimal evanescent-field sensing', *Optics Express,* 14(8), 3541-3546.

Appendix 1. Sentor 101 overview

Sentor 101 is a member of a family of temperature measurement systems that are collectively described as Distributed Temperature Sensors or DTS for short. A distributed temperature sensor monitors temperatures continuously along the length of its sensor. This technique contrasts to the use of "spot" sensors that monitor a single point location only.

The Sentor 101 system comprises three major components:

- Data acquisition unit.
- Computer - performing control, information processing and presentation functions.
- Optical fibre sensor.

The data acquisition unit and computer comprise the SENTOR 101® unit with the optical fibre used as the sensor. There are many advantages gained when an optical fibre is used as the sensor, including electrical isolation and immunity to electromagnetic radiation.

A1.1 Operation

The Sentor 101 distributed temperature sensor works by launching pulses of laser radiation, typically 2-10 ns duration, into an optical fibre, which is in contact with the structure to be measured. As each laser pulse travels along the fibre a small fraction of the incident pulse is absorbed by the fibre atoms and is back scattered as Raleigh and Raman components. The intensity of the short wavelength Raman part depends on the local fibre temperature.

The Sentor 101 monitors the back-scattered signal using:

- the photon counting method to record intensity and
- the arrival time to identify position.

For a 1 km length of fibre, the travel and return time to the end of the fibre will be approximately 10 microseconds. After this time the Sentor 101 unit rearms itself and fires another sensing pulse. This process continues for the nominated acquisition time so that, in say a 100 second period the system will have probed the temperature profile along the fibre as many as 10 million times. The accumulated photon count as a

function of position along the fibre is then downloaded to a central processing unit. The central processing unit then performs a series of calculations to allow for such factors as splice losses, attenuation as a function of position and temperature sensitivity of the Raman to return a temperature value for each point along the fibre.

The Sentor 101 requires high-speed electronics for the laser drive and photon detection circuits but uses the essential advantages of the photon counting method to simplify all other aspects of operation. Compared with intensity-based units the laser drive power is extremely modest and economical. There are no extremely high speed and costly analogue to digital converters or signal analysis and averaging systems. With intensity based systems many photons are required to create a measurable signal at each point along the fibre. With the photon counting method the opposite is true. With the photon counting system most of the time it is required that no photon be received and detected. If two photons were to arrive at the same time the system would record only the first and the result would be a non-uniform response. The Sentor 101 system is usually adjusted to have a laser power level that will create a maximum of one back-scattered Raman photon for each 50 outgoing pulses. This still gives up to 500,000 counts at short positions along the fibre and is a huge saving of laser power over intensity-based systems.

The Sentor 101 makes no resolution sacrifice when presenting data to user-chosen post-averaging detail. All records can be retained with maximum detail and can be post processed at any time to optimise presentation accuracy consistent with user resolution choices. For example, if an application suffers a fault that creates a progressive increase in heat dissipation it is likely that heat diffusion will occur slowly in time and spread away from the fault point. To optimise the diagnostic view an average over many time periods will maximise the temperature resolution of the thermal profile as a function of position away from the fault point. If, instead, the fault occurs suddenly it is likely to create a rather rapid temperature rise. In such a case, it is unlikely that temperature resolution will be an essential factor in identifying the problem, rather detailed time and space resolution, with a sufficient temperature resolution of perhaps 20°C will be more appropriate. With the Sentor 101, these post-record resolution compromises are always available.

The Sentor 101 makes many thousands of temperature measurements per second and can easily meet the most demanding time resolution specifications. The system will average the measurements over a user nominated acquisition time to improve the

accuracy of the final results. Even with intimate contact between fibre and target there will be very few applications that can expect meaningful results with less than 10 seconds of measurement time. Large objects such as heavy-duty electrical cables or transformers have temperature time constants of the order of hours and a measurement time of 30 minutes will optimise temperature and long distance space resolution and minimise reporting needs.

The Sentor 101 distributed temperature sensor divides its space measurements into 200mm intervals. For most applications, a resolution of one or more metres is sufficient and in these cases a system of reduced cost and improved temperature resolution will usually be preferred. The higher space resolution option can be retrofitted at any time and is determined only by the existing laser pulse duration. It is independent of the installed sensing fibre.

A1.2 Performance

The Sentor 101 distributed temperature sensor has three measurement dimensions so that resolution involves interaction between:

1. Space resolution over the length of the fibre
2. Time
3. Temperature resolution

A1.3 Advantages over point sensors

The positioning of point sensors requires advance knowledge of the hottest spots in an asset. Since this is not predictable with certainty under all operating conditions, many points must be monitored. For an application requiring more than five point sensors, the Sentor 101 system can offer very considerable savings and provide a higher level of data quality.

Appendix 2. Techniques for statistical analysis of the experimental data

Research experiments are frequently highly uncertain due to the goals of novelty defining research projects. Although the instrumentation used in the research project must function properly it is often delicate and requires considerable attention. Quite often experimental measuring systems whose characteristics are not completely defined are used during the research program. In such cases, statistical tools can be used to plan experiments and interpret the resulting experimental data in a sensible manner. Also special measurement techniques may be created to overcome imperfection of the measurement system and produce valid results.

In most experiments the experimenter seeks to obtain numerical values for certain physical variables called the measurand. Even if a measurand is fixed and the measuring system stays unchanged, repeated measurements will produce different resulting values. It is very important to the experimenter that the output of a measuring system truly states the actual value of the measurand. But because there is no measuring system which is perfect the obtained numerical value contains an error which is normally unknown. The exact value of the error can not be found exactly. However, it is possible to estimate the uncertainty interval (or uncertainty) of the measurement. The uncertainty is an estimate of the error in the measurement within some level of confidence (normally expressed as a percentage). In other words, it can be stated, for example that at a 95 % confidence level, the true value of a measurand falls in the estimated limits of error.

Confidence level is normally expressed in terms of a variable α called level of significance. The level of significance represents the probability that the estimated value of the measurand falls outside the confidence interval.

The measurement result is often presented in the form:

$$R = \bar{R} \pm \omega_r , \qquad \text{(A2.1)}$$

where $\bar{R}$ - is the estimated numerical value of the measurand,

ω_r - is the estimated uncertainty with a predetermined level of confidence or level of significance α. The error limits can be found by analyzing both the raw experimental data using suitable statistical techniques as well as characteristics of the measuring system.

There are two categories of errors in an experiment: systematic errors and random errors. Systematic errors are consistent, repeatable errors. They are frequently caused by improper calibration of the components of the measuring system. They can also result from a particular application of the measuring system, when constant offset in the obtained data can be introduced. Systematic errors cannot be estimated by repeating the experiment with the same equipment. Systematic errors may be detected and reduced by the process of calibration; also they can be reduced by analytical correction of the data for unwanted effects.

Random errors characterize unpredictable scattering in the output of the measuring system. Random errors originate not only from the measuring system by itself, but also from the experimental system and environment. The process under study itself might be highly variable. Random errors are easy to detect and reduce by repeating the experiment and performing statistical analysis. They can also be reduced by refining the measurement method or technique.

Although random errors can be reduced by multiple repetition of the experiment, there are some limitations that prevent indefinite error reduction. Three main limitations to consider include the available time and resources, systematic errors, and nonstatistical fluctuations.

A2.1 Estimating random error (uncertainties)

Consider a population of the random variable x with a mean μ and standard deviation σ. From this population different samples are taken, each of size n.

The best estimation for the population mean (μ) which represents the actual value of the measurand will be the sample mean $\bar{x}$.

$$\bar{x} = \frac{\sum_{i=1}^{n} x_i}{n} \tag{A2.2}$$

The quality of this estimation is characterized by a random uncertainty of the measurement (denoted as P_x). The central limit theorem makes it possible to estimate P_x and therefore the confidence interval of the estimated population mean with a suitable confidence level.

First, from the sample data a sample standard deviation (S_x) can be calculated as:

$$S_x = \sqrt{\sum_{i-1}^{n} \frac{(x_i - \bar{x})^2}{n-1}} \tag{A2.3}$$

Then, the estimate of the standard deviation of the sample mean can be written as:

$$\sigma_{\bar{x}} = \frac{S_x}{\sqrt{n}} \tag{A2.4}$$

Estimating random uncertainty of the measurement depends on the sample size. It is estimated using the normal distribution if the sample size is sufficiently large. In most cases, to be considered large, the sample size should exceed 30.

In the case when the sample size is large, a confidence interval can be found:

$$\bar{x} - \zeta_{\alpha/2} \frac{S_x}{\sqrt{n}} \le \mu \le \bar{x} + \zeta_{\alpha/2} \frac{S_x}{\sqrt{n}}, \tag{A2.5}$$

where $\zeta_{\alpha/2}$ is a coefficient which can be found from the normal distribution for a predetermined (desirable) level of confidence. Modern statistical software provides instruments easily finding the $\zeta_{\alpha/2}$ coefficients.

Or in other words the random uncertainty in the mean is:

$$P_x = \pm \zeta_{\alpha/2} \frac{S_x}{\sqrt{n}}. \tag{A2.6}$$

If the sample size is small, the assumption that the population standard deviation can be represented by the sample standard deviation may not be accurate. Due to the uncertainty in the standard deviation, for the same confidence level, we would expect the confident interval to be wider. In case of small samples, instead of the normal

distribution, the so called t-distribution (or Student's distribution) is used and the random uncertainty can be written as:

$$P_x = \pm t \frac{S_x}{\sqrt{n}}, \qquad \text{(A2.7)}$$

where t - is Student's coefficient, which can be determined from the t-distribution with the predetermined level of confidence and degrees of freedom using statistical software tools or even the traditional tables for the t-distribution.

A2.2 Basic statistic for a single measurement experiment

If an experiment is conducted only once or at most a few times for each test condition, it is considered to be a single-measurement experiment. In this case, it is impossible to calculate the standard deviation of the sample S_x directly from the actual measurement. S_x is usually determined through a secondary source, such as manufacturers' specifications or auxiliary tests run prior to taking the final data. In case the mean value is obtained from different set of tests than the standard deviation, the final value of the variable x determined from M measurements of x is given:

$$\bar{x} = \frac{\sum_{i=1}^{M} x_i}{M}. \qquad \text{(A2.8)}$$

The random uncertainty in $\bar{x}$ is given by:

$$P_{\bar{x}} = \pm \frac{S_x}{\sqrt{M}}. \qquad \text{(A2.9)}$$

where t is the Student's coefficient determined on the basis of the degrees of freedom ν defined as $\nu = n - 1$ for the auxiliary tests used to determine S_x and the desired confidence level.

It is generally recommended that S_x be determined in tests with a large sample size. A large sample size simplifies the uncertainty analysis considerably and provides more rigorous results.

A2.3 Combination of systematic and random components of uncertainties

Systematic and random uncertainties need to be evaluated with the same level of confidence to be combined in a final figure.

The total uncertainty is obtained by combining systematic and random uncertainties using:

$$W_{\bar{x}}^2 = P_{\bar{x}}^2 + B_{\bar{x}}^2 . \qquad \text{(A2.10)}$$

This combination rule is true for any number of so-called elemental uncertainties which can be determined separately during the analysis of the experiment. Each component of the experiment can generate either a systematic or random error. Normally, there are several elemental error sources in the measurement of each variable x, and uncertainty in x will be a combination of the uncertainties due to these sources. Thus, the systematic uncertainties and the standard deviations are each combined:

$$B_x^2 = \sum_{i=1}^{k} B_i^2 , \qquad \text{(A2.11)}$$

$$S_x^2 = \sum_{i=1}^{m} S_i^2 , \qquad \text{(A2.12)}$$

where k is a number of elemental systematic uncertainties and m is the number of elemental random uncertainties pertaining to the measured variable x.

It is practical to separately estimate and compare the various contributions of the elemental uncertainties to the uncertainty of the final result. A convenient rule of thumb is to neglect those uncertainties that make contributions of less than 10 %. Certainly, some care should be applied, because several smaller contributors to the final uncertainty can sum up to be as important as one large uncertainty.

Information about elemental systematic and random uncertainties caused by measurement instruments used in the experiment can be obtained from manufacturers' specifications. It is common for manufacturers to supply the uncertainty descriptor called accuracy. Accuracy usually includes errors due to hysteresis, linearity and repeatability, but assumes that the calibration is correct and there is no zero offset.

When accuracy is reported, it is treated as systematic uncertainty. Other reported elemental errors, such as thermal stability, that are not included in accuracy, should be treated as separate elemental errors. Sometimes in the specifications, systematic and random uncertainties are listed separately. Combining random errors from the manufacturers' specifications (like repeatability) with other statistically well-defined random elemental uncertainties can be problematic because often they are provided as a bonding number rather than an estimate with a set confidence level. A possible approach is to assume that the provided error value is a 95 % confidence random uncertainty based on a sample size greater than 30. With these assumptions, a value for the standard deviation can be obtained by dividing the provided error number by the value of Student's t for 95 % confidence level and sample size greater than 30 ($t \approx 2$). The same approach can be used for other random uncertainty data given without a defined statistical basis.

A2.4 Propagation of uncertainties

In general, the result of the experimentation that we are interested in, is calculated as a function of a number of measured variables $x_1, x_2, ..., x_l$, where l is the number of measured variables. That is:

$$R = f(x_1, x_2, ..., x_l). \tag{A2.13}$$

The best estimation of R is given by:

$$\bar{R} = f(\bar{x}_1, \bar{x}_2, ... \bar{x}_l). \tag{A2.14}$$

If we knew the actual error of every measured variable (denoted by ω_{x_i}), we could obtain an estimate of the error in the final result $\bar{R}$ by expanding R about the point $\bar{R} = f(\bar{x}_1, \bar{x}_2, ... \bar{x}_l)$ in a Taylor series. Thus the uncertainty in the result is:

$$\omega_R = \sum_{i=1}^{n} \omega_i \frac{\partial R}{\partial x_i}. \tag{A2.15}$$

This approximation neglects higher-order terms in the Taylor expansion. In most cases a first order approximation is sufficient, but in rare special cases, if the errors are

large, including at least second partial derivatives and partial cross derivatives might be necessary.

Using the conception of the square root of the sum of the squares, a better estimate for the result uncertainty is given by:

$$\omega_R = \sqrt{\sum_{i=1}^{n}\left[\omega_{x_i}\frac{\partial R}{\partial x_i}\right]^2}\ . \qquad \text{(A2.16)}$$

The confidence level of uncertainty in the result is the same as the confidence levels of the uncertainties in the variables x_i. Hence, it is important that all uncertainties be evaluated at the same confidence level.

This is another significant restriction based on the fact that each of the measured variables should be independent of each other. In special cases, when variables are found to be correlated, special terms which represent correlation between the variables should be included.

A2.5 Errors of photon counting with a photomultiplier tube

Photon counting is an effective technique used to detect the very low level light signals that are typically present in Raman spectroscopy applications, fluorescence applications, as well as in chemical and biological luminescence analysis. By using a fast photomultiplier tube (PMT) to detect the light and equally fast electronics to process the signal, the arrival of individual photons can be detected and counted. Single photon counting becomes possible when the incident light intensity is very low and reaches a state in which no more than two photoelectrons are received within the time resolution (pulse width) of the photomultiplier tube. Thus, every incident photon produces a discrete pulse of an electrical current. By discriminating these discrete pulses at a binary level, the number of signal pulses can be counted in a digital mode. This process is commonly known as photon counting.

The electronic detection of light by the photoelectric effect is fundamentally limited by statistical fluctuations. The statistical fluctuations which are superposed on the signal originate from:

- shot noise resulting from the signal light,

- shot noise resulting from the background light,
- shot noise resulting from the dark current.

Individual photon detections can be treated as independent events that follow a random temporal distribution. As a result, photon counting is a classic Poisson process. The probability $P_N(t)$ of counting N photons in the time interval t is described as:

$$P_N(t) = \frac{(rt)^N e^{-rt}}{N!}, \qquad \text{(A2.17)}$$

where r is the expected mean arrival rate of photons.

If the measurement is repeated a large number of times and the measured values of N are averaged, that average will approximate the mean value of Equation (A2.17), which is rt. And because the photon count follows a Poisson distribution, it has the property that its variance is equal to its expectation. That means that the standard error in the measured values of N will approximate the standard deviation of Equation (A2.17), which is $\sqrt{rt}$. Thus, if N is a moderately large number, a reasonably accurate estimate of the standard deviation in N (σ_N) is:

$$\sigma_N^2 = N \text{ or } \sigma_N = \sqrt{N}. \qquad \text{(A2.18)}$$

This shows that the statistical fluctuations depend on the measured values of N, and that their standard deviation grows with the square root of N.

Typically in the photon counting mode the number of observations which is defined as a product of the laser pulse repetition frequency and the total observation time is sufficiently large (~10^7 for a laser pulse repetition frequency of 25 kHz and a total observation time of 10 min, for example). This allows use of the described above formulae for the average and the standard error.

In the case of synchronous pulse-gated photon counting, the signal component (N_S) is derived by subtraction of the total noise contribution (N_N) from the total detected number of counts (N_T), both of which are detected alternately in the same time duration. The total noise contribution includes the number of noise photoelectrons due to background (N_b) and the number of noise photoelectrons due to dark current (N_d):

$$N_S = N_T - N_N = N_T - (N_b + N_d) \tag{A2.19}$$

The subtraction of the total noise contribution reduces significantly the systematic error in the signal component. But because the fluctuations in the signal and in the total noise are independent, uncertainties caused by those fluctuations should be combined, thus standard deviation in the signal component is:

$$\sigma_S = \sqrt{N_T + N_N} = \sqrt{N_S + 2(N_b + N_d)} \tag{A2.20}$$

where σ_S represents the random error in the signal component. The standard deviation σ_S provides a reasonable estimation for the confidence limits of the measured signal component in the photon counting mode.

A2.6 Fitting models to experimental data: Estimation of the fit parameters

It is often desirable to represent empirical data from research experiments using a model based on mathematical equations. The model needs to be based on a good understanding of the underlying physics, chemistry, electronics, and other properties of a problem. No graphing or analysis software can choose a model for the given data — it can only be useful in differentiating between models. Once a model is chosen, different curve fitting procedures can be employed to find parameters of the model.

Let us consider a typical output of a research experiment when a series of N measurements of a pair (x_i, y_i) is obtained in the experiment. Typically variable y is measured at a discrete set of values of variable x; so, x is called the independent variable and y the dependent variable. Our object is to find parameters (which will be denoted as A) of function $y = f(x, A)$ which represents the chosen model and describes the relation between the variables. In the simplest well established case, known as linear regression, a straight line is fitted to the data. In most scientific and engineering models, however, the dependent variable depends on the parameters in a nonlinear way.

We assume that there are experimental uncertainties in the individual measurements (x_i, y_i) which prevent us from finding exact values for the parameters A

of the model function $y = f(x, A)$. We can only find some optimal evaluation of the parameters. There is no correct and unique method for optimization of the parameters that is valid for all problems. There is, however, a method that is well established experimentally and is fairly well justified. This is *the method of least squares*. In the method of least squares the weighted sum of squared residuals is used as a figure-of-merit to adjust the parameters of the model. The weighted sum of squared residuals or chi-squared is:

$$\chi^2(A) = \sum_{i=1}^{N} \left(\frac{y_i - f(x_i, A)}{\sigma_i} \right)^2 = \sum_{i=1}^{N} \omega_i (y_i - f(x_i, A))^2 \qquad \text{(A 2.21)}$$

where the weights are based on the experimental standard deviation in the measurement y_i : $\omega_i = \frac{1}{\sigma_i^2}$.

The weighted sum of squared residuals or chi-squared is related to the discrepancy between the measured values y_i and the values calculated from the model $y = f(x_i, A)$. Optimal (or best-fit) parameters A can be achieved by minimizing the weighted sum of squared residuals.

In most cases, the relationship between measured values and measurement variables is nonlinear. In nonlinear models, analytical methods of least-square fitting can not be used, so approximating methods must be considered. In general, χ^2 can be treated as a continuous function of the parameters A, describing a hypersurface in a multi-dimensional space. Then a search is performed through that space for the appropriate minimum value of χ^2. Alternatively, approximation methods developed for finding roots of coupled, nonlinear equations can be used. Because the nonlinear fitting procedure is usually iterative, it always starts with an initial guess of parameter values. A good understanding of the selected model is important because the initial guess of the parameter values must make sense in the real world. The most widely used iterative procedure for nonlinear curve fitting is the Levenberg–Marquardt algorithm, which is implemented in commercially available fitting softwares. Starting from some initial values of the parameters, the method tries to minimize χ^2 by successive small variations of the parameter values and reevaluation of χ^2 until a minimum is reached.

Often, curve fitting is done without weighting if the standard deviations σ_i for the data points y_i are unknown. In this case, in the formula (A 2.21) for χ^2, the weights ω_i are all set to 1.

In the special case when all of the standard deviations are equal $\sigma_i^2 = \sigma^2$ (common uncertainties) it is possible to estimate them from the data and the results of the fit. This requirement of equal errors may be satisfied if the uncertainties are instrumental and all data are recorded with the same instrument and on the same scale. An estimate of $\sigma_i^2 = \sigma^2$ for the standard deviation of an individual measurement is:

$$\sigma^2 \approx s^2 = \frac{1}{N-m}\sum_{i=1}^{N}(y_i - f(x_i, A))^2 \qquad \text{(A 2.22)}$$

where $N-m$ is the number of degrees of freedom and is equal to the number of measurements minus the number of parameters determined from the fit. In Equation (A 2.22) the value $f(x_i, A)$ calculated using the fitted parameters was used as the expected mean value of y_i.

If experimental measurement errors are known and they are different from one another (variable uncertainties), they should be introduced into the fitting procedure as σ_i. They then provide an uneven weighting of different experimental points: the smaller the measurement error for a particular experimental point, the larger the weight of that point in χ^2. Curve-fitting software normally allows users to supply measurement errors for use in the fitting process.

A2.6.1 Goodness-of-fit statistics: Criteria for comparing models

Because of experimental errors, typical data never exactly fit the model that is being used, even when that model is correct. Therefore after fitting data with the model, it is necessary to evaluate the goodness of fit. A visual examination of the fitted curve and the graphed data points is a first step to check that the curve provides a good representation of the data. The residuals plot is also useful because it provides insight into the quality of the fitted curve. Residuals are the deviation of the data points from the fitted curve. Normally, if the curve fits the data well, the data-point deviations are randomly distributed around the fitted curve. On the other hand, a nonrandom

distribution of residuals means that the behaviour may be driven by a hidden variable which was not accounted by the model.

Beyond that, there is a need to test goodness-of-fit against some useful statistical standards.

Sum of squares due to error (SSE) measures the total deviation of the measured values (y_i) from the fit to the measured values ($f(x_i, A)$). It is also called the summed square of residuals.

$$SSE = \sum_{i=1}^{N} \omega_i (y_i - f(x_i, A))^2 \qquad \text{(A 2.23)}$$

This is identical to the chi-squared statistic in Equation (A 2.21). A calculated value closer to 0 indicates that the model has a smaller random error component, and that the fit is more useful for prediction.

The *R-squared* (R^2) statistic is the square of the correlation between the measured values (y_i) and the predicted values $f(x_i, A)$. It measures how successful the fit is in explaining the variation of the data.

$$R^2 = 1 - \frac{\sum_{i=1}^{N} \omega_i (y_i - f(x_i, A))^2}{\sum_{i=1}^{N} \omega_i (y_i - \bar{y})^2} = 1 - \frac{SSE}{SST} \qquad \text{(A 2.24)}$$

where $\bar{y}$ is the mean of the observed data values and $SST = \sum_{i=1}^{N} \omega_i (y_i - \bar{y})^2$ is the total sum of squares.

R-squared can take on any value between 0 and 1. Values closer to 0 indicate that the model accounts for a bigger fraction of the variance between the data and the model. Increasing the complexity of the model, which is usually done by bringing extra fitted coefficients into the model, will increase value of R-squared. But it does not automatically mean that the fit is improved. Often the data does not contain enough information to estimate the extra fitted coefficients accurately. In other words, the more complex model overfits the data. To avoid this situation use of the *degrees of freedom adjusted R- squared* statistic is recommended.

The *degrees of freedom adjusted R- squared* statistic (or adjusted R- squared) is:

$$AdjustedR^2 = 1 - \frac{SSE(n-1)}{SST(\nu - 1)} \qquad \text{(A 2.25)}$$

where $\nu = n - m$ is the residual degrees of freedom defined as the number of the measured values n minus the number of fitted coefficients m estimated from the fit. The value ν indicates the number of independent pieces of information involving the n data points that are required to calculate the sum of squares.

The *root mean squared error* (*RMSE*) also known as the fit standard error or the standard error of regression is defined as:

$$RMSE = \sqrt{MSE} = \sqrt{\frac{SSE}{\nu}} \qquad \text{(A 2.26)}$$

where MSE is the mean square error or the residual mean square. Similar to the SSE, an $RMSE$ value closer to 0 indicates a fit that is more useful for prediction.

The goodness of fit tests can be used to compare different fitted models on an objective basis. We can compare nested models fitted to the same dataset with the *F test*. This has been designed to allow hypotheses involving multiple parameters to be tested simultaneously.

Two models are nested if one (the reduced model) is obtained from the other (the complete model) by setting some parameters to zero (i.e. removing terms from the model), or some other constraint on the parameters. The F-test consists in comparing the SSE for the reduced model (SSE_R) and SSE for the complete model (SSE_C). The restricted model includes k parameters, the complete model has $k + p$ parameters. A test statistic called the F-ratio is introduced as:

$$F = \frac{(SSE_R - SSE_C)/\, p}{SSE_C /(n - (k + p + 1)} \qquad \text{(A 2.27)}$$

It has an F distribution with degrees of freedom (ν_1, ν_2), where $\nu_1 = p, \quad \nu_2 = n - (k + p + 1)$. At the chosen level of significance α the calculated F-statistic is compared to an F_{α,ν_1,ν_2} which can be obtained from tables or calculated by

statistical software. If $F \geq F_{\alpha,\nu_1,\nu_2}$, the difference between the reduced model and the complete model is statistically significant. In other words, for the F-statistic to increase with an additional parameter, that parameter must make a significant contribution to improving the overall fit.

The degrees of freedom adjusted R- squared statistic as well as the F-statistic are generally the best indicators of the fit quality when two nested models are compared. If models are not nested, using other goodness-of-fit statistics such as R-squared or $RMSE$ is preferable.

The parameters estimated from the fit will also have uncertainties (standard errors of parameters). They can be found using the error propagation method discussed in Section 4. Each of the data points y_i has been used in the determination of the parameters and each has contributed some fraction of its own uncertainty to the uncertainty in the final determination.

Thus, the obtained standard errors in the parameters indirectly tell how well the curve fits the data. If the standard error is small, it means that a small variation in the parameter would produce a curve that fits the data much worse. If the standard error is large, a relatively large variation of that parameter would not modify the fit much; therefore, the parameter's value is not determined well.

Standard errors are related to another quantity, usually obtained from the fitting and computed by curve-fitting software: the confidence interval. This shows how good the obtained estimate of the value of the fitting function is at a particular value of (x_i). The confidence interval gives a desired level of statistical confidence α. For a particular value of x_i, it can be claimed that the correct value for the fitting function lies within the obtained confidence interval. Curve-fitting software can compute the confidence interval and draw the confidence interval lines on the graph with the fitted curve and the data points. The smaller the confidence interval, the more likely the obtained curve is close to the real curve.

Another useful quantity usually produced by curve-fitting software is the prediction interval. Whereas the confidence interval deals with the estimate of the fitting function and describes modelling error, the prediction interval deals with the data and

includes modelling and sampling errors. It is also computed with respect to a desired confidence level. The prediction interval is the interval of y values for a given x_i value within which a desired percentage of all experimental points in a series of repeated measurements are expected to fall. The narrower the interval, the better the predictive nature of the model used. The prediction interval is represented by two curves lying on opposite sides of the fitted curve. Because the prediction intervals reflect both modelling and sampling errors, they are larger than the corresponding range of the residuals.